IONS IN ELECTRICALLY CONDUCTIVE AND INSULATING METAL-ORGANIC-FRAMEWORKS: TRANSPORT AND ENERGY STORAGE

by

Alice Yue Su

B.Sc. in Chemistry
Technical University of Munich, 2021

SUBMITTED TO THE DEPARTMENT OF CHEMISTRY

IN PARTIAL FULFILLMENT OF THE REQUIREMENTS FOR THE DEGREE OF

DOCTOR OF PHILOSOPHY IN CHEMISTRY

AT THE

MASSACHUSETTS INSTITUTE OF TECHNOLOGY

September 2025

Authored by: Alice Yue Su
Department of Chemistry
August 15, 2025

Certified by: Mircea Dincă
W. M. Keck Professor of Energy, Department of Chemistry
Thesis Supervisor

Accepted by: Adam P. Willard
Professor of Chemistry
Graduate Officer

This doctoral thesis has been examined by a Committee of the Department of Chemistry as follows:

Professor Danna E. Freedman .....
Thesis Committee Chair
Frederick George Keyes Professor of Chemistry

Professor Mircea Dincă .....
Thesis Supervisor
W. M. Keck Professor of Energy

Professor Timothy M. Swager .....
Thesis Committee Member
John D. MacArthur Professor of Chemistry

IONS IN ELECTRICALLY CONDUCTIVE AND INSULATING METAL-ORGANIC-FRAMEWORKS: TRANSPORT AND ENERGY STORAGE

by

Alice Yue Su

Submitted to the Department of Chemistry

on August 15, 2025

in Partial Fulfillment of the Requirements for the Degree of

Doctor of Philosophy in Chemistry

ABSTRACT

Ion transport in metal-organic frameworks (MOFs) is attracting increasing attention since ions can be easily incorporated into porous MOF structures as guest species, promising a variety of possible applications. While electronically insulating but ionically conductive MOFs show great potential as solid electrolytes, the precise structure and tunability of MOFs also enables rational combination of electronic and ionic conductivity to create intrinsic mixed conductors. The combination of both conduction pathways is highly relevant for energy storage applications where ions interact with and insert into electronically conductive electrode active materials. This thesis first explores ion transport in an anionic MOF electrolyte, conducting mono- and divalent cations. Transport studies give insight into how MOF structure and ion-related variables impact ionic conductivity and activation energy. Studies on this material paint a picture that furthers our understanding of fundamental ion transport mechanism in MOF electrolytes. Incorporating electronic transport as an additional layer of complexity, new mixed proton-electron conductive two-dimensional MOFs based on aromatic azaborine ligands are synthesized. Their dual conductive nature is confirmed by separating the ionic and electronic contributions to the overall transport. Lastly, a family of triazatruxene-based two-dimensional electronically conductive MOFs are explored as pseudocapacitors. Here, the diffusion of ions inside the pore network as well as their interaction with MOF active sites depending on the interlayer spacing are investigated for their impact on capacitance.

Thesis supervisor: Mircea Dincă

Title: W. M. Keck Professor of Energy

Acknowledgements

First and foremost, I would like to express my tremendous gratitude to my advisor, Mircea Dincă. Thank you for supporting me throughout the years and giving me the freedom to pursue the research that I enjoyed. I am grateful for your guidance and insight, allowing me to grow more confident in myself and my work. I wish you and the lab success in this next chapter and hope it will be what you hoped for.

Thank you to Danna Freedman and Tim Swager for serving as my thesis committee. Your advice and insight were always greatly appreciated.

This research would not have been possible without my collaborators. I am greatly indebted to Petru Apostol and Alex Vlad for their contributions to Chapter 4 and to Stefano Canossa for performing the diffraction studies for Chapter 2. I would like to also thank my labmates Jules Oppenheim, Zhentao Yang and Jiande Wang for their significant scientific contributions. It was a pleasure and privilege working with you.

I am immensely grateful to all past and current Dincă lab members that I overlapped with. Too many people came and left during my time in the Dincă lab to recount here, but I want to especially express my gratitude to Tianyang, Mike, Alina, Harish, Justin, Andrei and Jules for their mentorship when I joined the lab; and Bowen, Zhentao and Jiande for their wisdom throughout the years. I am grateful for all the friendships that have started in the lab and continue beyond.

Lastly, I would like to thank my friends, David, Henry, and my parents for their love and support.

Contents

Chapter 3

Dual Proton-Electron Conduction in 2D Azaborine Metal-organic Frameworks

Chapter 4

Electrochemical Capacitance Traces with Interlayer Spacing in Two-dimensional Conductive Metal–organic Frameworks

List of Figures

Chapter 1

Chapter 2

Chapter 3

Chapter 4

List of Tables

Chapter 1

Electron and Ion Transport in Metal-organic Frameworks

1.1 Why We Want MOFs to Conduct

Metal-organic frameworks (MOFs) stand out most prominently for their ultrahigh porosity and surface area.[1] They are highly tunable due to their modular build from combinations of metal ions or clusters and organic ligands. This opens a huge pool of possible combinations, leading to different topologies and physical properties. The molecular nature of MOFs provides accessible functional sites across the material, meaning that MOFs can form specific interactions with guest molecules. Naturally, these materials excel in applications like gas storage and separation that take advantage of their superior porosity and molecular interactions. Electrical conductivity, at a first glance, may seem to be at odds with the permanent porosity of MOFs. However, it has been shown over the past 10+ years that it is possible to enable efficient electronic transport in MOFs. Electronic phenomena that were previously reserved for traditionally dense inorganic solids such as superconductivity or the formation of charge density waves have been increasingly emerging in newly discovered MOFs over the past years.[2,3] With the exponentially growing body of research in this field, we are able to make increasingly better use of the precise structural architectures and interactions to design conductive MOFs with targeted properties.

For applications like energy storage or chemiresistive sensing, the porosity of electronically conductive MOFs can be a unique strength. Permanent pores allow for facile entering of molecular or ionic guest species into the pore system to closely interact with the large internal surface, benefiting energy density or chemiresistive response. Unlike non-porous materials, MOFs provide pathways for ions to conduct without large energy barriers from structural distortions in the material. This makes MOFs great candidates for many ion transport applications like solid electrolytes or membranes. The precisely engineered pore sizes also

allow MOFs to engage in specific interactions with ions of various sizes, making them promising materials for separations.

While electronic and ionic transport in MOFs have separately been of great interest to the research community, the combination of both transport pathways is equally sought after, while more elusive. For MOFs, ion transport in electrode materials has attracted limited attention despite dual ion-electron conductivity being fundamental to energy storage processes. Furthermore, new developments in the field of electronics ranging from transistors, bioelectronics, or neuromorphic devices call for the discovery of new mixed conductors to meet the material demands of new device architectures. In this chapter, fundamental principles and examples of electronic, ionic, and mixed transport in MOFs will be reviewed.

1.2 Electronically Conductive MOFs

Similar to organic electronic conductors, electronic charge transport in MOFs can be enabled through redox hopping: Conductive MOFs are created by incorporating redox active ligands in various geometries and distances depending on the MOF topology. Charges are transported through a hopping-based mechanism in which they move from one ligand to the next through formal oxidation and reduction. This hopping mechanism can be further supported by guest species within the pores that take part in the redox reactions, bridging the distance between framework ligands.[4,5]

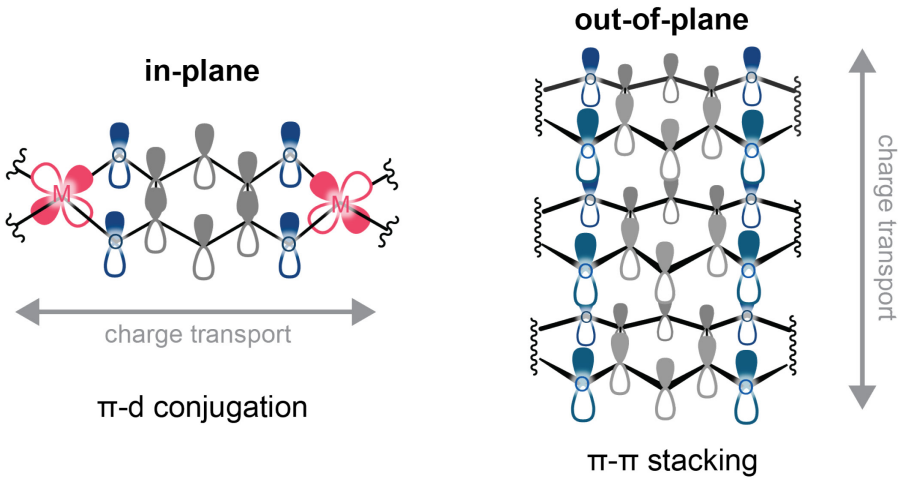

Figure 1-1. Charge transport pathways in 2D conductive MOFs. In-plane conjugation is enabled by π-d conjugation between the ligand π-orbitals and transition metal d-orbitals. Out-of-plane conjugation is facilitated by π-π orbital overlap of organic ligands.

Band-like charge transport in MOFs can give rise to higher conductivities than redox-hopping-based mechanisms. Here, electronic charges are conducted as a result of orbital overlap between organic ligands and metal ions. Charge mobility is ensured by employing conjugated ligands with delocalized molecular orbitals that coordinate to transition metal ions through *ortho*-hydroxy, amine, or thiol groups. Effective orbital overlap is achieved by constraining ligand orientations to form 2D sheets, analogous to graphene. Typically, electronic charges are transported in the 2D plane as well as perpendicular to it. The through-bond transport pathway is enabled by π-*d* overlap of ligand π-orbitals and neighboring transition metal *d*-orbitals. Close π-π stacking of ligand orbitals gives rise to out-of-plane conductivity, creating through space transport pathways.[5]

Despite the constraint of forming 2D materials, there is great flexibility in the type of ligands that can be incorporated into conductive MOFs, resulting in various 2D topologies. Prototypical ligands show trigonal symmetry, e.g. seen in triphenylene-[6–8] or benzene-based molecules,[9,10] forming hexagonal lattices. Alternative symmetries like square symmetric metal-phthalcyanines[11,12] or lower symmetry molcules[13] have been successfully incorporated into 2D MOF as well.

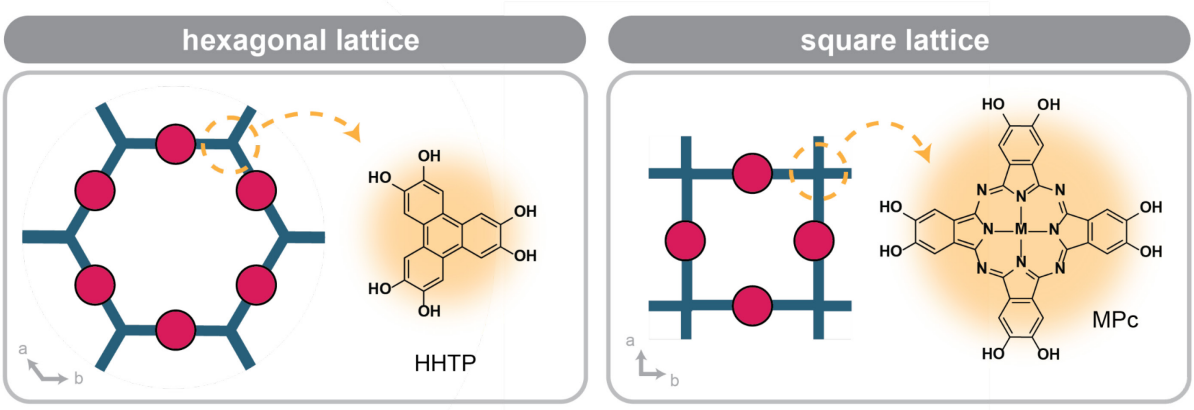

Figure 1-2. Hexagonal and square 2D MOF lattices viewed from the crystallographic *c*-direction. The red circles represent metal ions; blue sticks represent organic ligands. Typical ligands that form hexagonal and square lattices include hexahydroxytriphenylene (HHTP) and metal-phthalocyanine (MPc), respectively.

While true 2D MOFs typically show both through-space and through-bond transport pathways, breaking the 2D layers by offsetting metal ion positions isolates the out-of-plane charge transport pathway. A typical example are $Ln_{1+x}HHTP$ ($x = 0$ to 0.2; Ln = La, Nd, Ho, Yb; referred to as LnHHTP) MOFs. The ionic character of the Ln-O bond and offset Ln positions in pseudo-tetrahedral coordination environments prohibit charge delocalization from the ligand

to the metal.[14] DFT band structure calculations confirmed flat bands in the crystallographic *ab* plane and significant band dispersion in the *c*-direction. Despite breaking the extended in-plane conjugation, significant electronic conductivity was measured with values between 0.9×10^{-4} S/cm for LaHHTP and 0.05 S/cm for HoHHTP, respectively.[14] The stacking distance determines the extent of π-π orbital overlap and in extension the electronic conductivity. For the series of LnHHTP, for instance, the increasing interlayer distance from Yb to Ho, Nd, and La coincides roughly with decreasing conductivity. Based on the same principle, interlayer distance was modified in a series of triazatruxene-based 2D MOFs by changing the lengths of the ligand alkyl side chains. The π-π stacking of the 2D layers increased with alkyl chain length. The conductivity was in turn found to decrease with larger interlayer spacing.[15]

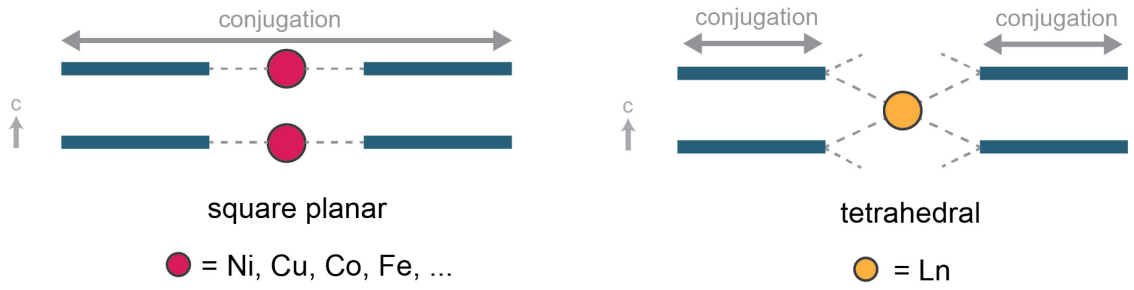

Figure 1-3. Side-view of 2D MOF structures with square planar and tetrahedral metal ion coordination environments. Square planar coordination is typically found for Ni, Cu, Co, and Fe ions. These ions lie in the same plane as the aromatic ligands. Lanthanide ions typically occupy positions between ligand layers, in a (quasi) tetrahedral coordination environment, breaking the in-plane conjugation.

While it is possible to reliably predict and synthesize 2D conductive MOFs using aromatic ligands and transition metals, structural nuances that can affect conductivity remain poorly understood. For instance, stacking modes or interlayer distances that have substantial effects on the value of electronic conductivity cannot generally be predicted purely based on the molecular ligands.[16,17] Additionally, observations such as the superior charge transport when using *o*-diamine- as opposed to *o*-dihydroxy-based ligands or nickel ions instead of copper ions have not been fundamentally explained.[18,19] With more and more MOFs being discovered and their physical and structural properties characterized using increasingly more sophisticated techniques, there is hope to gain fundamental understanding of electronically conductive MOFs.

1.3 Ionically conductive MOFs

Ionically conductive porous materials can be understood as a mix of traditional solid and liquid electrolytes. Mobile ionic charge carriers reside in pores and move through a typically solvent filled pore network. Analogous to liquid electrolytes, ions in porous electrolytes can exist in a solvated environment with a solvation shell. Ions may therefore be transported in a similar environment to liquid electrolytes, but in a confined space. At the same time, confinement may drastically affect the properties of liquids and ion transport. Additionally, immobilized molecular sites in MOFs are expected to be able to interact with ions, adding another layer of complexity. In a MOF in which hopping sites are in close proximity, a transport mechanism similar to hopping-based ion conduction in the non-porous crystalline solid state may even be dominant.

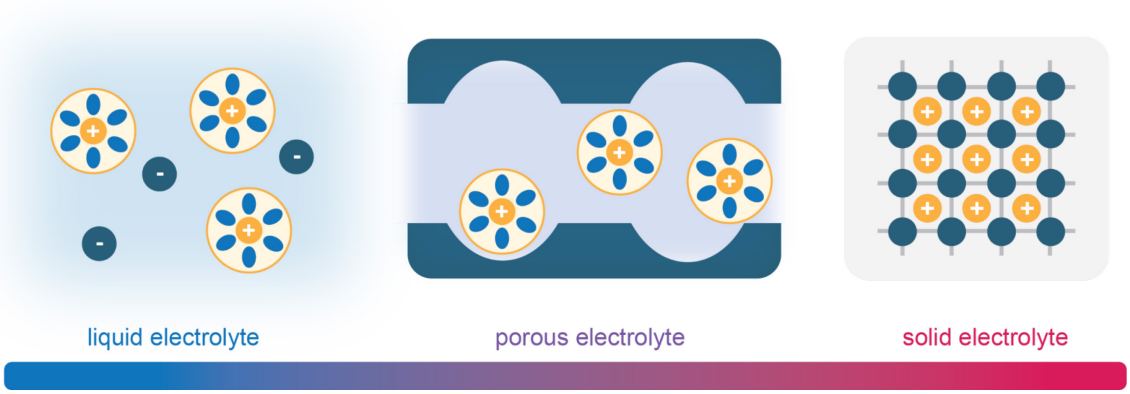

Figure 1-4. Porous electrolytes can be understood to exist between liquid and solid electrolytes. Liquid electrolytes contain cations with solvation shells in a liquid solvent; solid electrolytes typically have ordered crystal lattices with cations occupying crystallographic defined positions. Porous electrolytes contain cations with solvation shell in a solvent environment that is contained by a porous solid.

While it is not understood how exactly all facets of MOF structure play together to dictate the transport of ions, there are copious examples of highly ionically conductive MOFs.[20] The insertion of mobile ionic charge carriers, either protons or other cations, is typically the key step to synthesizing MOF electrolytes. Naturally, this aspect of ionically conductive MOFs is well established, as many strategies for ion insertion have been suggested.

1.3.1 Proton Conduction

As proton conductive MOFs have been described and summarized in detail elsewhere, this section will give a brief overview of common proton insertion strategies:[21,30] Proton conduction can be facilitated by guest molecules residing in MOF pores. These can be either ionic species, like H_3O^+, NH_4^+, and $Me_2NH_2^+$ or neutral acidic species like water, strong acids, imidazole etc.[21–25] Alternatively, organic ligands can feature functional groups containing acidic protons such as sulfonic acids, phosphonic acids, or carboxylic acids.[26–28] Open metal sites on cluster or metal SBUs provide coordination sites to molecules like water, acidifying the protons.[29]

Two ideal transport mechanisms, the Grotthus and the vehicular mechanism, are typically distinguished for proton conductors. In case of the vehicular mechanism, protons travel as charged molecules, such as H_3O^+, over long distances.[31] The Grotthus mechanism proposes that protons are shuttled between hopping sites via formation and breaking of hydrogen bonds. The effectively travelled distance of a single charge is thus greater than the travelled distance of each proton.[32] To distinguish between the two mechanisms, the activation energy of the transport process is typically used as the deciding factor because the Grotthus mechanism requires a much smaller activation energy compared to vehicular transport.

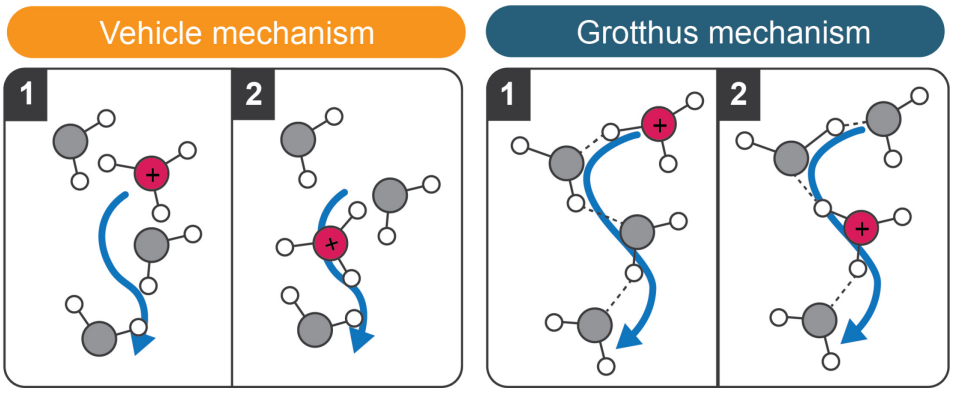

Figure1-5. Proton transport occurs through one of two mechanisms, the vehicle or Grotthus mechanism. Charged molecules are transported in the vehicle mechanism while the Grotthus mechanism describes proton transport as the transport of protons through formation and breaking hydrogen bonds.

1.3.2 Ion Conduction

While mobile cations can be easily inserted into a porous material through soaking in salt solutions, both anions and cations of the salt will be incorporated to maintain charge balance. This leads to undesirable low transference numbers, similar to liquid electrolytes. Instead, using

anionic groups that are tethered to the MOF as either part of the organic ligand or coordinated to secondary building units (SBUs) ensures exclusive cation transport.

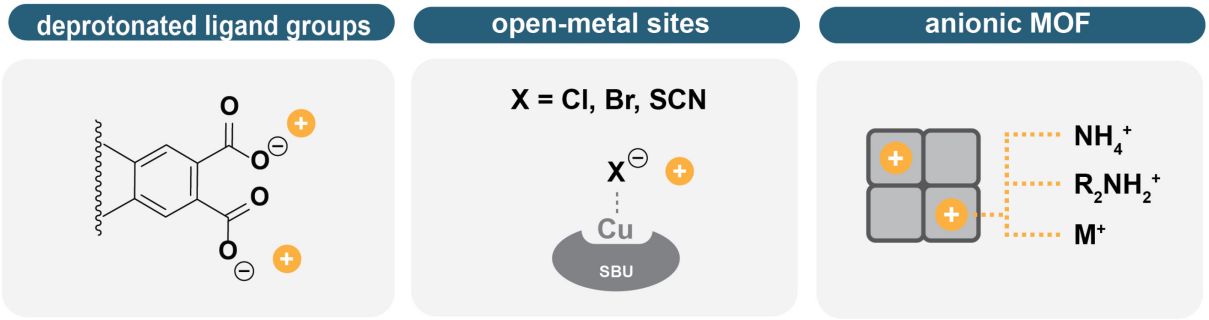

Figure 1-6. Three common strategies for inserting cations as mobile charge carriers into MOFs are deprotonating organic ligands with inorganic bases, coordinating anions with open metal-sites on MOF SBUs, and using anionic MOFs.

Building on established strategies for proton insertion, acid groups on organic ligands can be deprotonated using inorganic bases such as LiOH. The corresponding cation will then reside in the pores, loosely associated with the anionic base.[33,34] Open metal sites on SBUs can serve as coordination sites to immobilize anions.[35,36] This has, for instance, been shown for Cu-SBUs that were able to anchor halide anions, leaving Li^+, Na^+ or Mg^{2+} cations as mobile charge carriers in the pores.[35] The strength of the ion pairing between mobile cation and tethered anionic group determines the conductivity and activation energy of ion transport. Transference number and activation energy can be a trade-off in these types of ionically conductive MOFs as weaker ion pairings give rise to lower activation energies but also cause anions to be more weakly tethered to the SBU sites, lowering the transference number.[35] There are a number of anionic MOFs that do not have a neutral counterpart but are synthesized directly as an anionic framework with counterbalancing cations in the pores.[37–39] Even though it remains unclear why some combinations of metals and ligands assemble as anionic instead of neutral MOFs under certain synthetic conditions, they are often excellent candidates for ion transport. Organic amine-based cations are particularly common in as-synthesized anionic MOFs because they form as decomposition products from organic amine solvents during solvothermal synthesis.[37,39] However, with the addition of inorganic salts to the reaction mixture, incorporation of other cations, such as K^+ or NH_4^+, are possible as well.[40,41] Generally, any mobile cation can be easily exchanged for another in a corresponding salt solution in order to incorporate the desired charge carrier species. In anionic MOFs, interactions between cations and anionic sites are often more elusive since the anionic sites are not necessarily single

molecular sites but can consist of multiple molecular sites that form a coordination pocket in the assembled MOF.

1.3.3 Ion Transport in Solid and Liquid Electrolytes

To understand how ions are moving inside porous materials, we can draw from knowledge of ion transport in the liquid and non-porous solid state. While it is expected that porous ion conductors are not a simple combination of liquid and non-porous solid electrolytes, understanding each transport mechanisms may give valuable intuition and provide general concepts that can be extended to porous ion conductors.

Ion transport in liquid electrolytes can be understood as the shuttling of solvated ions through a uniform environment of liquid solvent. The ionic conductivity is dependent on the viscosity of the solvent (impacting the ion migration) and the degree of solvation of the ions (dictating the degree of dissociation of ion pairs):[42]

$$\sigma_i = \sum_i n_i \, \mu_i Z_i e \tag{1}$$

Here, the ionic conductivity σ is expressed through the number of free ions n_i, their mobility μ_i and charge $Z_i e$. The degree to which solvents can facilitate dissociation of ion pairs determined by their dielectric constant. Solvents with high dielectric constants can better shield the dissociated ions, leading to a higher degree of dissociation. The Stokes-Einstein relationship describes how the ion mobility μ_i is dependent on solvent-related quantities, namely viscosity η and solvation radius of the ion r_i:

$$\mu_i = \frac{1}{6\pi\eta r_i} \tag{2}$$

As μ_i and η are inversely related, the more viscous a solvent, the less mobile the solvated ion is. Similarly, the larger the solvation radius r_i of the ion, the less mobile it is. Typically, the choice of electrolyte solvent calls for a balance between low viscosity and high dielectric constant.[42] As both anions and cations are present in liquid electrolytes, not all current stems from cation shuttling. In fact, typical transference numbers for lithium-based liquid electrolytes lie in the range of 0.2 to 0.4, meaning that 60 to 80% of the current is caused by anion movement. Anion conduction is especially significant in comparison to small inorganic cations. Due to the

low degree of anion solvation, they are more mobile than metal cations with typically large solvation shells.[42]

In non-porous solid cation conductors, anion movement is not a concern as ions occupy fixed crystallographic positions giving rise to transference numbers of 1. Pure cation conduction mitigates the issue of concentration polarization caused by anion build-up at the electrode interface in liquid electrolyte systems. Additionally, solid electrolytes are often superior in terms of electrochemical and thermal stability. Most importantly, they promise to eliminate the risk of solvent flammability in battery cells which is one of the major concerns for current commercial battery systems.[43] However, achieving high ion mobilities and conductivities in the solid state and enabling homogeneous and wide interfacial contact is significantly more challenging than in the liquid state.[43,44]

Ions are transported across a much steeper energy landscape in non-porous solid electrolytes, typically inorganic ceramics, than in liquid electrolytes. They move from one local energetic minimum to another. These minima are generally crystallographically defined sites that fit a specific ion. The movement of ions is largely determined by the energy barriers between local minima (migration energy) and by the number of interstitials and vacant sites.[43] Interstitials, caused by aliovalent doping, or defects create vacant sites that ions can move into. This is described by the trapping energy or defect formation energy. The combination of migration, defect formation, and trapping energy constitutes the apparent activation energy for ion transport in the non-porous solids state. The Nernst-Einstein equation relates the ion diffusivity D_i to the mobility μ_i:

$$\mu_i = \frac{D_i}{k_B T} \tag{3}$$

with the Boltzmann constant k_B and temperature T. The ionic conductivity σ_i is given as

$$\sigma_i = \frac{\sigma_0}{T} e^{-\frac{E_A}{k_B T}} \tag{4}$$

with E_A as the activation energy.[43]

While ion transport in the solid state typically yields lower ionic conductivities and mobilities compared to the liquid state, state of the art crystalline solid electrolytes can reach conductivities in the typical range for commercial liquid electrolytes. For instance, LISCON and similar lithium-ion conductors can reach conductivity values of up to 10^{-3} to 10^{-2} S/cm.

This is rivals liquid electrolytes like 1M $LiPF_6$ or LiTFSI in EC/DMC and is sufficient for many battery applications.[45,46]

1.3.4 Ion Transport in Porous Electrolytes

The mechanism of ion transport in porous solids that are filled with confined liquids is poorly understood. To place porous electrolytes within our current framework of understanding, we can imagine two extremes: conductors with infinitely large pore or small pores, approaching the size of the mobile ion, effectively behaving like traditional liquid or solid electrolytes. The pore sizes found for real MOFs lie between those extremes, ranging from Angstrom to nanometers in diameter. The mechanism of ion transport may thus also be expected to vary from liquid- to solid-like based on the pore size. However, with specific pore shapes and connectivity, molecular components, and confined secondary electrolytes, an altogether more nuanced ion transport process can be surmised.

Considering the shape or dimensionality of a pore network, for instance, linear one-dimensional pore channels could perhaps provide the most straight-forwards path for ion transport in a single MOF crystal. If these channels are oriented along the electric field gradient, ions can move along the gradient in a linear path. In bulk powders, however, crystallites are packed in random orientations. In this case, unidirectional pores may be less favorable than a three-dimensional pore network that allows for easier alignment of pore channels between neighboring grains.

Hopping sites are another essential component of MOF ion conductors. Anionic functional groups typically serve as hopping sites. But hopping sites can also be more structurally complex and consist of pockets of multiple molecular sites. This was for example observed for the zinc ion conductor ZnZnBTT (BTT = 1,3,5-benzenetristetrazolate) in which zinc ion positions were crystallographically pinpointed between two tetrazolate groups on neighboring ligands.[38] Similar to the migration energy in non-porous solid conductors, there is an energy barrier to ions hopping between two sites in porous conductors that depends on their interaction strength. From a liquid-based perspective, the interaction strength indicates the degree of dissociation of ion pairs - in this case, between a mobile cation and an immobile anionic unit. The density of hopping sites or the distance between sites will most likely affect the ionic conductivity and transport mechanism significantly. Smaller distances between hopping sites may be beneficial for transport as it lowers the energy barrier between two sites, but larger distances are not

necessarily unfavorable. Since ions are solvated, larger distances between hopping sites could be traversed in a solvent assisted fashion instead of a traditional hopping-like mechanism. In this case, the viscosity of the solvent, for instance, could play a larger role for the ionic conductivity. Hopping site distance may therefore cause a shift between liquid-like and solid-like transport, where either could have the potential to yield high conductivity depending on the specific material.

Apart from the organic framework ligands, the secondary electrolyte is a significant molecular component in MOF electrolytes. The secondary electrolyte forms solvation shells around mobile ions and shields ions from interactions with the framework and hopping sites. As seen in the previous section, the solvation radius of ions is linearly related to ion mobility. Qualitatively, the same relationship between solvation radii and mobility may be expected in MOFs. Furthermore, the same model describes the linear relationship between viscosity of the solvent and the ionic conductivity. Depending on the degree of confinement, solvents can adopt higher or lower viscosities than in their unconfined state. While solvent viscosities have not been subject to investigation in MOFs, we can consult other instances of confined liquids to gain insight into how viscosity changes with pore size. The viscosity of water in carbon nanotube channels down to 8 Å has been computationally investigated by many groups and was found to decrease with decreasing channel diameter. It was calculated to be smaller than bulk water for all investigated nanotube sizes. Viscosity, however, also depends on the interaction of water molecules with the pore walls and the pore shape. For example, viscosity is predicted to be higher for cylindrical pores than slit-like pores and varies based on the hydrophilicity of the channel walls.[47–49] If it was possible to measure solvent viscosity in MOFs, its relationship to conductivity may be investigated.

Depending on the molecular properties and solvation energy of the secondary electrolyte, ions are expected to interact with hopping sites through their solvation shell or shed their solvation shell to interact with them. The solvation energy will also determine if there are events of solvation and shedding of the solvation shell during ion transport. The latter could, for example, occur in a MOF in which larger pores are connected by smaller diameter windows. These effects are commonly observed in MOFs for ion-ion separation purposes where ion separation is based differences in hydration energies and dehydration-rehydration events based on the size of hydrated ions and window sizes.[50,51]

In MOFs electrolytes, the charge of the ion does not only dictate the solvated ion radii and chemical interactions with molecular moieties but also dictates the charge carrier density in a given MOF as the total number of mobile ionic charges is equal to the total charge of the framework due to charge balance.

The complexity of porous electrolyte systems renders computational studies, such as MD simulations, extremely challenging and expensive. Results may not be accurate as many assumptions and simplifications have to be made. The lack of fundamental understanding of how to consolidate the ideas of liquid and solid transport and adapt them for porous conductors inhibits effective prediction and rational design of ionic conductors. Systematic studies on MOF ion conductors should aim to isolate specific structural factors through rational variation and tuning to reveal the impact of each component. Overall, the goal is to create a model of conduction that can be employed to design and understand new materials.

1.4 Mixed Ionic-Electronic Conductive MOFs

Combining electronic and ionic conductivity is a significant challenge for MOFs and other material classes like inorganic crystalline solids or organic solids.[52,53] Enabling both conduction pathways can be a trade-off between electronic and ionic transport. This is especially prominent in materials without permanent porosity where ion transport often causes small structural distortions that can be detrimental for electron transport. Porous materials provide an opportunity to spatially separate the two conduction pathways. Electronic conduction can be enabled through the framework while ions are transported through the pores. The design of mixed conductive MOFs can be rationally approached starting from either an ionically or electronically conductive MOF. With ionically conductive MOFs, the use of aromatic and redox active cores in ligand molecules can facilitate electronic charge transport through redox hopping. Alternatively starting from a 2D electronically conductive MOF, functional groups containing mobile ions can be added to ligands or metals to enable ionic conductivity.

1.4.1 Intrinsically Mixed Conductive MOFs

Proton-electron mixed conductivity is most frequently reported in MOFs due to the relative ease of inserting mobile protons through organic acid moieties while exchanging these protons for other ions would add an additional synthetic step.[54–57] Mixed electron and proton

conductivity was, for example, reported by Su *et al.* in a 2D tetrathiafulvalene based MOF, containing $[In(COO)_4]^-$ SBUs. Proton conductivity here is enabled by the carboxylic acid groups and methylammonium and hydronium guest molecules that can contribute to the formation of a hydrogen bonding network. An electrical current was measured despite the lack of intrinsic electronic conduction pathways as this material does not possess in-plane π-d conjugation. The authors assign the measured current to faradaic pseudocapacitive processes at the MOF electrode interface in which the oxidation states of the redox active ligands are changed. The pseudocapacitive current is amplified at high humidities due to the higher concentration of protonic charge carriers, with the DC electrical conductivity measured as 4.05 × 10^{-3} S/cm. At lower relative humidity (40% RH) moderate values for proton conductivity were achieved. At 90% RH, the material with free carboxylic acid groups showed high proton conductivity of 1.30 × 10^{-2} S/cm. [58]

Rambabu *et al.* employed a similar strategy to design mixed conductive MOFs based on 2,5-dihydroxy-1,4-benzenediphosphonic acid ligands (H_6-DOBDP). Their champion material, containing Fe(III) nodes, exhibits proton conductivity of 1.6 × 10^{-4} S/cm and electron conductivity of 8.3 × 10^{-7} S/cm in a hydrated state. Here, proton conductivity is enabled through P-OH groups while intrinsic electron conduction is proposed to be based on redox hopping between Fe centers in 1D $[Fe(O_2P\text{-}OH)_3]_n$ chains.[57]

He *et al.* used intercalated 2D MOFs as platforms to enable mixed conductivity. Intercalation of $[Co_7(OH)_6(H_2O)_3(C_4H_4O_4)_4]\cdot 7H_2O$ with K^+, $H_2PO_4^-$, HPO_4^{2-} and H_2O in a neutral K_2HPO_4 and KH_2PO_4 solution increased protonic and electronic conductivity compared to the starting material. Conductivity values of 2.02 × 10^{-5} S/cm and 3.84 × 10^{-4} S/cm at 100 °C and 99% RH were reported for proton and electron transport, respectively. This was rationalized through additional protonic charge carriers and channels provided by the intercalation and more efficient band-like electronic transport due to the lowered band gap after intercalation, derived from DFT band-structure calculations.[59]

An example of dual conduction in a 2D electrically conductive MOF was reported by Choi *et al.* in zinc hexahydroxytriphenylene (HHTP). As expected, electronic conduction is facilitated through π-d conjugation here. The authors propose a staggered structure for the 2D layers with axial aqua groups coordinating to Zn ions that should facilitate proton transport. An alternative structure without staggered layers recently reported by Zhang *et al.* may also be able to facilitate proton transport through dangling ligand catechol groups.[60] Nevertheless, Choi *et al.*

reported proton conductivity of 1.1×10^{-6} S/cm and high electrical conductivity of 1.8×10^{-2} S/cm at 95% RH.[61]

1.4.2 Methods for Characterizing Mixed Transport

The characterization of mixed conductors can be a great challenge as the separation of the electronic and ionic contributions to the electrical current is not trivial.[62,63] The transference number describes the total electrical current as a sum of all current contributions. In a dual conductor, it provides information on the ionic current when the electronic current is known and *vice versa*. There are a number of methods that can be used to quantify the contribution of each transport process. Huggins summarizes several DC methods based on asymmetric polarization or open circuit potentials for this purpose.[64] For MOFs, however, these DC methods are typically difficult to realize as they require robust understanding of the system, and thorough control of the thermodynamic conditions. As MOFs are generally more ill-defined compared to inorganic metallic or ceramic materials, precise knowledge of the system and interfacial processes may not be given.[64]

Variable frequency AC methods can be used to probe charge transport in solids using less sophisticated cell setups. This powerful method allows for the collection of large amounts of information on various transport processes with different time constants without requiring fundamental thermodynamic understanding of the system. AC electrochemical impedance spectroscopy (EIS) does, however, demand general knowledge of the number and types of transport processes in each system as it cannot be used to unambiguously assign them to physical events. This also means that impedance data alone cannot be used to determine whether a process is ionic or electronic in nature but must be supplemented with other physical or electrochemical characterization of the system.[64]

Figure 1-7 shows the schematic of a typical two-contact cell used for AC impedance measurements. While four-contact cells can be used as an alternative to reduce contact resistance, the setup is more challenging, especially when using brittle MOF pellets. A typical EIS measurement of a mixed conductor that transports electrons and one ionic species yields data in the shape of two semicircles in the Nyquist representation (**Figure 1-7**). The lack of a capacitive feature at low frequencies indicates a strong contribution of the electronic component as any capacitance is shunted by electronic transport.[64]

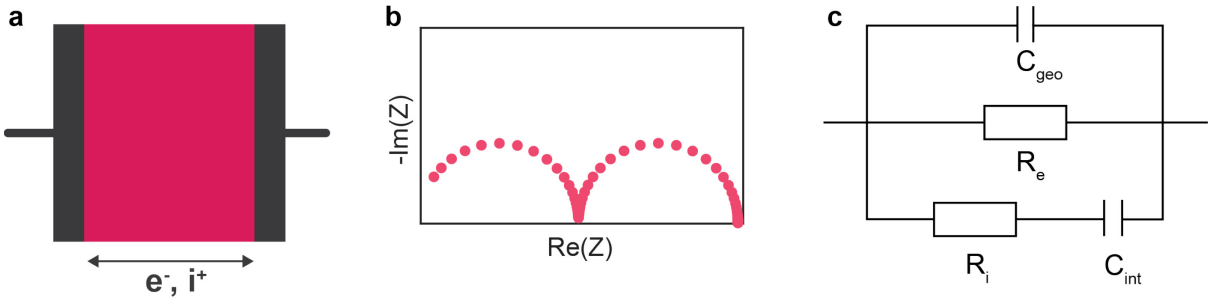

Figure 1-7. a) Cell setup for AC impedance measurements: MOF pellets are sandwiched between two parallel current collector plates. In mixed-conductive MOFs, ion and electrons are transported through the material at the same time. b) Nyquist plot of a mixed ionic-electronic conductor and c) corresponding equivalent circuit.

This data can be understood quantitatively through equivalent circuit modelling. The assignment of equivalent circuits to experimental data is ambiguous in most cases, highlighting the necessity of general knowledge of expected transport processes to choose the equivalent circuit that most accurately describes the true physical system. In mixed conductors electronic and ionic transport occur simultaneously in the same material. With this knowledge, the equivalent circuit can be built using three parallel rails: the geometric capacitance C_{geo} between the parallel current collector plates, the electronic resistance R_e, and the ionic rail consisting of ionic resistance R_i and interfacial capacitance C_{int} (**Figure 1-7**). Graphically, the x-axis intercept at the low frequency limit (R_2) is equal the electronic resistance R_e. R_1 is a combination of ionic and electronic relaxation, thus $1/R_1 = 1/R_i + 1/R_e$ since R_e and R_i are parallel.[64] Caution must be exercised as an equivalent circuit with two parallel RC elements that are connected in series would fit the same data but the serial nature of R_e and R_i would give non-physical results. Polycrystalline samples may show a third semicircle in the Nyquist plot which stems from transport across grain boundaries. In this case an additional RC element should be added to the ionic rail in the equivalent circuit model shown in **Figure 1-7**.[64]

For real samples, the resolution and quality of the AC data may not be sufficient to clearly observe both semicircles for a mixed conductor. This is especially relevant when the magnitudes of R_e and R_i are significantly mismatched, or the ratios of the capacitances cause less defined semicircular shapes. In either case, supplementation of the AC data with additional AC or DC measurements may be appropriate. Depending on which transport pathway is dominant, different strategies can be employed: If the ionic conductivity is the main conduction pathway, EIS will result in a semicircle with a capacitive low frequency tail. The ionic

conductivity can be easily determined from equivalent circuit fitting, analogous to pure ionic conductors. Electronic conductivity can be easily determined by performing chronoamperometry on the same cell as the current collector and cables are typically electronically conductive but ionically insulating. After reaching steady-state, ions cannot be conducted across the current collector, effectively isolating the electronic conduction pathway.

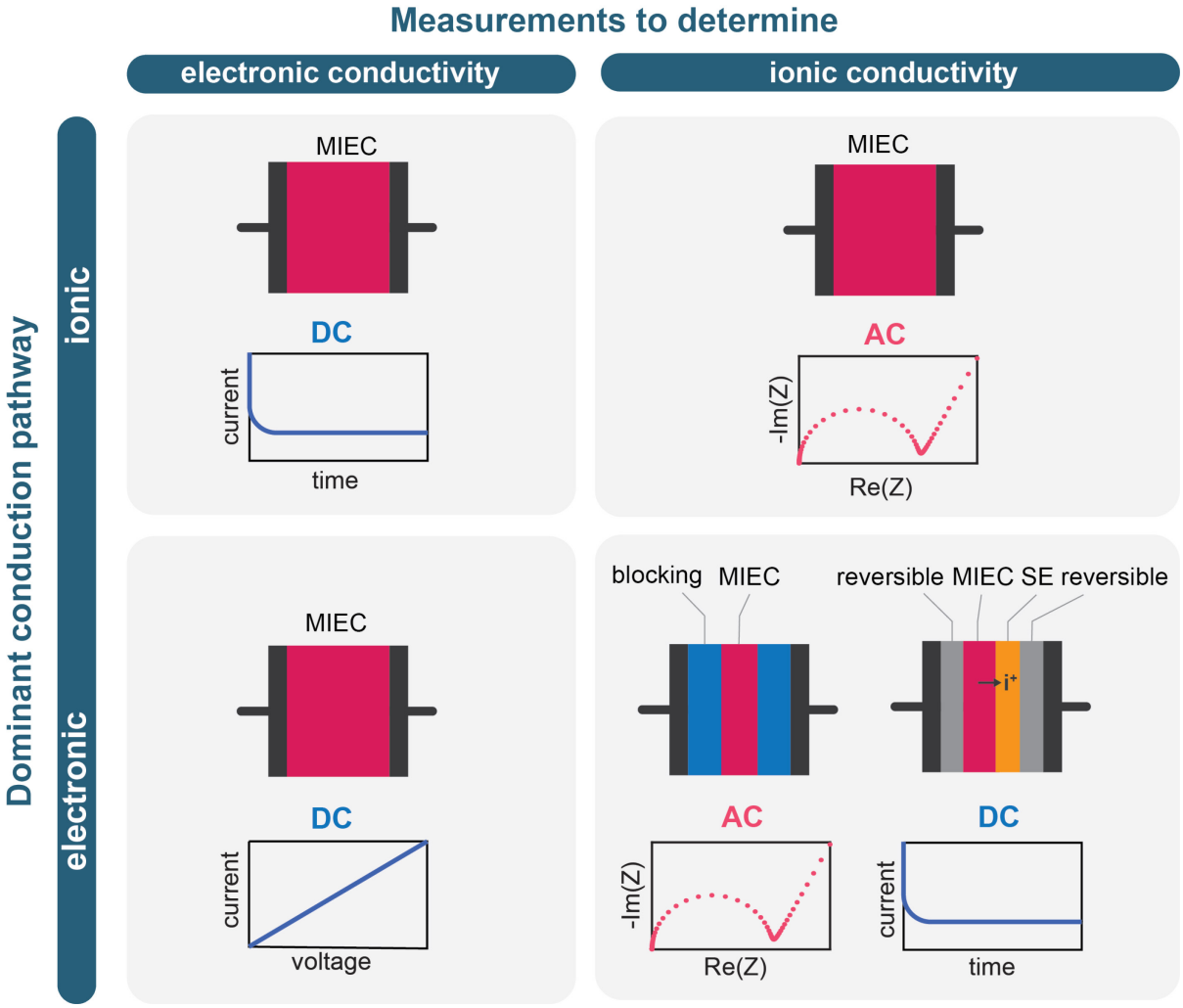

Figure 1-8. Overview of measurement techniques to isolate either the ionic or electronic conductivity for mixed MOFs conductors with mismatched ionic and electronic conduction pathways. Cell setups and expected (simulated) data are shown as well as the direction of ion (i^+) transport where applicable.

If the electronic conductivity dominates, blocking electrodes must be employed to isolate the ionic transport. In the AC variation, the MOF is symmetrically sandwiched between solid electrolytes that can conduct ions but are electronically blocking. The measured current thus only stems from ion transport. The thicknesses of the blocking layers and MOF layer should be chosen such that the blocking layers have higher ionic conductance and are non-limiting while still providing enough electronic resistance. The DC variation is a modified Hebb-Wagner setup:[62,65] A layer of solid electrolyte is inserted on only one side of the mixed

conductor pellet. These two layers are then sandwiched by symmetrical layers of reversible electrodes (e.g. Li metal for lithium conductors). A DC bias is applied across the cell such that ions are moving from reversible electrode to the mixed conductor, to solid electrolyte, and into the opposite reversible electrode. The DC polarization is held until a steady state current is reached and repeated over a range of bias voltages to ensure Ohmic transport. [62,65]

Adopting these techniques in the MOF field would allow for better characterization of mixed conductors with mismatched ionic and electronic conductivities. The greatest challenge in implementing these measurements for MOFs is to find appropriate materials to use as reversible electrodes as well as solid electrolytes. While many commercial reversible electrode and electrolyte materials are available for lithium and sodium, finding materials that are suitable for conducting magnesium, calcium, aluminum, etc. can be a difficult. Additionally, the interfacial contact between MOFs and other materials is often poor, inhibiting measurements for all-solid cells.

1.4.3 Mixed Transport in Electrode Materials for Energy Storage

Ion migration in electronically conductive electrode materials for energy storage can be viewed as mixed conductivity. Instead of only cations and electrons, both cations and anions are present in electronically conductive porous electrode materials. Only cations typically interact with the active electrode material to enable energy storage for batteries or supercapacitors.

In battery-like systems, ions must intercalate into materials and undergo oxidation and reduction reactions in typically slower processes. Here, the kinetics of ion insertion and migration within the electrode material can often be a limiting factor at fast cycling rates.[66,67] In supercapacitors, ions interact with the active material within the electrochemical double layer and make use of the internal or electrochemically accessible surface area of the material. Double layer capacitors can be formally distinguished from pseudocapacitors as they store charge purely by physical capacitance while pseudocapacitors have various amounts of redox contributions to their charge storage. Intercalation pseudocapacitance is a special case in which ions quickly intercalate into layered materials, enabling high power densities in line with other supercapacitors.[68–70]

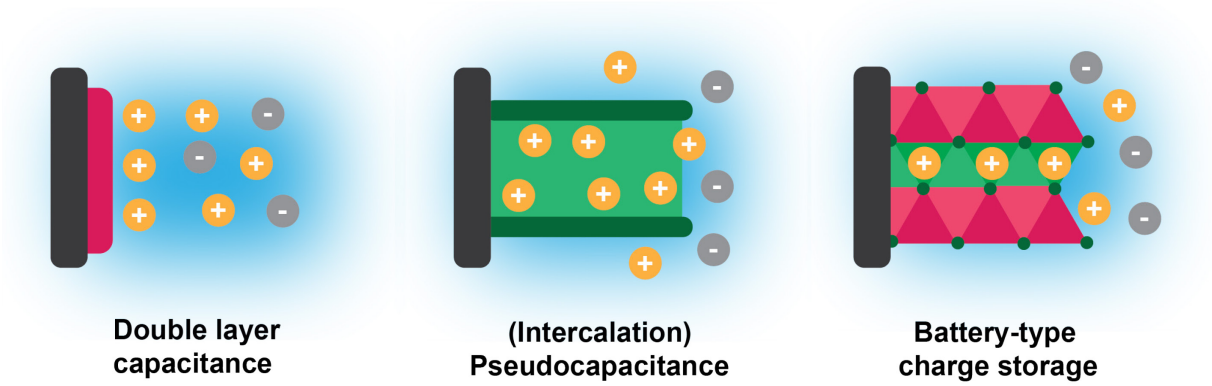

Figure 1-9. Charge storage mechanisms in comparison: A double layer capacitor stores charges through physical sorption. Battery-like systems undergo defined redox reactions during ion insertion. (Intercalation) pseudocapacitance occurs through a combination of often ill-defined surface redox reactions and double layer capacitance.

MOFs are privileged as supercapacitors due to their large accessible internal surface area. Ions preside in the pores in a solvated environment and interact with the material when polarized.[71] The insertion and transport of ions within the pore network is most likely dictated by similar principles as in MOF electrolytes and greatly affects the energy storage process. The same is expected for layered intercalation pseudocapacitive electrode material where the rate of ions insertion between layers may affect rate performance. For example, ions may not be able to intercalate into the center of each grain at high cycling rates, effectively using only accessing a small portion of the theoretical capacitance.

The exact mechanisms for pseudocapacitors are still not fully understood as a combination of redox and physical capacitance is at play. The specific interactions between ions and MOF electrode, both transport in the pores and faradaic reactions with specific molecular moieties remain blurry. In any case, ion transport within the active electronically conductive electrode material is a key process that has a great impact on the overall performance and power density of the cell. Understanding the interplay of ion transport, electron transport and possible faradaic interactions is required to optimize porous supercapacitors.

1.5 References

(1) Furukawa, H.; Ko, N.; Go, Y. B.; Aratani, N.; Choi, S. B.; Choi, E.; Yazaydin, A. Ö.; Snurr, R. Q.; O'Keeffe, M.; Kim, J.; Yaghi, O. M. Ultrahigh Porosity in Metal-Organic Frameworks. *Science* **2010**, *329* (5990), 424–428.

(2) Skorupskii, G.; Le, K. N.; Cordova, D. L. M.; Yang, L.; Chen, T.; Hendon, C. H.; Arguilla, M. Q.; Dincă, M. Porous Lanthanide Metal–Organic Frameworks with Metallic Conductivity. *PNAS* **2022**, *119* (34), e2205127119.

(3) Takenaka, T.; Ishihara, K.; Roppongi, M.; Miao, Y.; Mizukami, Y.; Makita, T.; Tsurumi, J.; Watanabe, S.; Takeya, J.; Yamashita, M.; Torizuka, K.; Uwatoko, Y.; Sasaki, T.; Huang, X.; Xu, W.; Zhu, D.; Su, N.; Cheng, J. G.; Shibauchi, T.; Hashimoto, K. Strongly Correlated Superconductivity in a Copper-Based Metal-Organic Framework with a Perfect Kagome Lattice. *Science Adv.* **2021**, *7* (12), 3996–4013.

(4) Li, J.; Ott, S. The Molecular Nature of Redox-Conductive Metal-Organic Frameworks. *Acc. Chem. Res.* **2024**, *57* (19), 2836–2846.

(5) Xie, L. S.; Skorupskii, G.; Dincă, M. Electrically Conductive Metal-Organic Frameworks. *Chem. Rev.* **2020**, *120* (16), 8536–8580.

(6) Hmadeh, M.; Lu, Z.; Liu, Z.; Gándara, F.; Furukawa, H.; Wan, S.; Augustyn, V.; Chang, R.; Liao, L.; Zhou, F.; Perre, E.; Ozolins, V.; Suenaga, K.; Duan, X.; Dunn, B.; Yamamto, Y.; Terasaki, O.; Yaghi, O. M. New Porous Crystals of Extended Metal-Catecholates. *Chem. Mater.* **2012**, *24* (18), 3511–3513.

(7) Campbell, M. G.; Sheberla, D.; Liu, S. F.; Swager, T. M.; Dincə, M. Cu3(Hexaiminotriphenylene)2: An Electrically Conductive 2D Metal–Organic Framework for Chemiresistive Sensing. *Angew. Chem. Intl. Ed.* **2015**, *54* (14), 4349–4352.

(8) Sheberla, D.; Sun, L.; Blood-Forsythe, M. A.; Er, S.; Wade, C. R.; Brozek, C. K.; Aspuru-Guzik, A.; Dincă, M. High Electrical Conductivity in Ni_3(2,3,6,7,10,11-Hexaiminotriphenylene)$_2$, a Semiconducting Metal-Organic Graphene Analogue. *J. Am. Chem. Soc.* **2014**, *136* (25), 8859–8862.

(9) Park, J.; Hinckley, A. C.; Huang, Z.; Feng, D.; Yakovenko, A. A.; Lee, M.; Chen, S.; Zou, X.; Bao, Z. Synthetic Routes for a 2D Semiconductive Copper Hexahydroxybenzene Metal-Organic Framework. *J. Am. Chem. Soc.* **2018**, *140* (44), 14533–14537.

(10) Dou, J. H.; Sun, L.; Ge, Y.; Li, W.; Hendon, C. H.; Li, J.; Gul, S.; Yano, J.; Stach, E. A.; Dincă, M. Signature of Metallic Behavior in the Metal-Organic Frameworks M_3(Hexaiminobenzene)$_2$ (M = Ni, Cu). *J. Am. Chem. Soc.* **2017**, *139* (39), 13608–13611.

(11) Nagatomi, H.; Yanai, N.; Yamada, T.; Shiraishi, K.; Kimizuka, N. Synthesis and Electric Properties of a Two-Dimensional Metal-Organic Framework Based on Phthalocyanine. *Chem. Eur. J.* **2018**, *24* (8), 1806–1810.

(12) Meng, Z.; Luo, J.; Li, W.; Mirica, K. A. Hierarchical Tuning of the Performance of Electrochemical Carbon Dioxide Reduction Using Conductive Two-Dimensional Metallophthalocyanine Based Metal-Organic Frameworks. *J. Am. Chem. Soc.* **2020**, *142* (52), 21656–21669.

(13) Xing, G.; Liu, J.; Zhou, Y.; Fu, S.; Zheng, J. J.; Su, X.; Gao, X.; Terasaki, O.; Bonn, M.; Wang, H. I.; Chen, L. Conjugated Nonplanar Copper-Catecholate Conductive Metal-Organic Frameworks via Contorted Hexabenzocoronene Ligands for Electrical Conduction. *J. Am. Chem. Soc.* **2023**, *145* (16), 8979–8987.

(14) Skorupskii, G.; Trump, B. A.; Kasel, T. W.; Brown, C. M.; Hendon, C. H.; Dincă, M. Efficient and Tunable One-Dimensional Charge Transport in Layered Lanthanide Metal–Organic Frameworks. *Nat. Chem.* **2020**, *12* (2), 131–136.

(15) Lu, Y.; Zhang, Y.; Yang, C. Y.; Revuelta, S.; Qi, H.; Huang, C.; Jin, W.; Li, Z.; Vega-Mayoral, V.; Liu, Y.; Huang, X.; Pohl, D.; Položij, M.; Zhou, S.; Cánovas, E.; Heine, T.; Fabiano, S.; Feng, X.; Dong, R. Precise Tuning of Interlayer Electronic Coupling in Layered Conductive Metal-Organic Frameworks. *Nat. Comm.* **2022**, *13* (1), 1–7.

(16) Chen, T.; Dou, J. H.; Yang, L.; Sun, C.; Libretto, N. J.; Skorupskii, G.; Miller, J. T.; Dincă, M. Continuous Electrical Conductivity Variation in M_3(Hexaiminotriphenylene)$_2$ (M = Co, Ni, Cu) MOF Alloys. *J. Am. Chem. Soc.* **2020**, *142* (28), 12367–12373.

(17) Yin, J. C.; Lian, X.; Li, Z. G.; Cheng, M.; Liu, M.; Xu, J.; Li, W.; Xu, Y.; Li, N.; Bu, X. H. Triazacoronene-Based 2D Conductive Metal–Organic Framework for High-Capacity Lithium Storage. *Adv. Func. Mater.* **2024**, *34* (41), 2403656.

(18) Wang, J.; Chen, T.; Jeon, M.; Oppenheim, J. J.; Tan, B.; Kim, J.; Dincă, M. Superior Charge Transport in Ni-Diamine Conductive MOFs. *J. Am. Chem. Soc.* **2024**, *146* (29), 20500–20507.

(19) Sheberla, D.; Sun, L.; Blood-Forsythe, M. A.; Er, S.; Wade, C. R.; Brozek, C. K.; Aspuru-Guzik, A.; Dincă, M. High Electrical Conductivity in Ni_3(2,3,6,7,10,11-Hexaiminotriphenylene)$_2$, a Semiconducting Metal-Organic Graphene Analogue. *J. Am. Chem. Soc.* **2014**, *136* (25), 8859–8862.

(20) Kharod, R. A.; Andrews, J. L.; Dinca, M. Teaching Metal-Organic Frameworks to Conduct: Ion and Electron Transport in Metal-Organic Frameworks. *Annu. Rev. Mater. Res.* **2022**, *52*, 103–128.

(21) Sadakiyo, M.; Yamada, T.; Kitagawa, H. Rational Designs for Highly Proton-Conductive Metal-Organic Frameworks. *J. Am. Chem. Soc.* **2009**, *131* (29), 9906–9907.

(22) Lim, D. W.; Sadakiyo, M.; Kitagawa, H. Proton Transfer in Hydrogen-Bonded Degenerate Systems of Water and Ammonia in Metal–Organic Frameworks. *Chem. Sci.* **2018**, *10* (1), 16–33.

(23) Zhang, F. M.; Dong, L. Z.; Qin, J. S.; Guan, W.; Liu, J.; Li, S. L.; Lu, M.; Lan, Y. Q.; Su, Z. M.; Zhou, H. C. Effect of Imidazole Arrangements on Proton-Conductivity in Metal-Organic Frameworks. *J. Am. Chem. Soc.* **2017**, *139* (17), 6183–6189.

(24) Dybtsev, D. N.; Ponomareva, V. G.; Aliev, S. B.; Chupakhin, A. P.; Gallyamov, M. R.; Moroz, N. K.; Kolesov, B. A.; Kovalenko, K. A.; Shutova, E. S.; Fedin, V. P. High Proton Conductivity and Spectroscopic Investigations of Metal-Organic Framework Materials Impregnated by Strong Acids. *ACS Appl. Mater. Interfaces* **2014**, *6* (7), 5161–5167.

(25) Ponomareva, V. G.; Kovalenko, K. A.; Chupakhin, A. P.; Dybtsev, D. N.; Shutova, E. S.; Fedin, V. P. Imparting High Proton Conductivity to a Metal-Organic Framework Material by Controlled Acid Impregnation. *J. Am. Chem. Soc.* **2012**, *134* (38), 15640–15643.

(26) Phang, W. J.; Jo, H.; Lee, W. R.; Song, J. H.; Yoo, K.; Kim, B.; Hong, C. S. Superprotonic Conductivity of a UiO-66 Framework Functionalized with Sulfonic Acid Groups by Facile Postsynthetic Oxidation. *Angew. Chem. Intl. Ed.* **2015**, *54* (17), 5142–5146.

(27) Rought, P.; Marsh, C.; Pili, S.; Silverwood, I. P.; Sakai, V. G.; Li, M.; Brown, M. S.; Argent, S. P.; Vitorica-Yrezabal, I.; Whitehead, G.; Warren, M. R.; Yang, S.; Schröder, M. Modulating Proton Diffusion and Conductivity in Metal–Organic Frameworks by Incorporation of Accessible Free Carboxylic Acid Groups. *Chem. Sci.* **2019**, *10* (5), 1492–1499.

(28) Taylor, J. M.; Dawson, K. W.; Shimizu, G. K. H. A Water-Stable Metal-Organic Framework with Highly Acidic Pores for Proton-Conducting Applications. *J. Am. Chem. Soc.* **2013**, *135* (4), 1193–1196.

(29) Jeong, N. C.; Samanta, B.; Lee, C. Y.; Farha, O. K.; Hupp, J. T. Coordination-Chemistry Control of Proton Conductivity in the Iconic Metal-Organic Framework Material HKUST-1. *J. Am. Chem. Soc.* **2012**, *134* (1), 51–54.

(30) Ramaswamy, P.; Wong, N. E.; Shimizu, G. K. H. MOFs as Proton Conductors – Challenges and Opportunities. *Chem. Soc. Rev.* **2014**, *43* (16), 5913–5932.

(31) Kreuer, K. -D; Rabenau, A.; Weppner, W. Vehicle Mechanism, A New Model for the Interpretation of the Conductivity of Fast Proton Conductors. *Angew. Chem. Intl. Ed.* **1982**, *21* (3), 208–209.

(32) Agmon, N. The Grotthuss Mechanism. *Chem. Phys. Lett.* **1995**, *244* (5–6), 456–462.

(33) Tian, L.; Xu, X.; Liu, M.; Liu, Z.; Liu, Z. Significantly Enhancing the Lithium Ionic Conductivity of Metal-Organic Frameworks via a Postsynthetic Modification Strategy. *Langmuir* **2021**, *37* (13), 3922–3928.

(34) Zettl, R.; Lunghammer, S.; Gadermaier, B.; Boulaoued, A.; Johansson, P.; Wilkening, H. M. R.; Hanzu, I. High Li^+ and Na^+ Conductivity in New Hybrid Solid Electrolytes Based on the Porous MIL-121 Metal Organic Framework. *Adv. Energy Mater.* **2021**, *11* (16), 2003542.

(35) Miner, E. M.; Park, S. S.; Dincă, M. High Li^+ and Mg^{2+} Conductivity in a Cu-Azolate Metal-Organic Framework. *J. Am. Chem. Soc.* **2019**, *141* (10), 4422–4427.

(36) Ameloot, R.; Aubrey, M.; Wiers, B. M.; Gõmora-Figueroa, A. P.; Patel, S. N.; Balsara, N. P.; Long, J. R. Ionic Conductivity in the Metal–Organic Framework UiO-66 by Dehydration and Insertion of Lithium Tert-Butoxide. *Chem. Eur. J.* **2013**, *19* (18), 5533–5536.

(37) Duan, X.; Ouyang, Y.; Zeng, Q.; Ma, S.; Kong, Z.; Chen, A.; He, Z.; Yang, T.; Zhang, Q. Two Carboxyl-Decorated Anionic Metal-Organic Frameworks as Solid-State Electrolytes Exhibiting High Li^+ and Zn^{2+} Conductivity. *Inorg. Chem.* **2021**, *60* (15), 11032–11037.

(38) Iliescu, A.; Andrews, J. L.; Oppenheim, J. J.; Dincă, M. A Solid Zn-Ion Conductor from an All-Zinc Metal-Organic Framework Replete with Mobile Zn^{2+} Cations. *J. Am. Chem. Soc.* **2023**, *145* (48), 25962–25965.

(39) Park, S. S.; Tulchinsky, Y.; Dinca, M. Single-Ion Li^+, Na^+, and Mg^{2+} Solid Electrolytes Supported by a Mesoporous Anionic Cu-Azolate Metal-Organic Framework. *J. Am. Chem. Soc.* **2017**, *139* (38), 13260–13263.

(40) Lu, W. G.; Jiang, L.; Feng, X. L.; Lu, T. B. Three-Dimensional Lanthanide Anionic Metal - Organic Frameworks with Tunable Luminescent Properties Induced by Cation Exchange. *Inorg. Chem.* **2009**, *48* (15), 6997–6999.

(41) Procopio, E. Q.; Linares, F.; Montoro, C.; Colombo, V.; Maspero, A.; Barea, E.; Navarro, J. A. R. Cation-Exchange Porosity Tuning in Anionic Metal–Organic Frameworks for the Selective Separation of Gases and Vapors and for Catalysis. *Angew. Chem. Intl. Ed.* **2010**, *49* (40), 7308–7311.

(42) Xu, K. Nonaqueous Liquid Electrolytes for Lithium-Based Rechargeable Batteries. *Chem. Rev.* **2004**, *104* (10), 4303–4417.

(43) Bachman, J. C.; Muy, S.; Grimaud, A.; Chang, H. H.; Pour, N.; Lux, S. F.; Paschos, O.; Maglia, F.; Lupart, S.; Lamp, P.; Giordano, L.; Shao-Horn, Y. Inorganic Solid-State Electrolytes for Lithium Batteries: Mechanisms and Properties Governing Ion Conduction. *Chem. Rev.* **2016**, *116* (1), 140–162.

(44) Lou, S.; Liu, Q.; Zhang, F.; Liu, Q.; Yu, Z.; Mu, T.; Zhao, Y.; Borovilas, J.; Chen, Y.; Ge, M.; Xiao, X.; Lee, W. K.; Yin, G.; Yang, Y.; Sun, X.; Wang, J. Insights into Interfacial Effect and Local Lithium-Ion Transport in Polycrystalline Cathodes of Solid-State Batteries. *Nat. Comm.* **2020**, *11* (1), 1–10.

(45) Knauth, P. Inorganic Solid Li Ion Conductors: An Overview. *Solid State Ionics* **2009**, *180* (14–16), 911–916.

(46) Dahbi, M.; Ghamouss, F.; Tran-Van, F.; Lemordant, D.; Anouti, M. Comparative Study of EC/DMC LiTFSI and $LiPF_6$ Electrolytes for Electrochemical Storage. *J. Power Sources* **2011**, *196* (22), 9743–9750.

(47) Thomas, J. A.; McGaughey, A. J. H. Reassessing Fast Water Transport through Carbon Nanotubes. *Nano Lett.* **2008**, *8* (9), 2788–2793.

(48) Zhang, H.; Ye, H.; Zheng, Y.; Zhang, Z. Prediction of the Viscosity of Water Confined in Carbon Nanotubes. *Microfluid. Nanofluidics* **2011**, *10* (2), 403–414.

(49) Babu, J. S.; Sathian, S. P. The Role of Activation Energy and Reduced Viscosity on the Enhancement of Water Flow through Carbon Nanotubes. *J. Chem. Phys.* **2011**, *134* (19), 194509.

(50) Mo, R. J.; Chen, S.; Huang, L. Q.; Ding, X. L.; Rafique, S.; Xia, X. H.; Li, Z. Q. Regulating Ion Affinity and Dehydration of Metal-Organic Framework Sub-Nanochannels for High-Precision Ion Separation. *Nat. Comm.* **2024**, *15* (1), 1–10.

(51) Lu, J.; Zhang, H.; Hou, J.; Li, X.; Hu, X.; Hu, Y.; Easton, C. D.; Li, Q.; Sun, C.; Thornton, A. W.; Hill, M. R.; Zhang, X.; Jiang, G.; Liu, J. Z.; Hill, A. J.; Freeman, B. D.; Jiang, L.; Wang, H. Efficient Metal Ion Sieving in Rectifying Subnanochannels Enabled by Metal–Organic Frameworks. *Nat. Mater.* **2020**, *19* (7), 767–774.

(52) Paulsen, B. D.; Tybrandt, K.; Stavrinidou, E.; Rivnay, J. Organic Mixed Ionic–Electronic Conductors. *Nat. Mater.* **2020**, *19* (1), 13–26.

(53) Sunarso, J.; Baumann, S.; Serra, J. M.; Meulenberg, W. A.; Liu, S.; Lin, Y. S.; Diniz da Costa, J. C. Mixed Ionic–Electronic Conducting (MIEC) Ceramic-Based Membranes for Oxygen Separation. *J. Membr. Sci.* **2008**, *320* (1–2), 13–41.

(54) Ribeiro, C.; Tan, B.; Figueira, F.; Mendes, R. F.; Calbo, J.; Valente, G.; Escamilla, P.; Paz, F. A. A.; Rocha, J.; Dincă, M.; Souto, M. Mixed Ionic and Electronic Conductivity

in a Tetrathiafulvalene-Phosphonate Metal-Organic Framework. *J. Am. Chem. Soc.* **2024**, *147*, 48.

(55) Choi, J. Y.; Stodolka, M.; Kim, N.; Pham, H. T. B.; Check, B.; Park, J. 2D Conjugated Metal-Organic Framework as a Proton-Electron Dual Conductor. *Chem* **2023**, *9* (1), 143–153.

(56) Su, J.; He, W.; Li, X. M.; Sun, L.; Wang, H. Y.; Lan, Y. Q.; Ding, M.; Zuo, J. L. High Electrical Conductivity in a 2D MOF with Intrinsic Superprotonic Conduction and Interfacial Pseudo-Capacitance. *Matter* **2020**, *2* (3), 711–722.

(57) Rambabu, D.; Goossens, T.; Bakuru, V. R.; Apostol, P.; Mairesse, F.; Steenhaut, T.; Beaujean, P.; Mondal, S. K.; Guo, X.; Zhang, Y.; Pal, S.; Markowski, R.; Lin, X.; Xu, P.; Chanteux, G.; Kachmar, A.; Tie, D.; Ramackers, A.; Frano, V.; Robeyns, K.; Kumar Maji, T.; Filinchuk, Y.; Champagne, B.; Vlad, A. Mixed Proton-Electron Conductivity in a Dynamic 3D Metal-Organic Framework. *Chem* **2025**, 102590.

(58) Su, J.; He, W.; Li, X. M.; Sun, L.; Wang, H. Y.; Lan, Y. Q.; Ding, M.; Zuo, J. L. High Electrical Conductivity in a 2D MOF with Intrinsic Superprotonic Conduction and Interfacial Pseudo-Capacitance. *Matter* **2020**, *2* (3), 711–722.

(59) He, X. L.; Shao, B.; Huang, R. K.; Dong, M.; Tong, Y. Q.; Luo, Y.; Meng, T.; Yang, F. J.; Zhang, Z.; Huang, J. A Mixed Protonic–Electronic Conductor Base on the Host–Guest Architecture of 2D Metal–Organic Layers and Inorganic Layers. *Adv. Sci.* **2023**, *10* (17), 2205944.

(60) Zhang, K. J.; Chen, T.; Oppenheim, J. J.; Yang, L.; Palatinus, L.; Müller, P.; Van Voorhis, T.; Dincă, M. High-Resolution Structure of $Zn_3(HOTP)_2$ (HOTP = Hexaoxidotriphenylene), a Three-Dimensional Conductive MOF. *Chem. Sci.* **2025**.

(61) Choi, J. Y.; Stodolka, M.; Kim, N.; Pham, H. T. B.; Check, B.; Park, J. 2D Conjugated Metal-Organic Framework as a Proton-Electron Dual Conductor. *Chem* **2023**, *9* (1), 143–153.

(62) Riess, I. Measurement of Ionic Conductivity in Semiconductors and Metals. *Solid State Ionics* **1991**, *44* (3–4), 199–205.

(63) Riess, I. Mixed Ionic–Electronic Conductors—Material Properties and Applications. *Solid State Ionics* **2003**, *157* (1–4), 1–17.

(64) Huggins, R. A. Simple Method to Determine Electronic Conductivity and Ionic Components of the Conductors in Mixed a Review. *Ionics (Kiel)* **2002**, *8* (3–4), 300–313.

(65) Riess, I. Review of the Limitation of the Hebb-Wagner Polarization Method for Measuring Partial Conductivities in Mixed Ionic Electronic Conductors. *Solid State Ionics* **1996**, *91* (3–4), 221–232.

(66) Zhang, H.; Yu, X.; Braun, P. V. Three-Dimensional Bicontinuous Ultrafast-Charge and-Discharge Bulk Battery Electrodes. *Nat. Nanotechnol.* **2011**, *6* (5), 277–281.

(67) Ye, J.; Baumgaertel, A. C.; Wang, Y. M.; Biener, J.; Biener, M. M. Structural Optimization of 3D Porous Electrodes for High-Rate Performance Lithium Ion Batteries. *ACS Nano* **2015**, *9* (2), 2194–2202.

(70) Park, M.; Zhang, X.; Chung, M.; Less, G. B.; Sastry, A. M. A Review of Conduction Phenomena in Li-Ion Batteries. *J. Power Sources* **2010**, *195* (24), 7904–7929.

(68) Liu, Y.; Jiang, S. P.; Shao, Z. Intercalation Pseudocapacitance in Electrochemical Energy Storage: Recent Advances in Fundamental Understanding and Materials Development. *Mater. Today Adv.* **2020**, *7*, 100072.

(69) Bhojane, P. Recent Advances and Fundamentals of Pseudocapacitors: Materials, Mechanism, and Its Understanding. *J. Energy Storage* **2022**, *45*, 103654.

(71) Bi, S.; Banda, H.; Chen, M.; Niu, L.; Chen, M.; Wu, T.; Wang, J.; Wang, R.; Feng, J.; Chen, T.; Dincă, M.; Kornyshev, A. A.; Feng, G. Molecular Understanding of Charge Storage and Charging Dynamics in Supercapacitors with MOF Electrodes and Ionic Liquid Electrolytes. *Nat. Mater.* **2020**, *19* (5), 552–558.

Chapter 2

Cation and Vacancy Engineering Reveals Coexistence of Liquid- and Solid-Like Ion Transport in Metal-organic Frameworks

2.1 Abstract

Metal-organic frameworks (MOFs) are emerging as unique (pseudo-)solid state electrolytes that enable transport of technologically relevant cations such as Li^+, Na^+, K^+, Mg^{2+}, Zn^{2+} and Sr^{2+}. As solids, they should be subject to the compositional and structural engineering approaches that are common to traditional solid-state electrolytes. Yet, they also contain liquid within their pores. As such, cations may benefit from sampling both solid and liquid-like transport regimes. Here, we show that Li^+, Na^+, K^+, Mg^{2+}, Zn^{2+} and Sr^{2+} ions are mobile in the cation-exchangeable anionic MOF $[Cu_3(\mu_3\text{-OH})(\text{pyrazole-4-carboxylate})_3]^-$, with conductivity values spanning from 4.3×10^{-6} S/cm for Zn^{2+} to 1.7×10^{-3} S/cm for K^+. Experiments aimed at probing the effects of solvated ion radii, interaction with the host framework, charge carrier concentration, and vacancy sites on ionic conductivity and activation energy for individual ions demonstrate that, indeed, transport of ions in MOFs should be thought of as a combination of direct interaction with the framework, as well as liquid-like transport in the pores.

2.2 Introduction

Despite the enormous success of rechargeable lithium-ion batteries, a push towards more sustainable technologies has driven the development of alternative battery chemistries based on more abundant ions, including sodium, magnesium, and zinc.[1] A parallel emerging interest lies in replacing toxic and flammable organic electrolytes with aqueous or solid-state electrolytes.[2–5] Nevertheless, the often sluggish ion transport kinetics in the solid state present a bottleneck for achieving high energy densities.[6] To address this issue, microporous materials can provide a (pseudo-)solid-state platform in which ions may exist in a locally solvated environment within the pores, but macroscopically the materials behave as free-flowing powders. This unique middle-ground allows for potentially combining the beneficial attributes of both solid and liquid electrolytes, namely enhanced safety and stability due to the solid phase and enhanced ion mobility and reduced activation barriers due to ion solvation. However, a fundamental framework for understanding ion conduction in these porous systems is only just emerging, as systematic studies probing the ion transport on an atomic or molecular level have been scarce.[7–11]

Metal-organic frameworks (MOFs) are especially suited to facilitate solvated ion transport since the ordered pore systems can host exchangeable guest species and facilitate efficient mass transport. For neutral MOFs, this is accomplished by introducing stationary anionic groups that can host charge-balancing mobile cations and act as hopping sites.[8,12–14] Similarly, ligand-based deprotonated acidic moieties can host counter cations and serve as hopping sites.[15–17] However, low charge carrier and hopping site densities are often compensated by over-stoichiometric amounts of salt that lead to low cation transference numbers. More attractively, intrinsically anionic MOFs feature stoichiometric cations in the as-synthesized state that are easily exchanged under mild conditions and replaced by electrolyte ions.[18] The controlled stoichiometry and defined sites of anionic MOFs allow us to extract information about ion-framework interactions and gain insight into the mechanisms of ion transport. Herein, we investigate a cation exchangeable anionic MOF, competent for the conduction of various mono- and divalent metal ions – Li^+, Na^+, K^+, Mg^{2+}, Zn^{2+} and Sr^{2+} – to understand the factors influencing ion transport in porous materials.

2.3 Results and Discussion

Synthesis and Ion Exchange

The anionic MOF $NH_4[Cu_3(\mu_3\text{-}OH)(PyC)_3]$ (**1-NH$_4$**; PyC = pyrazolate-4-carboxylate) was synthesized according to a previously reported procedure.[19] The as-synthesized material features interconnected cages with two charge-balancing ammonium cations per cage (**Figure 2-1**). Given its formula, **1-NH$_4$** is expected to exchange up to one equivalent of Li^+, Na^+, K^+ ions or half an equivalent of Mg^{2+}, Zn^{2+}, or Sr^{2+} ions.

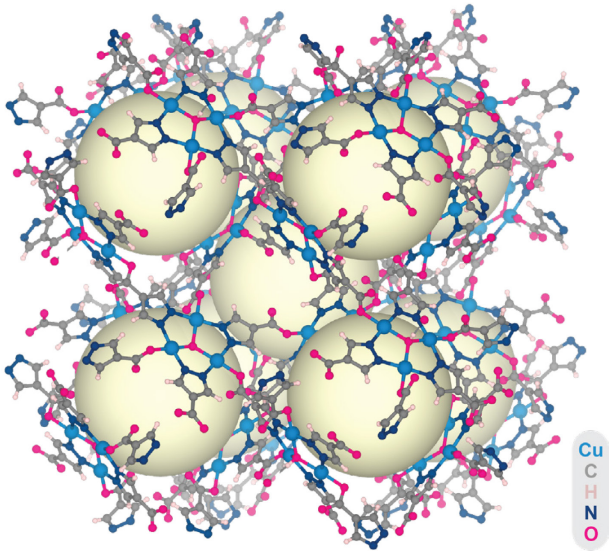

Figure 2-1. Structure of $[Cu_3(\mu_3\text{-}OH)(\text{pyrazole-4-carboxylate})_3]^-$. Yellow spheres represent solvent filled cavities.

Table 2-3. ICP-MS data and sum formulas for all samples reported. The molar ratio of SBU-Cu to mobile ion is given. Percent exchanged refers to the measured amount of mobile ion (versus SBU-Cu) compared to the theoretical stoichiometric exchange of ammonium to mobile ion.

Sample	Mobile ion	Measurement	Cu/ion molar ratio	Sum formula
	Li^+	Transference number	4.46	$Li_{0.67}(NH_4)_{0.33}[Cu_3(\mu_3\text{-}OH)(PyC)_3]$
1-Li	Li^+	VT conductivity	3.54	$Li_{0.85}(NH_4)_{0.15}[Cu_3(\mu_3\text{-}OH)(PyC)_3]$
1-Na	Na^+	VT conductivity	4.23	$Na_{0.75}(NH_4)_{0.25}[Cu_3(\mu_3\text{-}OH)(PyC)_3]$
1-K	K^+	VT conductivity	4.61	$K_{0.65}(NH_4)_{0.35}[Cu_3(\mu_3\text{-}OH)(PyC)_3]$
2-Mg	Mg^{2+}	VT conductivity, SC-XRD	6.43	$Mg_{0.47}(NH_4)_{0.06}[Cu_3(\mu_3\text{-}OH)(PyC)_3]$
2-Zn	Zn^{2+}	VT conductivity	5.14	$Zn_{0.50}[Cu_{2.93}Zn_{0.07}(\mu_3\text{-}OH)(PyC)_3]$
1-Sr	Sr^{2+}	VT conductivity	7.76	$Sr_{0.39}(NH_4)_{0.22}[Cu_3(\mu_3\text{-}OH)(PyC)_3]$

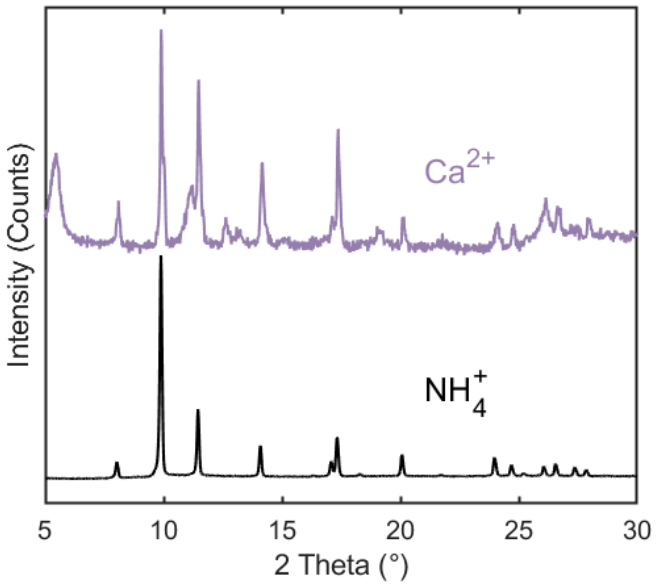

Figure 2-2. PXRD of a calcium exchanged sample in comparison to the as-synthesized **1-NH$_4$**.

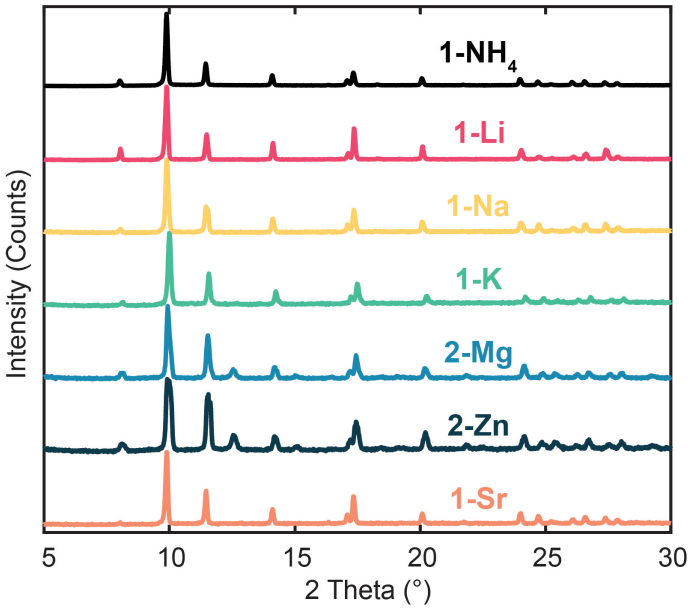

Figure 2-3. PXRD of as-synthesized **1-NH$_4$**, and of exchanged **1-Li**, **1-Na**, **1-K**, **2-Mg**, **2-Zn**, and **1-Sr.**

Thus, soaking **1-NH$_4$** in aqueous salt solutions of these ions at 45 °C for 10 days afforded cation-exchanged versions of the parent framework. The exchanged cation content of each material was determined by inductively coupled plasma mass spectrometry (ICP-MS) as a function of the ratio of charge-balancing cations to Cu atoms in the SBU. The sum formulas of ion-exchanged samples that were used for all subsequent measurements are summarized in **Table 2-1**. Attempts to isolate calcium-exchanged samples produced an unknown, likely lower

symmetry phase (**Figure 2-2**) while all other materials retained crystallinity, as confirmed by powder X-ray diffraction (PXRD) (**Figure 2-3**). PXRD analysis did however indicate that divalent ions Mg^{2+} and Zn^{2+} cause slight structural distortions. We will show later that these have a profound effect on conductivity. Mg- and Zn-exchanged materials are therefore denoted **2-Mg** and **2-Zn**, respectively, while the other materials are denoted **1-Li**, **1-Na**, **1-K**, and **1-Sr**.

Transport Measurements

The ionic conductivities of dry and free-flowing MOF powders were determined via electrochemical impedance spectroscopy (EIS) on symmetric cells with MOF electrolytes sandwiched between stainless steel plates (**Figure 2-18**). PXRD of the MOF powders post EIS confirmed the retention of crystallinity for all samples (**Figure 2-4**). We note that for all ion-exchanged samples discussed here, the ion conductivity values measured for different devices made from single batches are consistently within ±14% of the value reported here, allowing confidence in interpreting differences in conductivity between different ions.

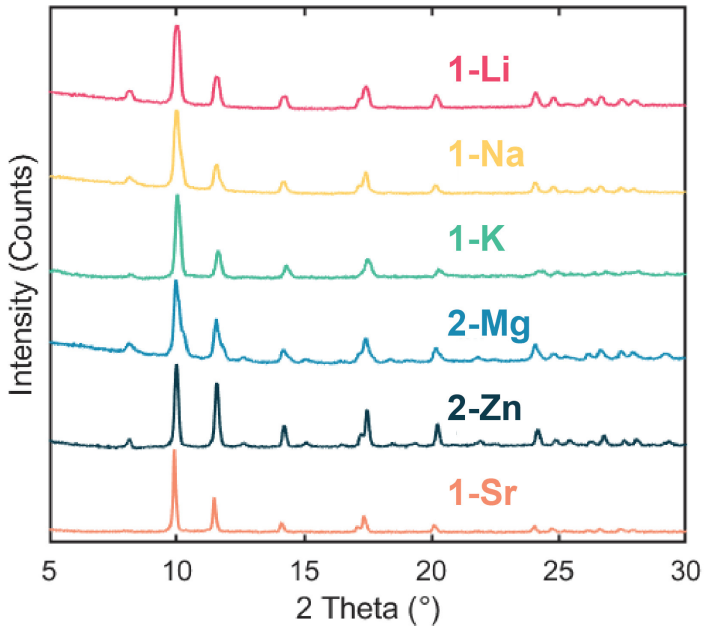

Figure 2-4. PXRD of materials post EIS measurements.

The conductivity of **1-Li** is 3.0×10^{-4} S/cm, which rivals the most conductive MOF-based electrolytes.[8,15,20–22] The sodium and potassium ion exchanged frameworks **1-Na** and **1-K** show higher conductivity than **1-Li**, reaching values of 5.8×10^{-4} S/cm and 1.7×10^{-3} S/cm, respectively (**Figure 2-5a**). These values are inversely proportional to the respective hydrated ionic radii in water.[23] Of note, **1-K** exhibits one of the largest K^+-ion conductivities for solids.[24,25] The room temperature ionic conductivities of **1-Sr**, **2-Mg,** and **2-Zn** are 1.5×10^{-5}

S/cm, 6.6 × 10^{-6} S/cm, and 4.3 × 10^{-6} S/cm, respectively (**Figure 2-5a**), continuing the trend of conductivity decreasing with increasing hydrated ionic radius.

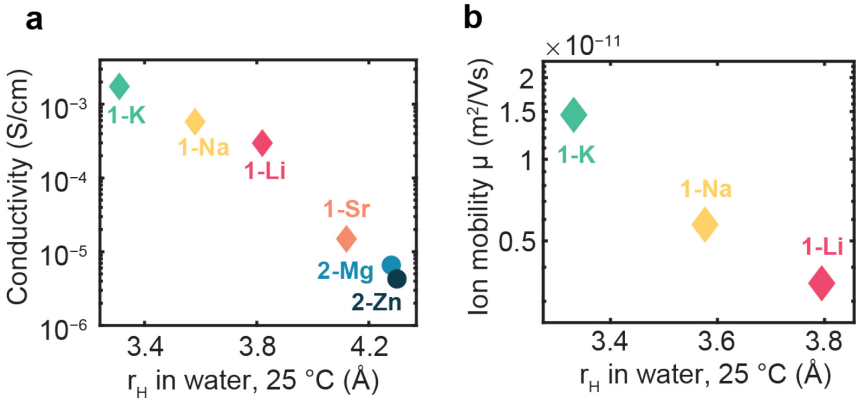

Figure 2-5. a) Ionic conductivities of cations in **1-Li**, **1-Na**, **1-K**, **1-Sr**, **2-Mg**, and **2-Zn** and b) mobilities of cations in **1-Li**, **1-Na** and **1-K**, plotted against the hydrated radii of the respective ions in water.[23]

Ion mobilities, μ, were calculated for **1-Li**, **1-Na**, and **1-K**, containing monovalent ions, to account for the difference in the mobile ion content in each of the isostructural samples:

$$\mu = \frac{\sigma}{qn} \tag{1}$$

where σ is the ionic conductivity, q is the ion charge, and n is the number of mobile charge carriers (assuming all lithium, sodium, and potassium ions are mobile). The ion mobilities, 0.32 × 10^{-11} m^2/Vs, 0.56 × 10^{-11} m^2/Vs, and 1.6 × 10^{-11} m^2/Vs for **1-Li**, **1-Na**, and **1-K**, respectively, are also inversely proportional to the hydrated ion sizes, suggesting that this trend is not a result of varying charge carrier concentration, but of their size (**Figure 2-5b**). This tendency appears to be contrary to alkali ion conduction in anionic frameworks with organic secondary electrolytes, where conductivities decrease in the order $Li^+ > Na^+ > K^+$.[15,26,27] Ion transport in framework **1** is thus governed by the movement of hydrated ions through intra-pore water, which resembles pure liquid electrolytes. In fact, as in pure liquid water, the ion with the lowest charge density, K^+ in this case, forms the smallest hydration shell, enabling the highest ion mobility and conductivity.[23,28]

Arrhenius-type fittings of variable temperature conductivity values yield activation energies of 0.40 eV, 0.41 eV, and 0.40 eV for **1-Li**, **1-Na,** and **1-K**, respectively. Higher activation energies are observed for **2-Mg** and **2-Zn**, both at 0.48. The activation energy measured for **1-Sr**, 0.27 eV, is significantly smaller than those of the other five materials (**Figure 2-18** and **2-19**).

Although Li^+, Na^+, K^+, Mg^{2+}, Zn^{2+} and Sr^{2+} ions are expected to be the major contributors to the overall ionic currents, sub-stoichiometric amounts of ion exchange under our defined conditions leave residual ammonium ions in the material.[29] We were able to measure the Li^+ ion transference number, t_{Li^+}, of a lithium-exchanged sample to determine the absolute contribution of just Li^+ ions to transport via potentiostatic polarization of a symmetric cell made from non-blocking electrodes on either side of a lithium-exchanged MOF pellet. Although Li metal is typically used as the non-blocking electrode in these measurements, it was not compatible here because **1-Li** is not stable against metallic Li. Instead, we reduced $Li_4Ti_5O_{12}$ using lithium naphthalenide[30] to produce $Li_{4+x}Ti_5O_{12}$ (R-LTO) and constructed symmetric R-LTO||MOF||R-LTO cells. Cells were polarized at 10 mV and subjected to EIS measurements (**Figures 2-6** and **2-7**).[30] The transference number was calculated according to the Bruce-Vincent method:[31]

$$t_{Li^+} = \frac{I_{ss}(\Delta V - I_0 R_0)}{I_0(\Delta V - I_{ss} R_{ss})} \quad (2)$$

where I_0, I_{ss}, R_0, and R_{ss} are the initial and post-steady state currents and resistances, respectively, and ΔV is the applied voltage. This analysis gave a high lithium transference number of $t_{Li^+} = 0.8$, confirming lithium ions as the major mobile species. With higher amounts of cation-exchange, this number is naturally expected to increase.

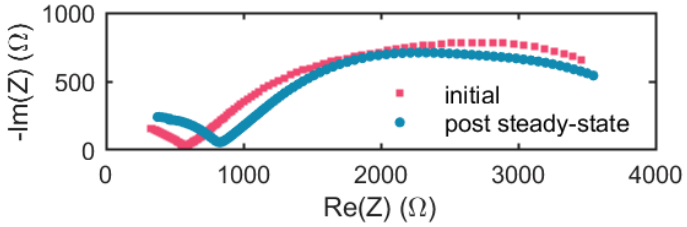

Figure 2-6. PEIS of a symmetric R-LTO||MOF||R-LTO cell before and after chronoamperometry.

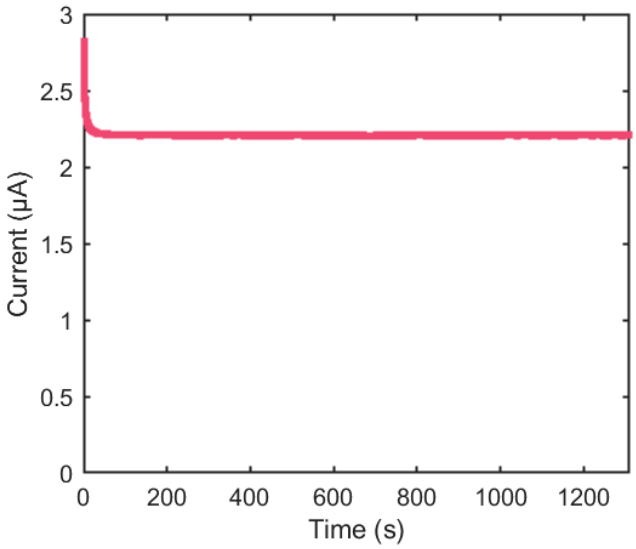

Figure 2-7. Chronoamperometry of a symmetric R-LTO||MOF||R-LTO cell, polarized at 10 mV.

Structural Characterization

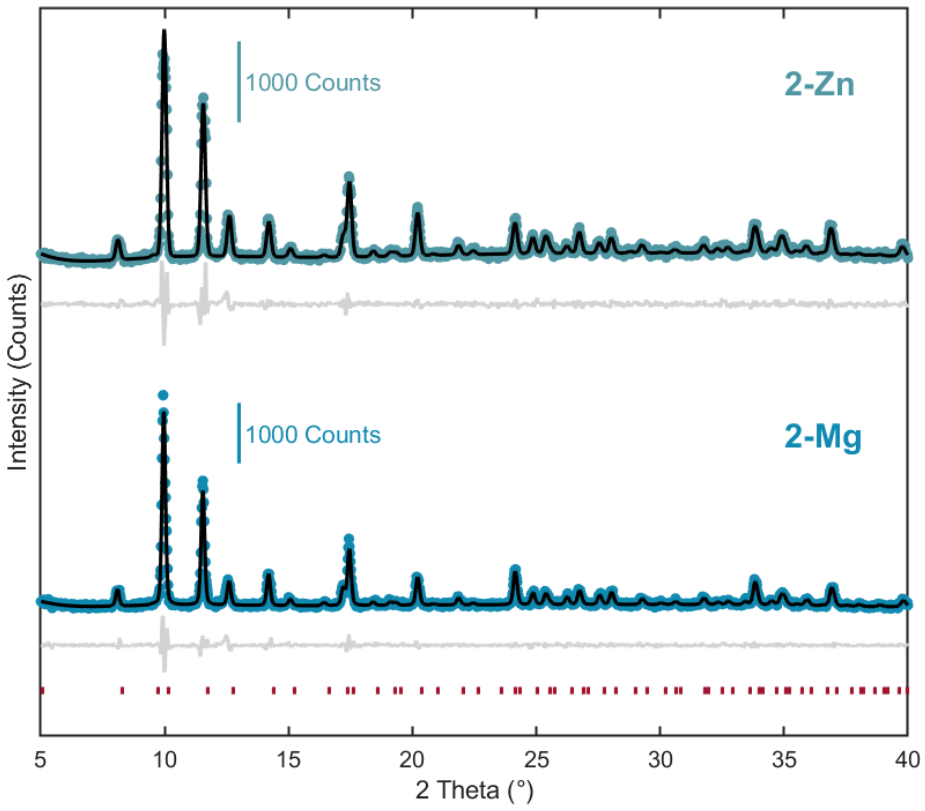

Figure 2-8. Pawley refinement of PXRD patterns **2-Mg** and **2-Sr** to space group $Fd\bar{3}$ (203). Colored circles: observed intensities; black lines: calculated intensities; grey lines: difference; red tick marks indicate calculated peak positions.

As mentioned above, **2-Mg** and **2-Zn** exhibit slightly modified PXRD patterns with additional reflections, most prominently the (331) reflection at 2θ = 12.7° (**Figure 2-3**). Although Pawley

refinement for **1-Li**, **1-Na**, **1-K** and **1-Sr** was conducted in the space group $Fd\bar{3}c$ with reflection condition *hhl*: $h, l = 2n$, the patterns for **2-Mg** and **2-Zn** cannot be refined in $Fd\bar{3}c$ due to the extra reflections violating the systematic absences. Thus, **2-Mg** and **2-Zn** were assigned to the lower symmetry space group $Fd\bar{3}$ (**Figures 2-8** and **2-9**).

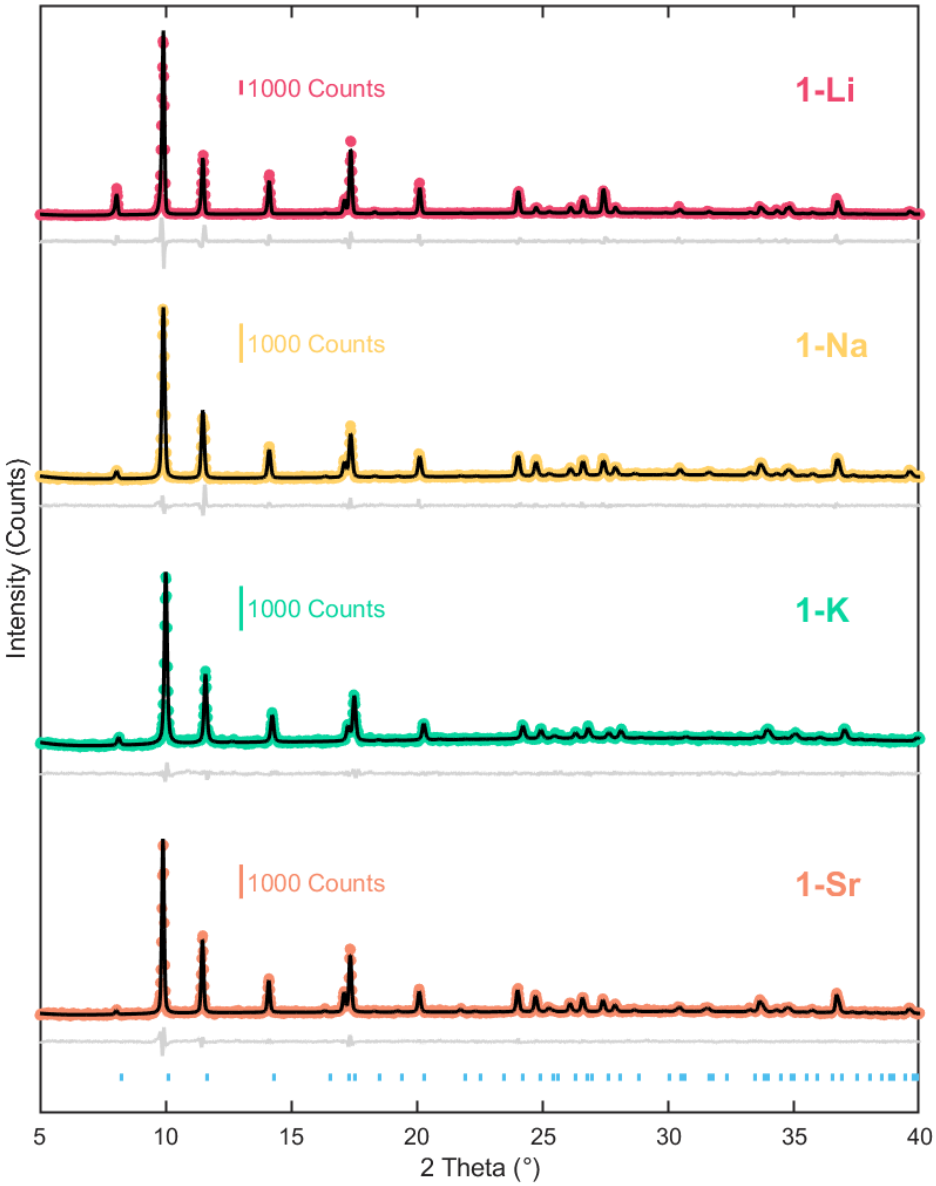

Figure 2-9. Pawley refinement of PXRD patterns for **1-Li**, **1-Na**, **1-K** and **1-Sr** to space group $Fd\bar{3}c$ (228). Colored circles: observed intensities; black lines: calculated intensities; grey lines: difference; blue tick marks indicate calculated peak positions.

Single crystal X-ray diffraction (SC-XRD) was performed on crystals of **1-K** and **2-Mg,** as representatives of the two structure types. Notably, both structures refine best in space group $Fd\bar{3}$ (**Figure 2-10**, see **Section 2.4.4** for structural and refinement parameters). Whereas carboxylate ligands bind at least partially in η^1-fashion to the Cu-SBU on both structures, **2-Mg** shows evidence of structural disorder that can be described by a combination of η^2 and η^1 binding modes. For this material, the asymmetric η^1 mode is refined as the majority component at 72% occupancy. Although the SC-XRD structure for **2-Mg** agrees with the PXRD data, we observe a discrepancy for **1-K**, as η^2 coordination is expected based on the higher symmetry PXRD pattern. We hypothesize that this discrepancy is a result of the high dynamicity of **1-K** due to the comparably weak interactions of K^+ ions with the framework which we will discuss later. Room temperature PXRD may show a high symmetry average of the dynamic η^1 coordination mode while SC-XRD at 100 K freezes the η^1 bonds.

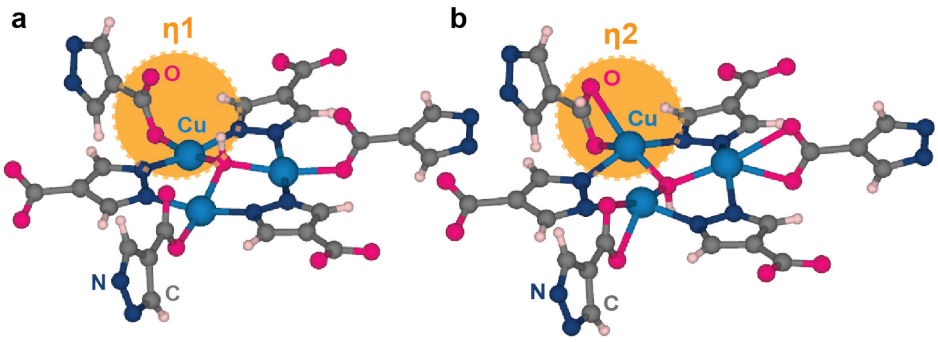

Figure 2-10. a) Single crystal structure of the SBU with asymmetric $\boldsymbol{\eta}^1$ coordination. This mode is refined as the sole component for **1-K** and the major component for **2-Mg** at 0.723(5) occupancy. b) A second minor structural component with symmetric $\boldsymbol{\eta}^2$ coordination was found for **2-Mg**.

We were able to observe Mg^{2+} ion position, which are highly relevant to ion transport, through SC-XRD. Mg^{2+} ions were modelled as $Mg(H_2O)_6^{2+}$ complexes based on observed electron densities and ICP-MS data. They are located in one of two types of windows connecting the cavities, surrounded by six ligands (**Figure 2-11a,b**). This position may be preferred by the ions as they are expected to interact with organic ligands through the extended hydrogen-bonding network formed by water molecules (**Figure 2-11c**). Each of these positions, held by magnesium ions at half occupancy, is expected to serve as a potential hopping site during ion transport. The potassium ions in **1-K** are disordered in the cavities and were thus not included in the respective structural model.

As alluded to before, PXRD indicated structural differences between **1-K** and **2-Mg** that coincide with the respective activation energies: The lower symmetry materials **2-Mg** and **2-**

Zn showed higher activation energies than the higher symmetry MOFs **1-Li**, **1-Na**, **1-K** and **1-Sr**. We hypothesize that the hard Mg^{2+} ions can interact more strongly with the framework than softer potassium ions, based on the single crystal structures. The interaction of Mg^{2+} ions with water molecules increases their acidity, resulting in stronger hydrogen-bonding with the framework, holding Mg^{2+} ions at their preferred crystallographic position. We expect the same to be true for hard Zn^{2+} ions. Because Li^{+}, Na^{+}, K^{+} and Sr^{2+} ions are softer, the coordinated water molecules are less acidic, leading to weaker hydrogen bonding interactions with the framework. This finally results in lower activation energies for **1-Li**, **1-Na**, **1-K,** and **1-Sr** compared to **2-Mg** and **2-Zn**.

The activation energy measured for **1-Sr** is, however, still significantly lower than for **1-Li**, **1-Na** and **1-K**. This may be explained by the difference in the number of charge carriers for monovalent and divalent ions in this system, since the total number of cations cannot exceed what is expected based on balancing the charge of the anionic framework. Based on the crystal structure of **2-Mg**, divalent cations occupy their preferred positions in half occupancy – or half of the positions. This means that for **1-Sr**, almost half of these hopping sites are unoccupied. Traditionally used to describe ion conduction in dense solids, vacant sites can lower the defect formation energy, thus reducing the activation energy.[32] We believe that a similar principle may be at play for **1-Sr**, which features 39% vacant sites.

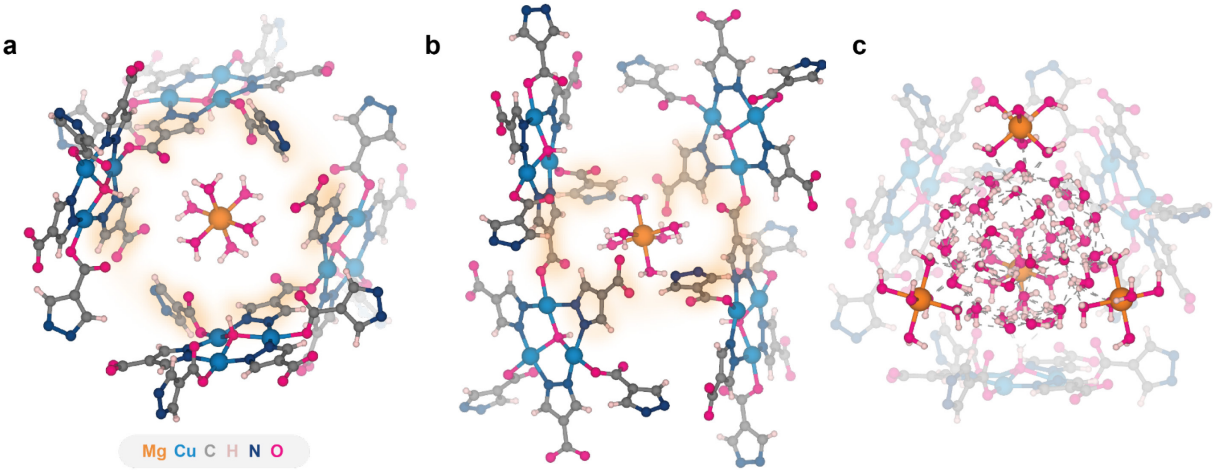

Figure 2-11. The hexaaqua-magnesium complex is located in the center of six organic ligands in **2-Mg**, shown from a a) top-down view and b) side view. The six organic ligands in immediate proximity to the Mg-complex are marked in yellow. c) The Mg^{2+} ions are part of an extended hydrogen-bonding network of water molecules that sit in the pores.

Characterization of Vacancy Effects

Introducing hopping site vacancies is a concept borrowed from traditional solid-state electrolytes,[32] that to our knowledge has not been applied to MOFs. To test whether vacant

hopping sites can indeed lower the activation energy for ion transport here, we introduced vacancies in Li- and K-exchanged frameworks by starting with **2-Mg** and soaking it with Li^+ or K^+ ions for 7 days. The resulting materials, **1-Li-v** and **1-K-v,** have sum formulas of $Li_{0.74}Mg_{0.13}[Cu_3(\mu_3\text{-}OH)(PyC)_3]$ and $K_{0.72}Mg_{0.14}[Cu_3(\mu_3\text{-}OH)(PyC)_3]$, respectively. The ratios of Cu to Mg, and to Li or K for each material were determined by ICP-MS (**Table 2-2**).

Table 2-2. ICP-MS data for **1-Li-v** and **1-K-v**. The molar ratios of SBU-Cu to respective alkali ion or to magnesium ions is given. The percentage of vacant SBUs is the difference between 1 and the total number of alkali and magnesium ions per SBU. The total charge per SBU refers to the combined charges of alkali and magnesium ions, with a theoretical value of 1.

Sample	Alkali ion (M^+)/Cu_3-SBU molar ratio	Mg/Cu_3-SBU molar ratio	Vacant SBUs	Measurement
1-Li-v	0.74 (Li^+)	0.13	13%	VT conductivity
1-K-v	0.72 (K^+)	0.14	14%	VT conductivity

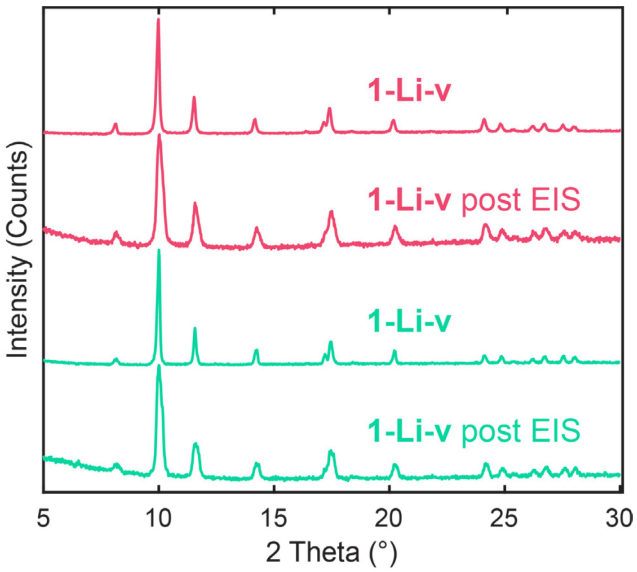

Figure 2-12. PXRD of **1-Li-v** and **1-K-v** pre and post EIS measurements.

The additional reflections in the PXRD for **2-Mg** disappear after ion exchange to **1-Li-v** and **1-K-v**, solidifying the notion that the identity of the mobile ion influences the structure and interaction with hopping sites (**Figure 2-12**). As the amount of magnesium ions must be equal to the amount of vacant sites, **1-Li-v** features 13% vacant hopping sites and **1-K-v** has 14% vacant sites relative to **1-Li** and **1-K**, respectively. Although Mg^{2+} ions are present in both materials, their contribution to activation energy and conductivity can be neglected due to their comparably small fraction and the two orders of magnitude lower Mg^{2+} ion conductivity.

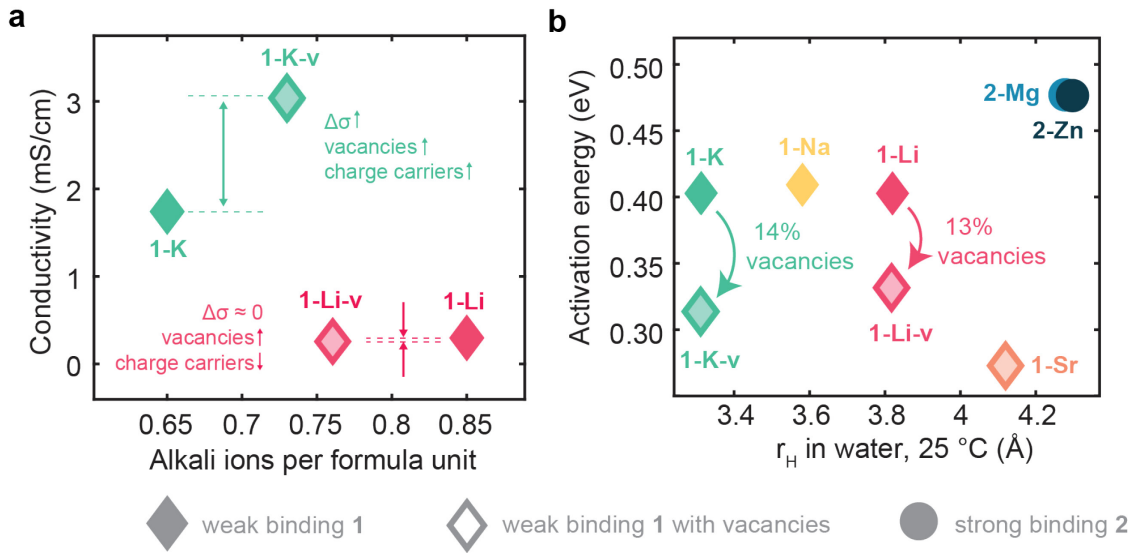

Figure 2-13. a) Activation energies of **1-Li**, **1-Na**, **1-K**, **1-Sr**, **2-Mg**, **2-Zn**, **1-Li-v** and **1-K-v** given against the hydrated radii of the respective ions in water.[23] b) Comparison of ionic conductivities of **1-Li** and **1-Li-v**, and **1-K** and **1-K-v**. c) Schematic representation of ion transport in solvated porous frameworks as a combination of two processes: **A** Interaction with hopping sites and **B** Solvent-assisted transport through pores.

The room temperature conductivities of **1-Li-v** and **1-K-v** are 2.8×10^{-4} S/cm and 3.0×10^{-3} S/cm, respectively (**Figure 2-13a**). For **1-Li-v**, this value is approximately the same compared to **1-Li** without vacant sites. This can be rationalized as the number of vacancies increased from **1-Li** to **1-Li-v**, leading to an increase in conductivity, while the number of charge carriers decreased (from 0.85 to 0.76 per formula unit) between these two samples, lowering the conductivity. In case of **1-K-v,** the ionic conductivity was found to be higher than that of **1-K** by 1.3×10^{-3} S/cm. Here, **1-K-v** has both a higher charge carrier concentration (0.73 vs 0.65 ions per formula unit) and a higher number of vacancies. Both factors are expected to contribute to the higher conductivity value found for **1-K-v**. Most significantly, these observations suggest that the effects of vacant hopping sites and charge carrier concentration on the ionic conductivity are both small compared to the variations in conductivity as a result of different ionic species and their hydrated ionic radii.

Importantly, the activation energy of **1-Li-v** at 0.34 eV is indeed significantly lowered in comparison to 0.40 eV for **1-Li**. A similar result was observed for **1-K-v** with an activation energy of 0.33 eV compared to 0.40 eV for **1-K** (**Figure 2-21**). This confirms our hypothesis that deliberate introduction of vacant hopping sites is a powerful approach towards lowering the activation energy for ion transport (**Figure 2-13b**).

Conclusion

The foregoing results allow us to deconvolute the effect of three variables on ion transport in MOFs. First, the nature of the metal ion plays an important role, as has been shown numerous times before and as attested here, too. Second, and much less obvious, our results suggest that the nature of the hopping site, can be influenced by the mobile ion itself: Mg^{2+} and Zn^{2+} cause structural distortions in the framework, which manifest in the activation energy for transport of these ions. Third, we show that aliovalent cation exchange can be used to control the level of hopping site vacancies, and that introducing such vacancies correlates with a reduction of the activation energy for transport. Based on these findings, we propose two subprocesses during ion transport: **A** *Ion interaction with hopping sites* and **B** *Solvent-assisted ion transport through pores* (**Figure 2-14**).

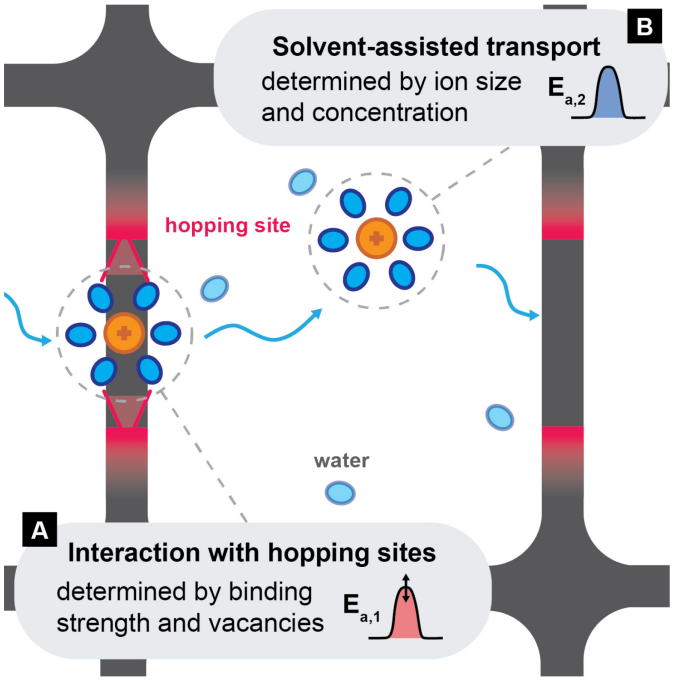

Figure 2-14. Schematic representation of ion transport in solvated porous frameworks as a combination of two processes: **A** *Interaction with hopping sites* and **B** *Solvent-assisted transport through pores.*

Process **A** contributes the bulk of the apparent (i.e. measured) activation energy and is the process that describes the interaction of mobile ions with the framework walls. This process is strongly influenced by hopping site vacancies and the strength of interaction with hopping sites, analogous to dense solids in which the activation energy is determined by contributions from vacancies, and from the energy barrier between two low energy states.[32] Process **B** describes the movement of solvated ions through a pore-confined water network before they reach the next hopping site, and can be thought of as similar to diffusion in liquids. Akin to liquid

electrolytes, solvent-assisted ion transport is governed by charge carrier concentration and hydrated ion size.[33] In line with this interpretation, the apparent activation energy in our system is unaffected by changes in charge carrier concentration or hydrated ion size. The overall conductivity, however, is affected by both the interaction of a given ion with the hopping sites, and by solvent-assisted diffusion.

2.4 Materials and Supplementary Information

2.4.1 Materials

Metal nitrates were purchased from Sigma-Aldrich, pyrazole-4-carboxylic acid was purchased from Synthonix. $Li_4Ti_5O_{12}$ (LTO) and Al foil were purchased from MTI.

2.4.2 Synthesis

MOF synthesis

According to previously described procedures,[19] copper(II) nitrate hexahydrate (0.966 g, 4.00 mol, 1 equiv.) and 4-pyrazolecarboxylic acid (0.448 g, 4.00 mol, 1 equiv.) were mixed in 12 mL ammonium hydroxide solution and 52 mL water and loosely capped. The solution was allowed to stand loosely capped at room temperature for 2 days to yield dark blue crystals.

Ion exchange

In a typical ion exchange experiment, 1 g of MOF crystallites were soaked in 100 mL of aqueous 1M metal nitrate solution at 45°C for 10 days. The powder was washed with deionized water several times and soaked in fresh water over night before isolating via filtration and washing with more water.

2.4.3 Characterization Methods

Electrochemical characterization

Characterization of the electrolyte was performed on a 2-electrode cell with stainless steel current collectors. The electrolyte powder was hydrated in a small amount of water at least overnight and ground in an agate mortar. The powder was then pressed in a PTFE die with 1 cm diameter at 1 ton for 30 seconds. Electrochemical measurements were performed using a Bio-Logic VSP potentiostat.

The alternating current (AC) impedance analysis was performed on 2-electrode cell with an input voltage amplitude of 100 mV. The pellet was maintained at the target temperature by an Espec BTL-433 chamber. Data was recorded every 5 °C between 25 °C and 50 °C (**1-Na**, **1-K**, **2-Zn**, **2-Mg, 1-Sr**) and held for 2 h each to reach thermal equilibrium or every 2 °C between

25 °C and 35 °C (**1-Li, 1-Li-v, 1-K-v**) and held for 1 h each to reach thermal equilibrium. The resistance was obtained by fitting the Nyquist plot to the model circuit shown in **Figure 2-18**, using the EC-Lab software.

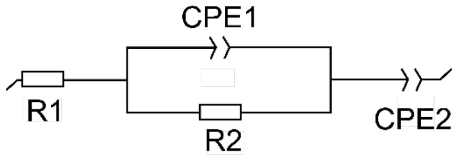

Figure 2-15. Equivalent circuit for fitting EIS for SS||electrolyte||SS cells.

The ionic conductivity was calculated using equation

$$\sigma = \frac{1}{R_2}\frac{t}{A} \tag{3}$$

where R_2 is the resistance, t is the pellet thickness and A is the area.

Transference numbers

Partially reduced LTO (R-LTO) was used as non-blocking electrode in symmetric cells for transference number measurements. R-LTO was prepared according to previously described procedures.[30] Naphthalene (6 mmol) and lithium metal (6 mmol) were stirred in 30 mL tetrahydrofuran under argon atmosphere for 6 h before 3 mmol LTO were added and stirred for 1 h. The blue-grey powder was isolated via filtration.

Cells were assembled by pressing 30 mg of solid electrolyte in a PTFE die with 1 cm diameter at 1 ton for 30 seconds. Electrodes were composed of a mixture of R-LTO/electrolyte/acetylene black (4/5/1 w/w/w) and directly pressed onto the electrolyte. Aluminum foil was used as the current collector.

Impedance measurements on the symmetric cells were conducted as described before. The resistance was obtained by fitting the Nyquist plot to the model circuit shown in **Figure 2-19** using the EC-Lab software.

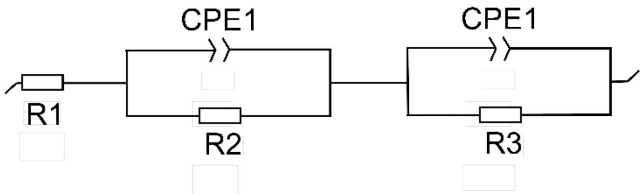

Figure 2-16. Equivalent circuit for fitting EIS for determining transference numbers.

Chronoamperometry was performed by applying a 10 mV bias voltage and held until a steady state current was observed.

Inductively coupled plasma mass spectrometry (ICP-MS)

Inductively coupled plasma mass spectrometry analyses were conducted on an Agilent 7900 at the MIT Center for Environmental Health Sciences (MIT CEHS). Ion loadings after exchange were calculated with reference to copper from framework SBU.

Single crystal X-ray diffraction (SC-XRD)

Diffraction data was collected on a XtaLAB, Dualflex, Pilatus 300K with Mo Kα radiation (λ = 0.71073 Å) from a PhotonJet source. The crystals were kept at 100 K during data collection. Details of the data quality and refinement statistics are provided in **Table S2**.

Powder X-ray diffraction (PXRD)

PXRD patterns were recorded with a Bruker D8 Advance diffractometer equipped with a Göbel mirror, rotating sample stage, LynxEye detector and Cu Kα (λ = 1.5406 Å) X-ray source in a θ = 2θ Bragg–Brentano geometry. An anti-scattering slit (1 mm) and an exchangeable detector slit (8 mm) were used. The tube voltage and current were 40 kV and 40 mA, respectively. Knife-edge attachments were used to remove scattering at low angles. Samples for PXRD were prepared by placing powders on a zero-background silicon (510) crystal plate. Pawley refinements were performed experimental data using pseudo-Voigt functions in TOPAS.

Table 2-3. Background-subtracted fit-statistics for Pawley refinements.

Structure	Cell parameter (Å)	R_p	R_{wp}	GoF
1-Li	30.30	7.00%	9.93%	2.42
1-Na	30.30	5.29%	6.94%	1.31
1-K	30.10	4.47%	5.75%	1.32
1-Sr	30.31	4.64%	6.08%	1.22
2-Zn	30.19	5.48%	7.24%	1.50
2-Mg	30.14	5.50%	7.22%	1.40

2.4.4 Single Crystal X-ray Diffraction

Table 2-4. Crystal data and structure refinement for **1-K**.

CCDC deposition number	**2420526**
Empirical formula	C12 H22 Cu3 N6 O14.50
Formula weight	672.96
Temperature/K	100
Crystal system	Cubic
Space Group	$Fd\bar{3}$ (203)
a/Å	30.0110(4)
b/Å	30.0110(4)
c/Å	30.0110(4)
α/°	90
β/°	90
γ/°	90
Volume/Å^3	27029.7(12)
Z	32
ρ_{calc}/g/cm^3	1.323
μ/mm^{-1}	1.927
F(000)	10848
Crystal size/mm^3	0.12 x 0.12 x 0.03
Radiation	MoKα (λ=0.71073)
2θ range for data collection/°	5.944 to 52.594
Index ranges	−37≤h≤37, −37≤k≤37, −37≤l≤37
Reflections collected	169720
Independent reflections	2076 [R_{int} = 0.0743]
Data/restraints/parameters	2076/95/116
GoF on F^2	1.172
Final R indexes [I≥2σ (I)]	R_1 = 0.0481, wR_2 = 0.1105
Final R indexes [all data]	R_1 = 0.0691, wR_2 = 0.1268
Largest diff. peak/hole / e Å^{-3}	0.762/ −0.620

The crystallographic information file is available from the Cambridge Crystallographic Data Centre under accession code CCDC 2420526.

Table 2-5. Crystal data and structure refinement for **2-Mg**.

CCDC deposition number	**2407432**
Empirical formula	C4 H9.59 Cu Mg0.07 N2 O5.52
Formula weight	239.18
Temperature/K	100
Crystal system	Cubic
Space Group	$Fd\bar{3}$ (203)
a/Å	30.32659(18)
b/Å	30.32659(18)
c/Å	30.32659(18)
α/°	90
β/°	90
γ/°	90
Volume/Å^3	27891.4(5)
Z	96
ρ_{calc}/g/cm^3	1.367
μ/mm^{-1}	1.880
F(000)	11667
Crystal size/mm^3	0.4 x 0.4 x 0.3
Radiation	MoKα (λ=0.71073)
2θ range for data collection/°	5.8760 to 60.7000
Index ranges	−36≤h≤36, −36≤k≤36, −36≤l≤36
Reflections collected	81255
Independent reflections	2144 [R_{int} = 0.0421]
Data/restraints/parameters	2144/131/177
GoF on F^2	1.118
Final R indexes [I≥2σ (I)]	R_1 = 0.0971, wR_2 = 0.2588
Final R indexes [all data]	R_1 = 0.0971, wR_2 = 0.2588
Largest diff. peak/hole / e Å^{-3}	0.892/ −1.472

The crystallographic information file is available from the Cambridge Crystallographic Data Centre under accession code CCDC 2407432.

2.4.5 Supplementary Data

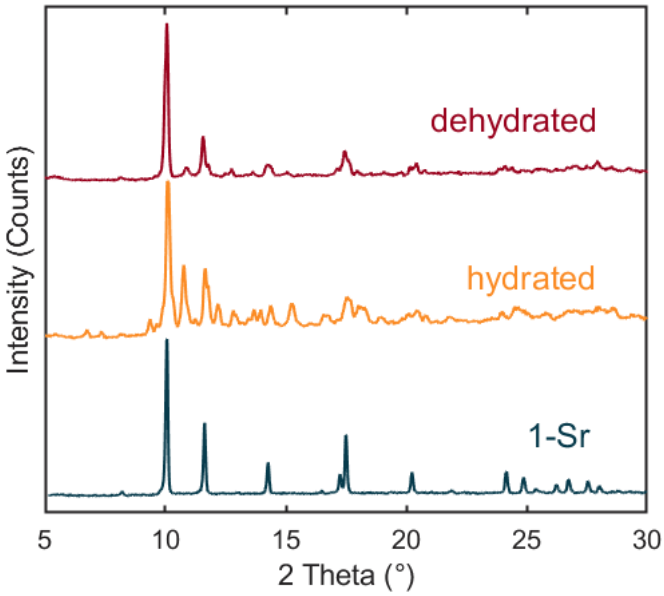

Figure 2-17. PXRD of **1-Sr** (bottom) in comparison to an over-exchanged sample containing strontium. The top trace shows the PXRD of an over-exchanged sample after 1 month in low humidity ambient conditions, the middle trace shows the same sample after soaking in water over night.

Calcium exchanged samples yielded purple solids with unknown structure after as little as 1 day of exchange. Similar to **2-Zn**, strontium exchange can yield strontium contents higher than 0.5 strontium atoms per SBU. This is accompanied by a reduction in crystallinity and formation of small amounts of an unknown phase, which is amplified upon hydrating the material by soaking it in water. **1-Sr**, used for electrochemical characterization, was thus carefully prepared to have strontium contents below 0.5 atoms per SBU such that no impurity phases were formed, and the framework remained structurally unchanged upon hydration.

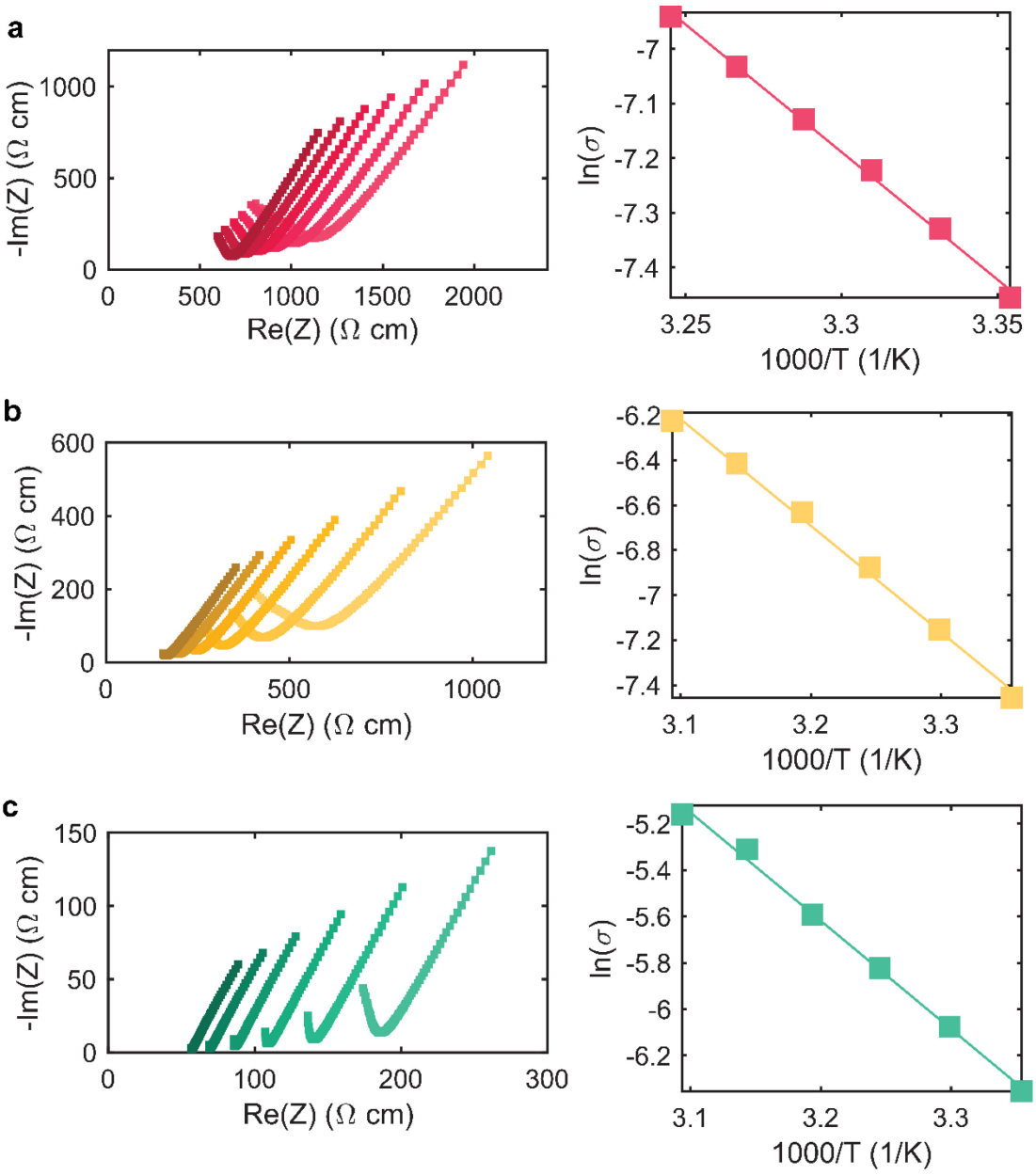

Figure 2-18. Impedance spectra and linear fit of resistances of a) **1-Li** at temperature between 25 °C and 35°C and b) **1-Na**, c) **1-K** at temperatures between 25 °Cand 55 °C. Darker colors indicate higher temperatures. Data is normalized for each pellet thickness.

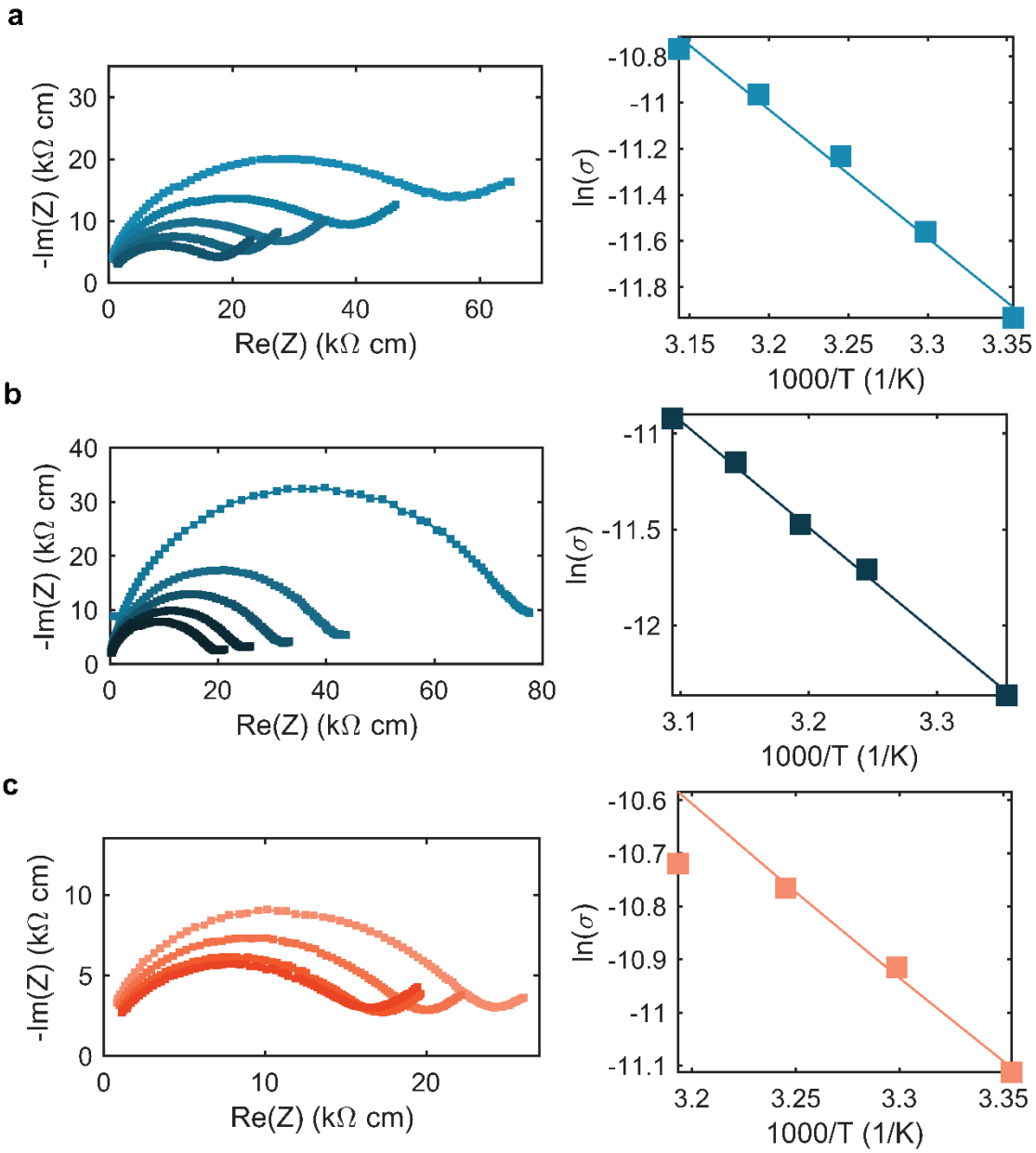

Figure 2-19. Impedance spectra and linear fit of resistances of a) **2-Mg**, b) **2-Zn** and c) **1-Sr**. Darker colors indicate higher temperatures. Data is normalized for each pellet thickness.

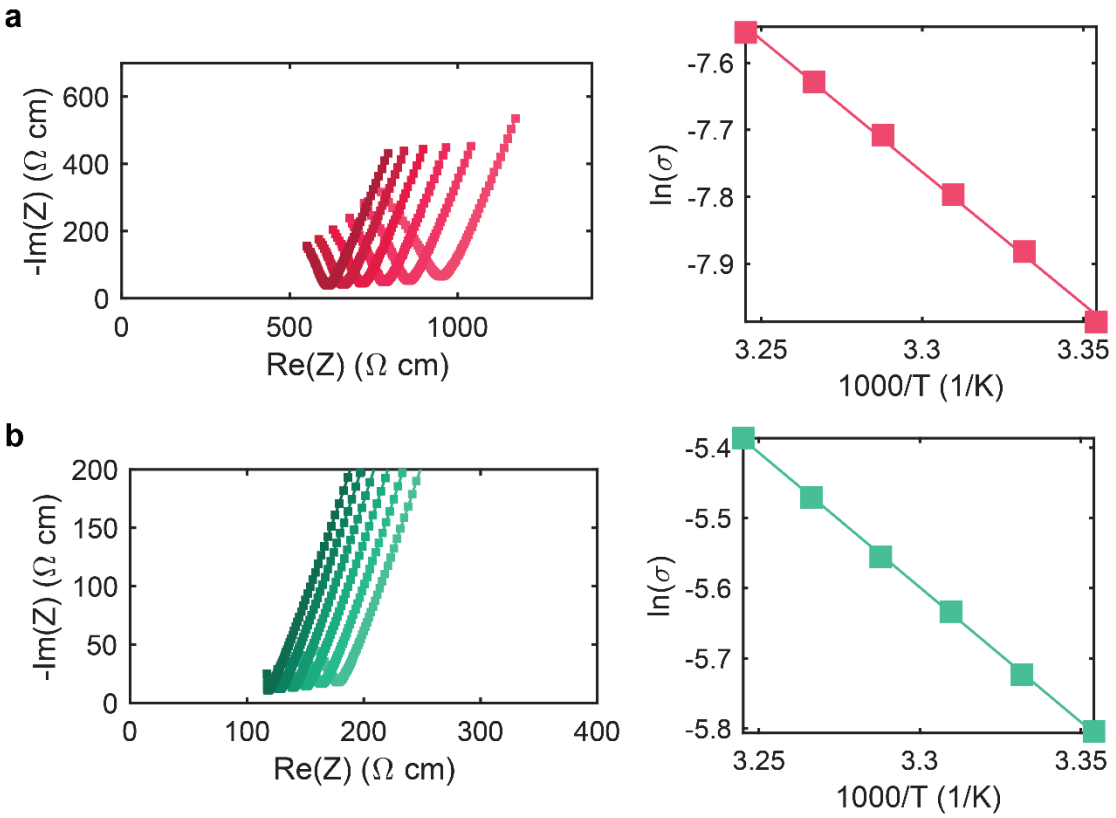

Figure 2-20. Impedance spectra and linear fit of resistances of a) **1-Li-v** and b) **1-K-v** at temperatures between 25 °C and 35 °C. Darker colors indicate higher temperatures. Data is normalized for each pellet thickness.

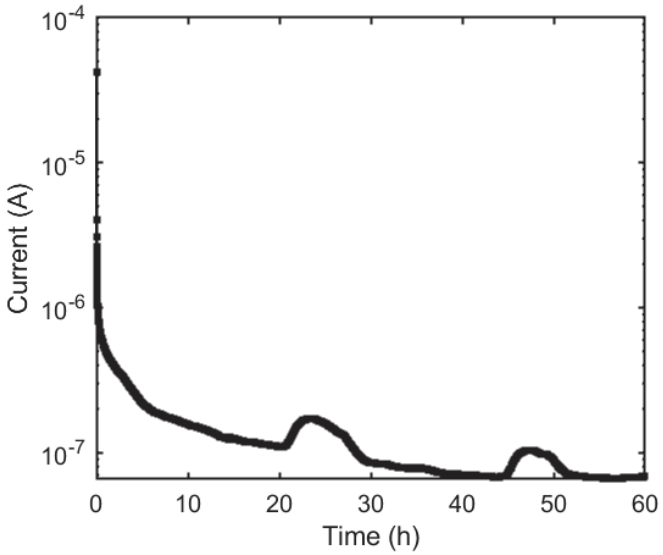

Figure 2-21. Chronoamperometric measurement of **1-NH4**, polarized at 1V over 60 h.

The electronically insulating nature of the framework was verified by the parent compound **1-NH4**, reaching an electrical conductivity of 1.3×10^{-9} S/cm, as determined by chronoamperometry:

2.5 References

(1) Biemolt, J.; Jungbacker, P.; van Teijlingen, T.; Yan, N.; Rothenberg, G. Beyond Lithium-Based Batteries. *Materials* **2020**, *13* (2), 425.

(2) Rinkel, B. L. D.; Hall, D. S.; Temprano, I.; Grey, C. P. Electrolyte Oxidation Pathways in Lithium-Ion Batteries. *J. Am. Chem. Soc.* **2020**, *142* (35), 15058–15074.

(3) Wang, Q.; Jiang, L.; Yu, Y.; Sun, J. Progress of Enhancing the Safety of Lithium Ion Battery from the Electrolyte Aspect. *Nano Energy* **2019**, *55*, 93–114.

(4) Ravdel, B.; Abraham, K. M.; Gitzendanner, R.; DiCarlo, J.; Lucht, B.; Campion, C. Thermal Stability of Lithium-Ion Battery Electrolytes. *J. Power Sources* **2003**, *119–121*, 805–810.

(5) Li, W.; Dahn, J. R.; Wainwright, D. S. Rechargeable Lithium Batteries with Aqueous Electrolyte. *Science* **1994**, *264*, 1115–1118.

(6) Takada, K. Progress in Solid Electrolytes toward Realizing Solid-State Lithium Batteries. *J. Power Sources* **2018**, *394*, 74–85.

(7) Shen, L.; Bin Wu, H.; Liu, F.; Brosmer, J. L.; Shen, G.; Wang, X.; Zink, J. I.; Xiao, Q.; Cai, M.; Wang, G.; Lu, Y.; Dunn, B.; Shen, L.; Wu, H. B.; Liu, F.; Shen, G.; Wang, X.; Lu, Y.; Brosmer, J. L.; Zink, J. I.; Xiao, Q.; Cai, M.; Wang, G.; Dunn, B. Creating Lithium-Ion Electrolytes with Biomimetic Ionic Channels in Metal–Organic Frameworks. *Adv. Mater.* **2018**, *30* (23), 1707476.

(8) Miner, E. M.; Park, S. S.; Dincă, M. High Li^+ and Mg^{2+} Conductivity in a Cu-Azolate Metal-Organic Framework. *J. Am. Chem. Soc.* **2019**, *141* (10), 4422–4427.

(9) Yoshida, Y.; Yamada, T.; Jing, Y.; Toyao, T.; Shimizu, K.; Sadakiyo, M. Super Mg^{2+} Conductivity around 10^{-3} S cm^{-1} Observed in a Porous Metal–Organic Framework. *J. Am. Chem. Soc.* **2022**, *144* (19), 8669–8675.

(10) Pan, Y.; Saha, S.; Burigana, M.; Singh, V.; Yaghi, O. M.; Paesani, F. Thermodynamics of Alkali Metal Ion Uptake from Aqueous Solution in MOF-808. *Chem. Sci.* **2025**, *16* (26), 12129–12138.

(11) Xia, Q.; Ma, X.; Qiu, P.; Yuan, G.; Chen, X. Anionic Metal-Organic Framework as an Ultrafast Single-Ion Conductor for Exceptional Performance Rechargeable Zinc Batteries. *J. Am. Chem. Soc.* **2025**, *147*, 23331–23338.

(12) Park, S. S.; Tulchinsky, Y.; Dinca, M. Single-Ion Li^+, Na^+, and Mg^{2+} Solid Electrolytes Supported by a Mesoporous Anionic Cu-Azolate Metal-Organic Framework. *J. Am. Chem. Soc.* **2017**, *139* (38), 13260–13263.

(13) Aubrey, M. L.; Ameloot, R.; Wiers, B. M.; Long, J. R. Metal-Organic Frameworks as Solid Magnesium Electrolytes. *Energy Environ. Sci.* **2014**, *7* (2), 667–671.

(14) Ameloot, R.; Aubrey, M.; Wiers, B. M.; Gõmora-Figueroa, A. P.; Patel, S. N.; Balsara, N. P.; Long, J. R. Ionic Conductivity in the Metal-Organic Framework UiO-66 by Dehydration and Insertion of Lithium Tert-Butoxide. *Chem. A Eur. J.* **2013**, *19* (18), 5533–5536.

(15) Duan, X.; Ouyang, Y.; Zeng, Q.; Ma, S.; Kong, Z.; Chen, A.; He, Z.; Yang, T.; Zhang, Q. Two Carboxyl-Decorated Anionic Metal-Organic Frameworks as Solid-State

Electrolytes Exhibiting High Li^+ and Zn^{2+} Conductivity. *Inorg. Chem.* **2021**, *60* (15), 11032–11037.

(16) Zettl, R.; Lunghammer, S.; Gadermaier, B.; Boulaoued, A.; Johansson, P.; Wilkening, H. M. R.; Hanzu, I. High Li^+ and Na^+ Conductivity in New Hybrid Solid Electrolytes Based on the Porous MIL-121 Metal Organic Framework. *Adv. Energy Mater.* **2021**, *11* (16), 2003542.

(17) Tian, L.; Xu, X.; Liu, M.; Liu, Z.; Liu, Z. Significantly Enhancing the Lithium Ionic Conductivity of Metal-Organic Frameworks via a Postsynthetic Modification Strategy. *Langmuir* **2021**, *37* (13), 3922–3928.

(18) Iliescu, A.; Andrews, J. L.; Oppenheim, J. J.; Dincă, M. A Solid Zn-Ion Conductor from an All-Zinc Metal-Organic Framework Replete with Mobile Zn^{2+} Cations. *J. Am. Chem. Soc.* **2023**, *145* (48), 25962–25965.

(19) Quartapelle Procopio, E.; Linares, F.; Montoro, C.; Colombo, V.; Maspero, A.; Barea, E.; Navarro, J. A. R. Cation-Exchange Porosity Tuning in Anionic Metal-Organic Frameworks for the Selective Separation of Gases and Vapors and for Catalysis. *Angew. Chem. Intl. Ed.* **2010**, *122* (40), 7466–7469.

(20) Shen, L.; Wu, H. Bin; Liu, F.; Brosmer, J. L.; Shen, G.; Wang, X.; Zink, J. I.; Xiao, Q.; Cai, M.; Wang, G.; Lu, Y.; Dunn, B. Creating Lithium-Ion Electrolytes with Biomimetic Ionic Channels in Metal–Organic Frameworks. *Adv. Mater.* **2018**, *30* (23), 1707476.

(21) Zhu, F.; Bao, H.; Wu, X.; Tao, Y.; Qin, C.; Su, Z.; Kang, Z. High-Performance Metal-Organic Framework-Based Single Ion Conducting Solid-State Electrolytes for Low-Temperature Lithium Metal Batteries. *ACS Appl. Mater. Interfaces* **2019**, *11* (46), 43206–43213.

(22) Yang, H.; Liu, B.; Bright, J.; Kasani, S.; Yang, J.; Zhang, X.; Wu, N. A Single-Ion Conducting UiO-66 Metal-Organic Framework Electrolyte for All-Solid-State Lithium Batteries. *ACS Appl. Energy Mater.* **2020**, *3* (4), 4007–4013.

(23) Nightingale Jr., E. R. Phenomenological Theory of Ion Solvation. Effective Radii of Hydrated Ions. *J. Phys. Chem.* **1959**, *63* (9), 1381–1387.

(24) Gu, Y. J.; Lo, Y. A.; Li, A. C.; Chen, Y. C.; Li, J. H.; Wang, Y. Sen; Tian, H. K.; Kaveevivitchai, W.; Kung, C. W. A Single Potassium-Ion Conducting Metal-Organic Framework. *ACS Appl. Energy Mater.* **2022**, *5* (7), 8573–8580.

(25) Cao, K.; Ma, J.; Yue, Z.; Li, H.; Fan, Y.; Liu, H. Status and Challenges of Solid-State Electrolytes for Potassium Batteries. *Small* **2025**, 2500762.

(26) Cepeda, J.; Pérez-Yáñez, S.; Beobide, G.; Castillo, O.; Goikolea, E.; Aguesse, F.; Garrido, L.; Luque, A.; Wright, P. A. Scandium/Alkaline Metal-Organic Frameworks: Adsorptive Properties and Ionic Conductivity. *Chem. Mater.* **2016**, *28* (8), 2519–2528.

(27) Zhang, Y.; Wang, J.; Apostol, P.; Rambabu, D.; Eddine Lakraychi, A.; Guo, X.; Zhang, X.; Lin, X.; Pal, S.; Rao Bakuru, V.; Chen, X.; Vlad, A. Bimetallic Anionic Organic Frameworks with Solid-State Cation Conduction for Charge Storage Applications. *Angew. Chem. Intl. Ed.* **2023**, *62* (42), e202310033.

(28) Koneshan, S.; Rasaiah, J. C.; Lynden-Bell, R. M.; Lee, S. H. Solvent Structure, Dynamics, and Ion Mobility in Aqueous Solutions at 25 °C. *J. Phys. Chem. B* **1998**, *102*, 4193–4204.

(29) Zhang, Z.; Han, Q.; Zhang, S.; Guo, X.; Huang, H.; Yang, F.; Zhong, C. Abundant Hydrophilic Atoms Enhanced the Proton Conductivity of a Stable Metal-Organic Framework in a Wide Relative Humidity Range. *ACS Sustain. Chem. Eng.* **2022**, *10* (36), 11867–11874.

(30) Tabuchi, T.; Yasuda, H.; Yamachi, M. Mechanism of Li-Doping into $Li_4Ti_5O_{12}$ Negative Active Material for Li-Ion Cells by New Chemical Method. *J. Power Sources* **2006**, *162* (2), 813–817.

(31) Bruce, P. G.; Vincent, C. A. Steady State Current Flow in Solid Binary Electrolyte Cells. *J. Electroanal. Chem.* **1987**, *225*, 1–17.

(32) Bachman, J. C.; Muy, S.; Grimaud, A.; Chang, H. H.; Pour, N.; Lux, S. F.; Paschos, O.; Maglia, F.; Lupart, S.; Lamp, P.; Giordano, L.; Shao-Horn, Y. Inorganic Solid-State Electrolytes for Lithium Batteries: Mechanisms and Properties Governing Ion Conduction. *Chem. Rev.* **2016**, *116* (1), 140–162.

(33) Mahiuddin, S.; Ismail, K. Study of the Concentration Dependence of the Conductance of Aqueous Electrolytes. *J. Phys. Chem.* **1984**, *88* (5), 1027–1031.

Chapter Specific Acknowledgement

Single crystal diffraction measurements and structure solutions were carried out by Dr. Stefano Canossa with help from Dr. Julius J. Oppenheim. I would also like to acknowledge the invaluable input from Dr. Stefano Canossa for the interpretation of the structures and thank Zhentao Yang for his assistance with cell assembly and many helpful discussions. This work was supported by the Brown Science Foundation through the Brown Investigator Award to Mircea Dincă.

Chapter 3

Dual Proton-Electron Conduction in 2D Azaborine Metal-organic Frameworks

3.1 Abstract

Dual proton-electron conductors are highly sought after for applications in electronics and energy storage. Whereas two-dimensional metal-organic frameworks (2D MOFs) with high electrical conductivity are now numerous, introducing conduits for ion transport in these is challenging. Herein, we report the synthesis of two new mixed electron-proton conductors, M_3TABC_2 (M = Cu, Zn; TABC = hexahydroxy-1,5,9-triaza-2,6,10-trihydroxyboracoronene), made from a new conjugated azaborine ligand with mobile protons. Cu_3TABC_2 and Zn_3TABC_2 show high electronic conductivities of 6.0×10^{-2} S/cm and as 2.2×10^{-4} S/cm and ionic conductivities of $1.6 \pm 0.1 \times 10^{-5}$ S/cm and $1.9 \pm 0.4 \times 10^{-5}$ S/cm, respectively. Overall, this work demonstrates the incorporation of mobile protons into aromatic ligands as a strategy for enabling mixed conductivity in 2D MOFs.

3.2 Introduction

Materials that can conduct ionic and electronic charges simultaneously are desirable for applications in energy storage, neuromorphics, and bioelectronics.[1–3] Traditionally, mixed conductors are inorganic or polymer-based materials. Yet, metal-organic frameworks (MOFs) show great promise as such materials due to their tunable structures.[4–6] Despite the discovery of many MOFs that exhibit excellent electron or proton conductivity, the development of materials that combine both properties in a single material is in its infancy.[7–10] To effectively amalgamate the two conduction pathways in a single MOF, previous knowledge on enabling each conduction pathway has to be considered and implemented.

In terms of electronic conductivity, 2D MOFs contain large aromatic ligands that facilitate efficient band-like conduction through in-plane conjugation and ligand π-π interactions.[9] Proton conduction, rather common in electronically insulating MOFs, is typically enabled by appending functional groups that provide proton hopping sites, such as carboxylic acid, sulfonic acid, or hydroxyl groups.[10] Implementing proton conduction pathways in 2D conductive MOFs would produce materials that retain their high electronic conductivity while conducting protons in parallel, but examples of 2D mixed-conductive MOFs have been exceedingly rare.[4]

Inspired by recent advances in introducing heterocyclic ligands in 2D conductive MOFs, we reasoned we could target particular heterocyclic cores that also allowed the installation of acidic groups. These would potentially serve as hopping sites for proton transport on an underlying electrically conductive platform.[11–13] In this sense, we found the chemistry of conjugated azaborines featuring B–OH moieties particularly relevant.[14] Here, we show that this functional motif allows the formation of canonical tri-catechol hexagonal 2D MOFs that combine high electrical conductivity with proton transport.[15,16]

3.3 Results and Discussion

Synthesis and Structural Characterization

The new ligand hexahydroxy-1,5,9-triaza-2,6,10-trimethoxyboracoronene (TABC-OMe) is synthesized by borylation of triphenylene-hexamethoxy-1,5,9-triamine with BBr_3 at high temperature, adapted from established methods for the synthesis of azaborines from boron halides.[14,17] BBr_3 also functions as a demethylation agent yielding the deprotected catechols in one pot. Exchange of Br with OMe in methanol affords TABC-OMe, which is transformed into TABC-OH during MOF synthesis (**Figure 3-1**). Notably, the azaboracoronene core is isoelectronic to its all-carbon equivalent, coronene, but the LUMO energy levels of the former are raised compared to the latter (**Figure 3-2**).[13]

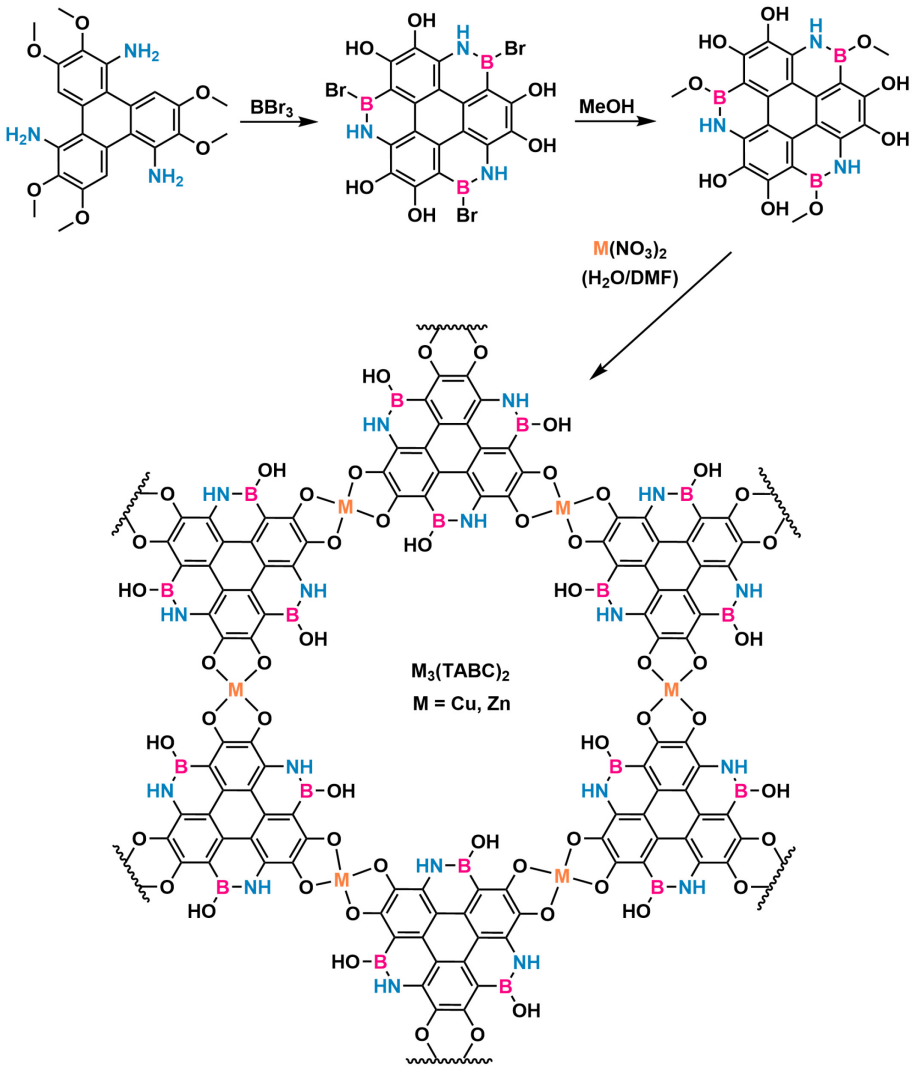

Figure 3-1. Schematic borylation of triphenylene-hexamethoxy-1,5,9-triamine, substitution to hexahydroxy-1,5,9-triaza-2,6,10-trimethoxyboracoronene (TABC-OMe), and formation of M_3TABC_2 (M = Cu, Zn) 2D MOFs.

The reaction of TABC-OMe with copper or zinc ions in mixtures of *N,N*-dimethylformamide (DMF) and water yields M_3TABC_2 (M = Cu, Zn) as black polycrystalline solids (**Figure 3-1**). Both Cu_3TABC_2 and Zn_3TABC_2 form needles of approximately 1-2 µm in length, as seen in scanning electron microscopy (SEM) images (**Figure 3-3**). Powder X-ray diffraction (PXRD) of both materials confirms their crystallinity and analogous structures (**Figure 3-4a**). Pawley refinements of the PXRD data provides best fits in hexagonal unit cells with lattice parameters of $a = b =$ 21.03(2) Å and $c =$ 3.239(5) Å for Cu_3TABC_2, and $a = b =$ 21.11(4) Å and $c =$ 3.155(5) Å for Zn_3TABC_2 (**Table 3-1**). Although the exact structure and stacking modes cannot be determined from PXRD data, Cu_3TABC_2 is likely present as van-der Waals stacked 2D sheets. Zn_3TABC_2 may similarly be understood as comprising van-der Waals stacked sheets. However, a structure in which zinc ions are not coplanar with the ligand sheets but adopt positions between layers accommodated by D_{4d} symmetry at the Zn atom cannot be ruled out. This would be equivalent to the recently reported structure of the related Zn_3HOTP_2 MOF.[18]

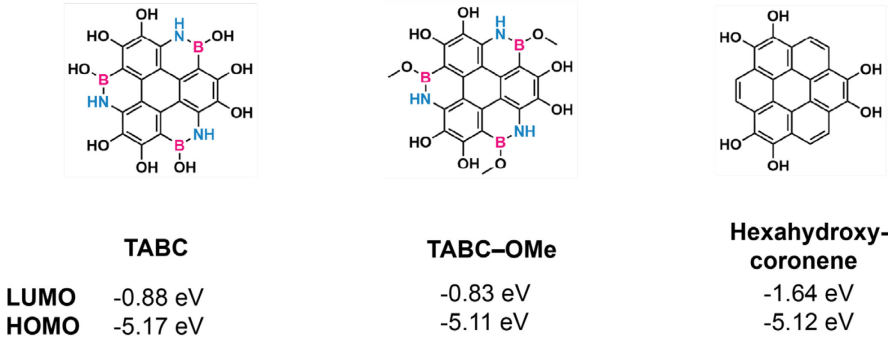

Figure 3-2. Calculated HOMO and LUMO energy levels of selected MOF ligand molecules (B3LYP/def2-TZVP).

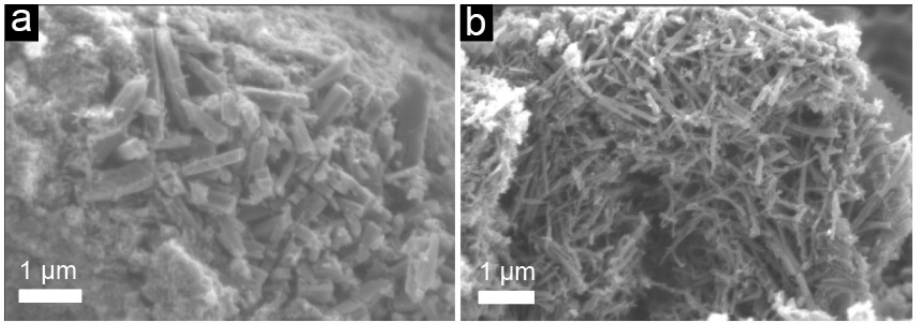

Figure 3-3. SEM images of a) Cu_3TABC_2 and b) Zn_3TABC_2.

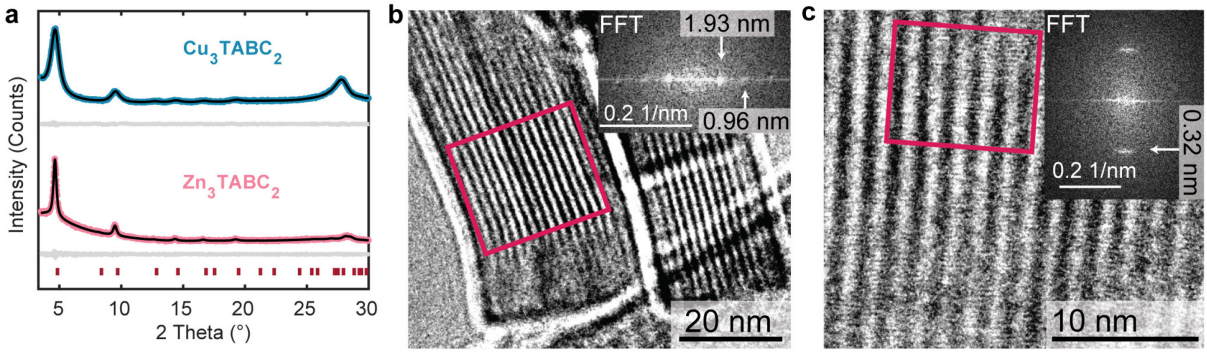

Figure 3-4. a) Pawley refinements (black traces) of experimental PXRD patterns of Cu_3TABC_2 and Zn_3TABC_2 (colored traces), grey traces show the difference plots, red marks show the theoretical reflection positions. HRTEM image of b) Cu_3TABC_2 and c) Zn_3TABC_2. The inset shows the fast Fourier transform of the area marked in red.

Confirmation of some of the structural details came from cryogenic high resolution transmission electron microscopy (cryo-HRTEM). The cryo-HRTEM images of Cu_3TABC_2 show contrast fringes parallel to the length of the crystalline needles (**Figure 3-4b**). Fast Fourier transform (FFT) reveals fringe periodicity of approximately 1.9 nm, in good agreement with the closest distance metal ions separated by two ligand molecules.[19] Similar contrast fringes are visible for Zn_3TABC_2 (**Figure 3-4c**). Additionally, fringes horizontal to the length of the crystals with a periodicity of approximately 0.32 nm correspond to the π-π stacking distance in crystallographic *c*-direction.

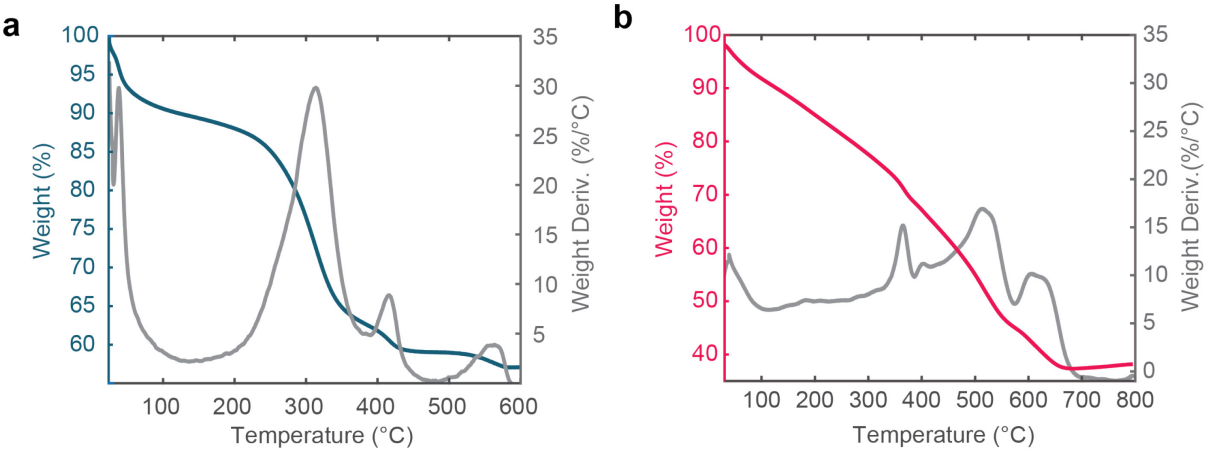

Figure 3-5. Thermogravimetric analysis of a) Cu_3TABC_2 and b) Zn_3TABC_2 under air flow and temperature ramp rate of 2°C/min.

Thermogravimetric analysis shows loss of solvent at 40 °C under air flow for both materials (**Figure 3-5**). Decomposition for Cu_3TABC_2 is observed above 200 °C. Zn_3TABC_2 shows continued gradual weight loss gradual upon heating. N_2 sorption isotherms at 77 K show that both materials are porous with BET apparent surface areas of 310 m^2/g for Cu_3TABC_2 and 118

m^2/g for Zn_3TABC_2 (**Figure 3-6**). These values are comparable to the nearly identical MOF made from triazacoronene.[13]

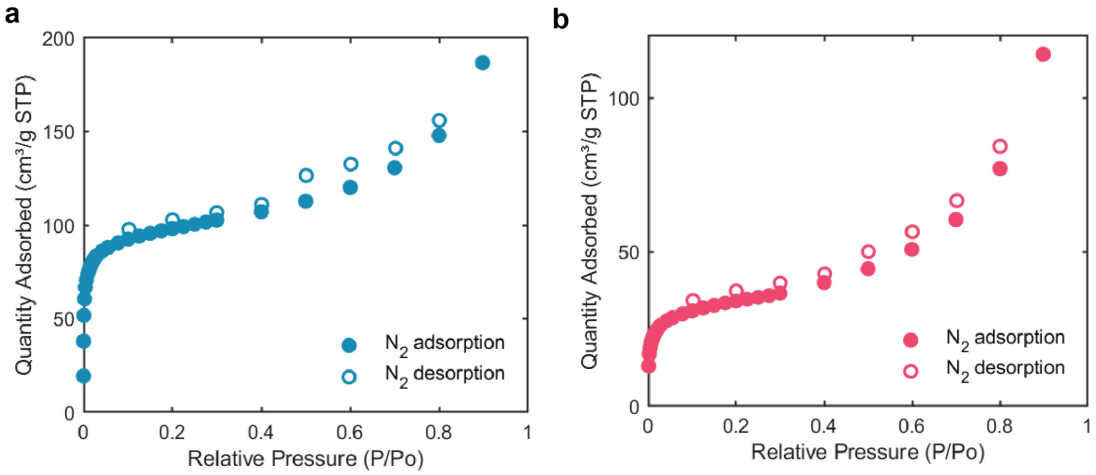

Figure 3-6. N_2 sorption isotherm for a) Cu_3TABC_2 and b) Zn_3TABC_2. The BET surface areas are 310 m^2/g and 118 m^2/g, respectively.

The X-ray photoelectron spectrum (XPS) of Cu_3TABC_2 shows the presence of two Cu $2p_{3/2}$ peaks at binding energies of 934.6 and 932.7 eV (**Figure 3-7**). This indicates mixed valency, commonly observed in Cu-based 2D conductive MOFs,[13,15,19] with a Cu^{2+}/Cu^{+} ratio of 3/2. The XPS spectrum of Zn_3TABC_2 shows the presence of only Zn^{2+} with a binding energy of 1021.8 eV. A small second component was found at 1023.6 eV, with a ratio of 1/9 compared to the main Zn^{2+} peak, which may be associated with structural distortions, defects, molecular Zn-species, or impurities.

Infrared spectroscopy (IR) was conducted to investigate the identity of the ligand after MOF formation. Previous reports have shown that the B–OR bond in aromatic azaborines is prone to hydrolysis in solvents with trace water.[14] As the synthesis of M_3TABC_2 is conducted in an aqueous mixture at 85 °C, substitution of the B–OMe moiety to B–OH is expected. IR spectra of the activated MOFs under inert atmosphere confirms the hydrolysis as no C–H stretching bands were visible and O–H stretching bands around 3200 cm^{-1} remain present even after activation under vacuum (**Figure 3-8**). Indeed, water vapor adsorption isotherms of Cu_3TABC_2 and Zn_3TABC_2 both show steep uptake at 8% relative humidity (RH), indicating hydrophilic pore environments (**Figure 3-9**).

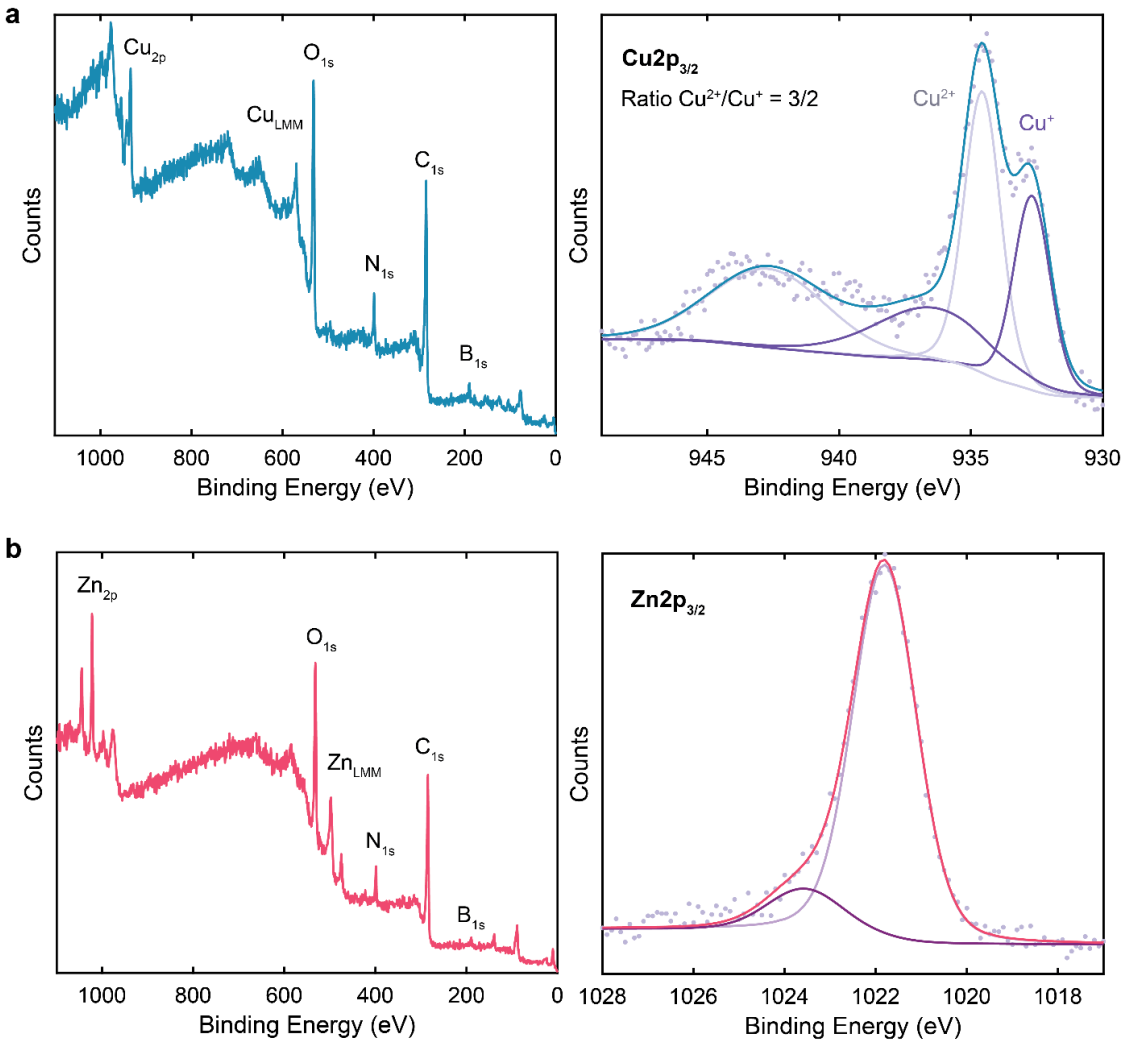

Figure 3-7. XPS spectra of a) Cu_3TABC_2 and b) Zn_3TABC_2. The full spectra are shown on the left, high resolution spectra of the $Cu2p_{3/2}$ or Zn $2p_{3/2}$ regions are shown on the right with corresponding peak fittings.

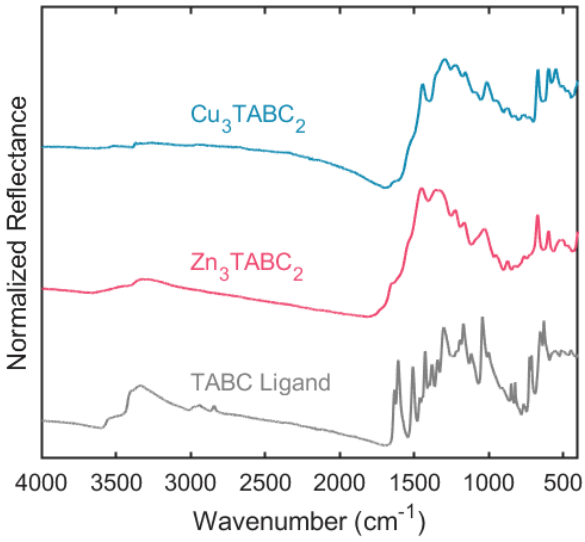

Figure 3-8. IR spectra of activated Cu_3TABC_2, Zn_3TABC_2, and TABC-OMe ligand.

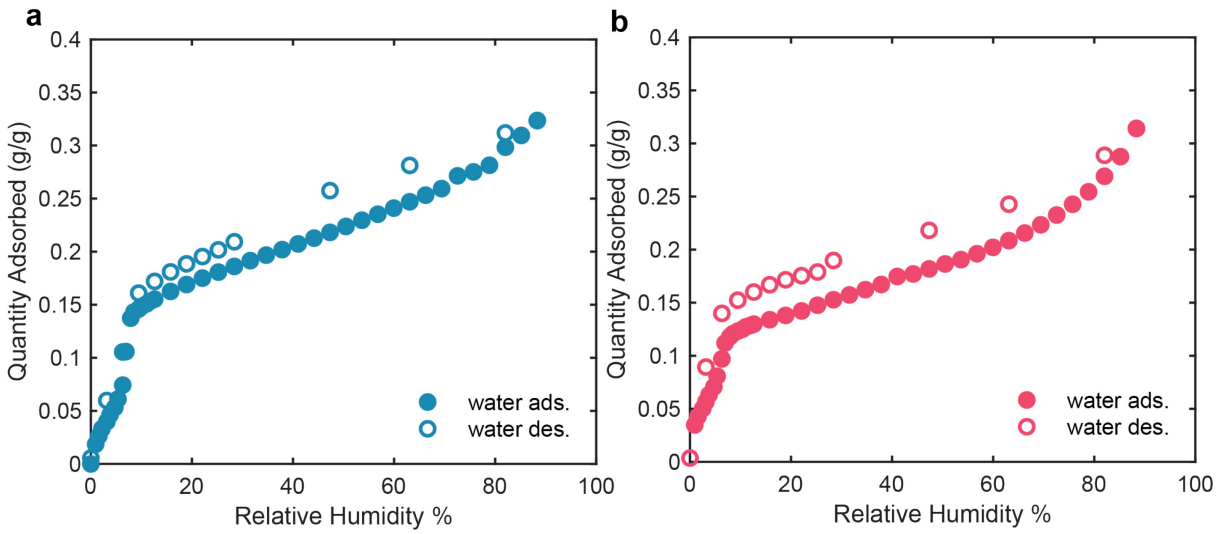

Figure 3-9. Water vapor adsorption and desorption isotherm of a) Cu_3TABC_2 and b) Zn_3TABC_2.

Electron Conductivity

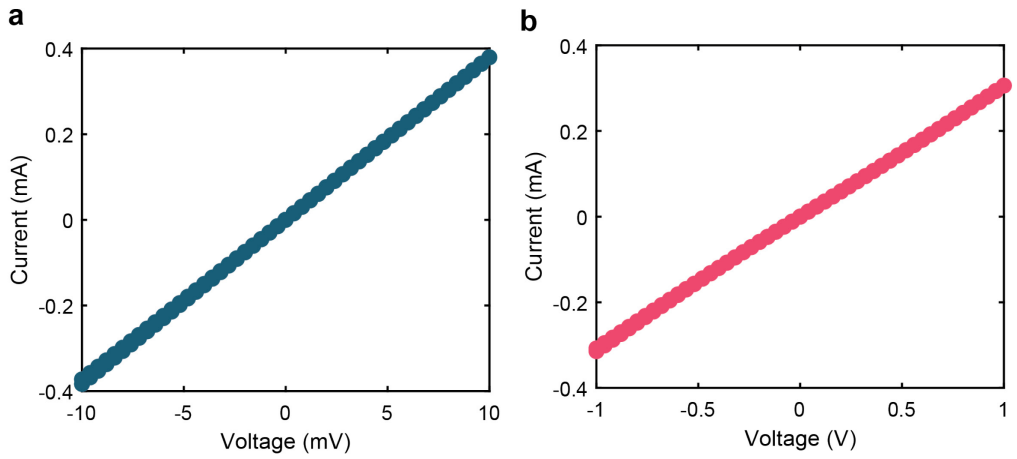

Figure 3-10. I-V curves of a representative sample of a) Cu_3TABC_2 and b) Zn_3TABC_2 in linear 2-probe geometry.

The electrical conductivity of Cu_3TABC_2 and Zn_3TABC_2 was measured on pressed pellets in linear 2-probe geometries. The DC conductivity of Cu_3TABC_2 was determined as 6.0×10^{-2} S/cm and as 2.2×10^{-4} S/cm for Zn_3TABC_2 (**Figure 3-10**). Optical bandgaps of 1.2 eV and 1.2 eV were obtained from Tauc plots of diffuse reflectance UV-Vis data (**Figure 3-11**). The mixed valency of copper ions in Cu_3TABC_2 may contribute to its superior electronic conductivity through increased charge delocalization.[20,21] However, the influence of minor structural discrepancies that are unresolved by PXRD on electrical conductivity cannot be ruled out. In addition to in-plane conductivity, the out-of-plane electronic conduction is expected to contribute to the overall conductivity as both MOFs feature a small π-π stacking distance compared to similar materials.[13,15,16,22]

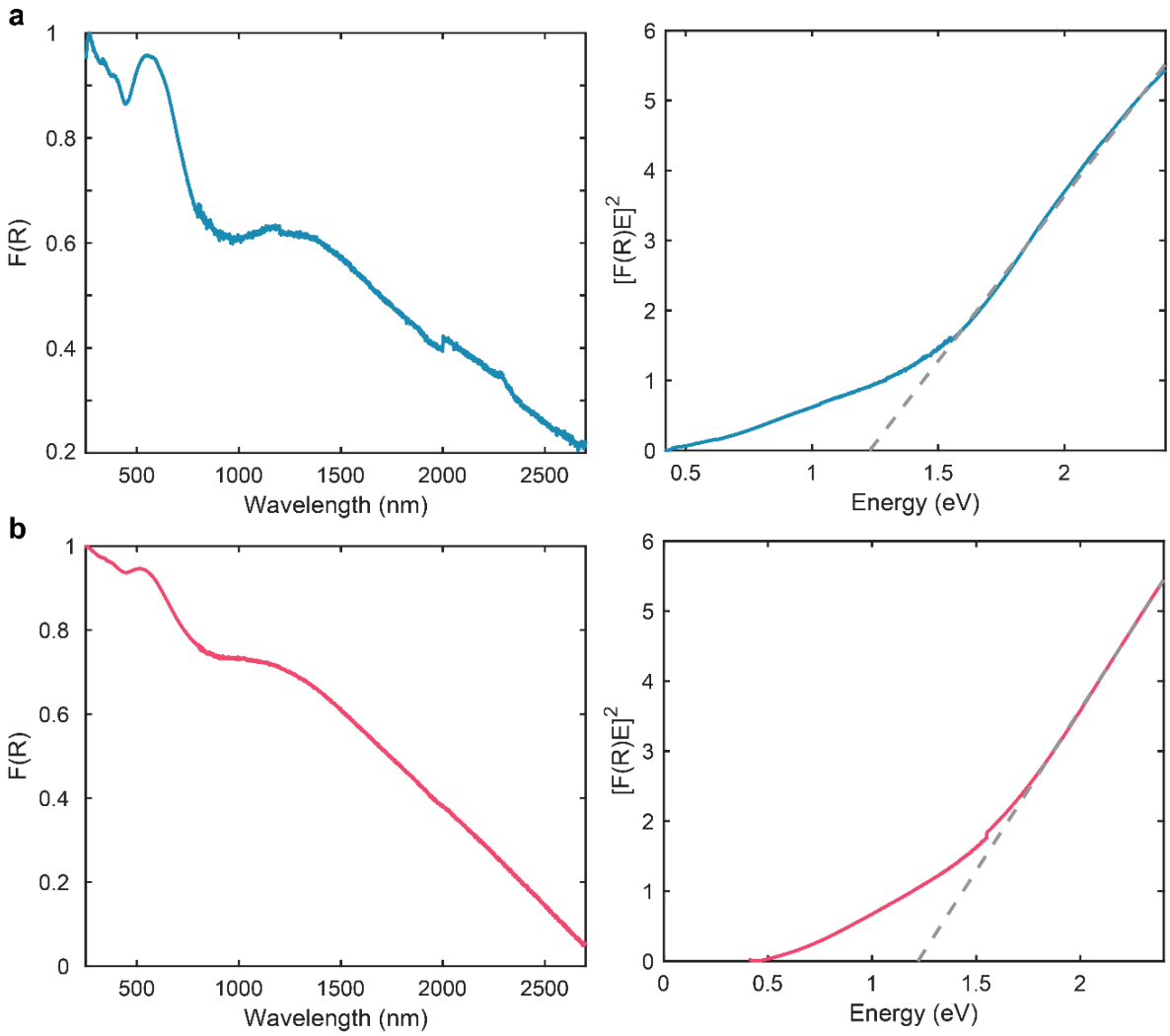

Figure 3-11. DRUV-Vis spectra of a) Cu_3TABC_2 and b) Zn_3TABC_2. The corresponding Tauc plots are shown on the right, yielding direct optical bandgaps of 1.2 and 1.2 eV.

Proton Conductivity

The proton conductivity of Cu_3TABC_2 and Zn_3TABC_2 was tested using electrochemical impedance spectroscopy (EIS). In a typical measurement, MOFs were pressed into pellets and equilibrated at various RH at room temperature before AC currents were applied in linear 2-probe geometries. As seen for Cu_3TABC_2 at 97% RH (**Figure 3-12a**), the Nyquist plot yields a semicircle at high frequencies, tapering off on the real axis at low frequencies. Here, the intercept with the real axis corresponds to the electrical resistance measured with DC currents. The lack of a capacitive tail at low frequencies is indicative of significant contribution of electrical conduction in the material. At this point, the shape of the semicircle in the measured frequency range does not suggest or rule out the presence of a second transport component besides electrical transport. Variation of RH from 11% to 97% does not change the shape of the semicircle or the real axis intercept significantly. EIS of Zn_3TABC_2, however, yields

Nyquist plots that consist of multiple (overlapping) semicircles that are indicative of the presence of at least two transport processes: proton and electron conduction. This is true for measurements at 11%, 53%, 75% and 97% RH (**Figure 3-13**). The lack of a capacitive tail, again, indicates a significant contribution from electronic transport. At 97% RH, the separation of the two semicircles is most significant (**Figure 3-12b**). We note that the lowest frequency semicircle for Zn_3TABC_2 was not completely surveyed in a reliable frequency range. However, we expect the low frequency *x*-axis intercept to coincide with the DC resistance value. To observe the transport properties of dehydrated Zn_3TABC_2, further EIS measurements were performed under dry N_2. The resulting Nyquist plot shows that even at 0% RH, there is a significant contribution of proton conduction in addition to electrical conduction (**Figure 3-14**).

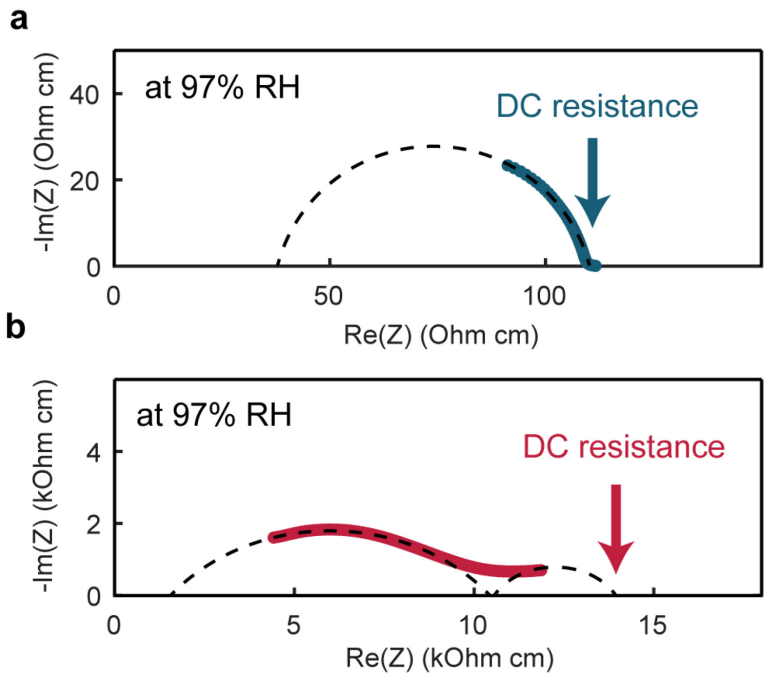

Figure 3-12. EIS of a) Cu_3TABC_2 and b) Zn_3TABC_2 at 97% RH and 25°C. The data for Cu_3TABC_2 shows one semicircle. The x-axis intercept coincides with the DC resistance under otherwise identical conditions. The data for Zn_3TABC_2 indicates the presence of at least two semicircles and therefore transport processes. The DC resistance under otherwise identical conditions is expected to coincide with the end of the low frequency semicircle. The dotted lines are visual guides to illustrate the presence of one or two transport processes

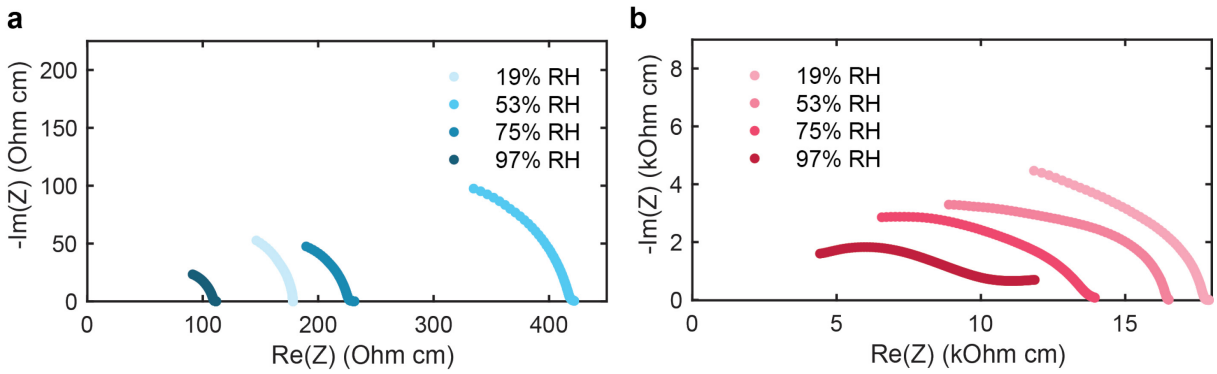

Figure 3-13. Nyquist plots of a) Cu_3TABC_2 and b) Zn_3TABC_2 at various relative humidities at room temperature.

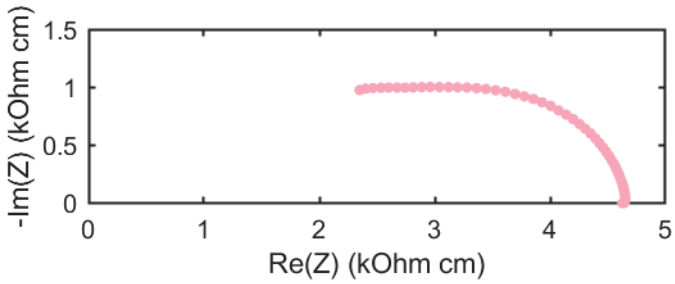

Figure 3-14. Nyquist plot of activated Zn_3TABC_2 at 0% relative humidity at room temperature.

Fitting the EIS data to an equivalent circuit gives quantitative insight into the magnitude of proton conductivity. The equivalent circuit of a typical dual conductor includes the geometric capacitance C_{geo}, electrical resistance R_e and ionic components consisting of R_i, the ionic resistance, and C_{int}, the interfacial capacitance between MOF and electrode, modelled as three parallel rails (**Figure 3-15a**).[23,24] This equivalent circuit describes two semicircles without capacitive tail. As seen earlier, the low frequency intercept $R_2 = R_e$ corresponds to the DC limit of the electrical resistances. The resistance at the *x*-axis intercept R_1 between the two semicircles describes a combination of the electrical and ionic resistances: $1/R_1 = 1/R_e + 1/R_i$. Grain boundaries can be modelled as R_{gb}/C_{gb} in series with the other ionic components, producing a third semicircle. As the present data does not resolve a third semicircle, grain boundary contributions were not considered for the equivalent circuit modelling.

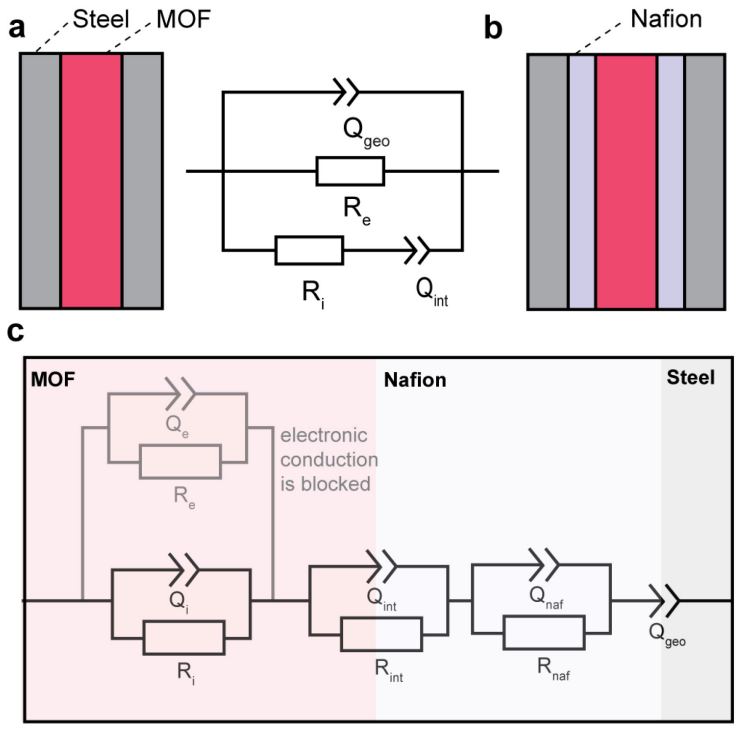

Figure 3-15. a) Schematic of the Stee||MOF||Steel cell and the corresponding equivalent circuit diagram for a mixed ionic-electronic conductor. b) Schematic of the Steel||Nafion||MOF||Nafion||Steel cell setup for blocking measurements and c) the corresponding equivalent circuit diagram. The electronic conduction is blocked by Nafion membranes.

Equivalent circuit fittings of the EIS data for Zn_3TABC_2 yields ionic conductivities of 1.1 to 2.4×10^{-5} S/cm for RH values between 11% and 97%. The data collected at 0% RH could not be modelled due to the lack of higher frequency data points. Overall, the proton conductivity does not show significant humidity dependance.

EIS measurements with electronically blocking layers were performed to confirm the ionic conductivities extracted from the fittings and quantify the ionic conductivity of Cu_3TABC_2. By employing proton conductive Nafion membrane on either side of the MOF pellets, the electronic contact to the current collectors is blocked such that only proton conduction can occur across the sample and membrane (**Figure 3-15b**).[25,26] By shutting off the electronic pathway, it is possible to isolate the ionic components. **Figure 3-15c** shows a model equivalent circuit for blocking measurements. Due to the symmetrical nature of the cell, the RQ circuits on either side are formally combined. AC currents were applied to Steel|Nafion|MOF|Nafion|Steel cells. To facilitate sufficient electrical contact between the MOF and membrane, the measurements were performed in water. For both Cu_3TABC_2 and Zn_3TABC_2, this yields high frequency semicircles with capacitive tails. The semicircles are a result of the ionic transport. At the low frequency DC limit, a capacitive tail appears due to C_{geo}, as the electronic pathway is blocked.

Measurements using various pellet thicknesses show an approximately linear relationship between pellet thickness and resistance from the AC blocking measurements (**Figure 3-16**), indicating that the semicircle indeed is representative of the ionic conductivity of the MOF pellet. EIS measurements under external polarization induced no change in the semicircles, confirming that it does not describe any charge transfer processes (**Figure 3-17**). The high ionic conductivity of the thin Nafion membrane contributes negligible resistance.[27] The blocking measurements yield ionic conductivities of $1.6 \pm 0.1 \times 10^{-5}$ S/cm for Cu_3TABC_2 and $1.9 \pm 0.4 \times 10^{-5}$ S/cm for Zn_3TABC_2. The value for Zn_3TABC_2 is in line with the ionic conductivity extracted from the fitting of non-blocking EIS data.

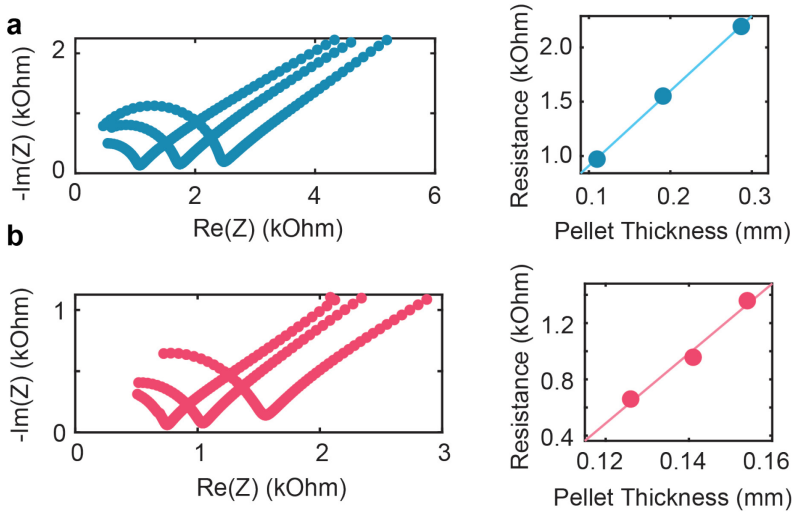

Figure 3-16. Blocking measurements of a) Cu_3TABC_2 and b) Zn_3TABC_2 at three different pellet thicknesses each. The left graphs are Nyquist plot, the right graphs show the linear relationship between resistance and pellet thickness.

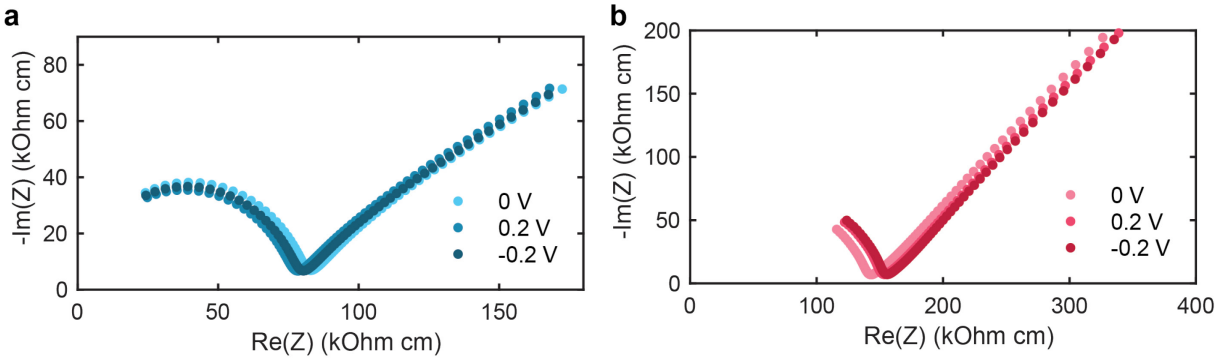

Figure 3-17. Nyquist plots of a) Cu_3TABC_2 and b) Zn_3TABC_2 in blocking setups using Nafion with and without external applied potentials.

Conclusion

Since the electronic conductivity for Cu_3TABC_2 is one thousand times higher than its ionic conductivity, the non-blocking EIS measurements were expectedly dominated by the electronic transport pathway. Only by blocking the electronic pathway does the ionic transport become observable. As electrical and ionic conductivity are closer in magnitude for Zn_3TABC_2, it is possible to observe both processes in non-blocked EIS measurements.

Although typical for 2D conjugated MOFs, examples of high electronic conductivity in mixed conductive MOFs are exceedingly rare. The foregoing results show that designing mixed-conductive MOFs based on 2D MOF structures is a promising strategy to ensure high electronic conductivity. Especially Cu_3TABC_2 has one of the highest electronic conductivities among MOF dual conductors. By targeted incorporation of proton hopping sites through our ligand design, we were able to also achieve high proton conductivity in these 2D MOFs. This strategy may serve as a blueprint for the design of mixed conductive MOFs and shine a spotlight on the potential of ligand design in this field.

3.4 Materials and Supplementary Characterization

3.4.1 Materials

All chemicals were purchased from Sigma Aldrich or Alfa Aesar and used without further purification. Standard Schlenk techniques were used.

3.4.2 Molecular Synthesis

2,3,6,7,10,11-hexamethoxytriphenylene was prepared according to previously reported procedures.[28]

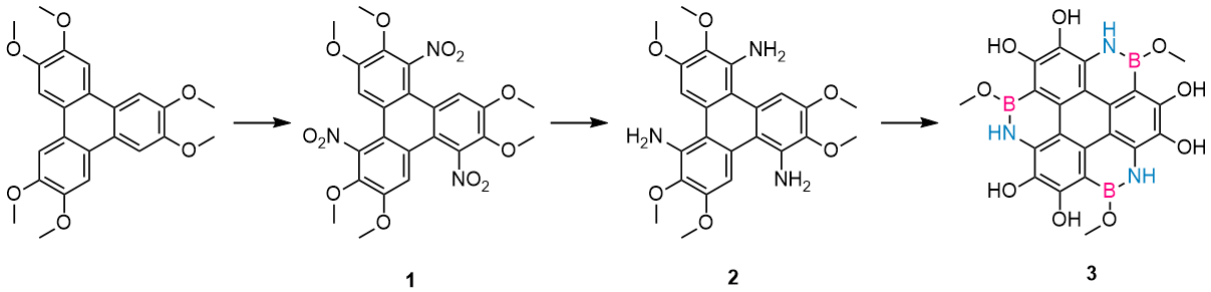

Figure 3-18. Schematic synthetic route from 2,3,6,7,10,11-hexamethoxytriphenylene to 3,4,7,8,11,12-hexamethoxy-1,5,9-triaza-2,6,10-trihydroxybora-coronene in three steps.

1,5,9-trinitro-2,3,6,7,10,11-hexamethoxytriphenylene 1

The procedure was adapted from previous reports.[28] Hexamethoxytriphenylene (10.0 g, 24.5 mmol), TBAB (7.9 g, 24.5 mmol), and $AgNO_3$ (25.0 g, 147.0 mmol) were stirred in dry chloroform (250 mL). *p*-Toluene sulfonyl chloride (28.0 g, 147.0 mmol) was added in portion and the reaction mixture was heated to reflux for 3 days. The solids were removed via filtration and the filtrate poured into water, extracted with DCM and dried under vacuum. The crude product was washed with Et_2O and recrystallized in EtOH to yield 4.8 g (8.8 mmol, 36%) of **1** as a yellow solid. **^{1}H-NMR** ($CDCl_3$): δ [ppm] = 3.99 (s, 3H, OCH_3), 4.06 (s, 3H, OCH_3), 7.59 (s, 3H, CH).

2,3,6,7,10,11-hexamethoxytriphenylene-1,5,9-triamine 2

The procedure was adapted from previous reports.[28] To a mixture of 100 ml THF and 25 ml MeOH was added 2.6 g (4.8 mmol) of **1** and $Ni(OAc)_2{\cdot}4H_2O$ (1.3 g, 5.2 mmol). $NaBH_4$ (3.14 g, 83.0 mmol) was added carefully in portions and a fine black precipitate was immediately

deposited. The mixture continued to stir for 4 h before 40 mL water was added. Solids were removed by filtration and the solvents were evaporated under reduced pressure. The product were washed with EtOH and dried under vacuum to yield **2** as a beige solid (2.0 g, 4.4 mmol, 92%).

3,4,7,8,11,12-hexamethoxy-1,5,9-triaza-2,6,10-trihydroxybora-coronene 3 (TABC-OMe) **2** (0.40 g, 0.88 mmol) was loaded into a flame dried Schlenk flask with 15 ml of dry 1,2-dichlorobenzene. The mixture was degassed with three freeze-pump-thaw cycles and heated to 180 °C for 36 h under N_2. After cooling to r.t., the solvent was removed under vacuum. Degassed MeOH was carefully added to the remaining solids. Then, the solids were isolated via centrifugation and washed with MeOH (3x) and dried to give **3** as grey solids (0.34 mg, 0.67 mmol, 78%). **^{1}H-NMR** (DMSO-d6): δ [ppm] = 3.17 (s, 3H, CH_3), 7.79 (s, 1H, CH), 9.00 (s, 1H, OH), 9.19 (s, 1H, OH). **^{13}C-NMR** (DMSO-d6): δ [ppm] = 48.61, 101.97, 109.37, 127.72, 127.75, 132.49, 148.69. **HRMS** (AccuTOF-DART) *m/z* calcd for TABC-OMe$^+$: m/z =490.13950, found: 490.13929. **Elemental Anal.** Calcd for $C_{21}H_{18}B_3N_3O_9 \cdot 2.9H_2O$: C, 46.54; H, 4.44; N, 7.75. Found: C, 46.35; H, 3.07; N, 7.79.

NMR and HRMS spectra can be found in **Sections 2.12** and **2.13**. It is to note that when solids are quenched with water or other alcohols such as propanol, OH or O(C_3H_7) replace the intermediate bromide, forming B-OH or B-O(C_3H_7) groups. These molecules can also be used in subsequent syntheses of MOFs.

3.4.3 MOF Synthesis

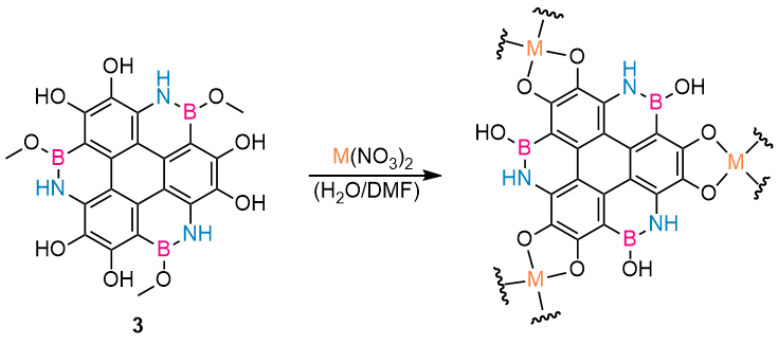

Figure 3-19. Schematic synthetic step from TABC-OMe to TABC MOFs.

MOFs are synthesized using TABC-OMe yielding TABC MOFs featuring OH groups, as alkoxide groups are replaced during the heating in aqueous solution. The ratio of DMF/water

as well as the concentration of NaOAc must be optimized for each starting ligand molecule to produce highly crystalline MOFS, as their solubility and reaction kinetics differ. Optimized procedures using TABC-OMe starting material are shown below.

Cu_3TABC_2

10 mg of TABC-OMe were dissolved in 0.2 ml DMF. The aqueous salt solution was created by mixing 40 µL of 1M $Cu(NO_3)_2$ solution, 0.4 mL of 1M NaOAc solution and 3.4 mL water. salt solution was added to the ligand solution and the mixture was heated in a capped vial at 85°C for 4 h. The solids were isolated and washed with water, methanol and acetone. **Elemental analysis:** Calcd for $C_{36}H_{12}B_6N_6O_{18}Cu_3 \cdot 14.3H_2O$: C, 32.52; H, 3.08 N, 6.32. Found: C, 32.56; H, 2.60; N, 6.04.

Zn_3TABC_2

10 mg of TABC-OMe were dissolved in 2 ml DMF. The aqueous salt solution was created by mixing 40 µL of 1M $Zn(NO_3)_2$ solution, 0.6 mL of 1M NaOAc solution and 1.4 mL water. salt solution was added to the ligand solution and the mixture was heated in a capped vial at 85°C for 4 h. The solids were isolated and washed with water, methanol and acetone. **Elemental analysis:** Calcd for $C_{36}H_{12}B_6N_6O_{18}Zn_3 \cdot 12.6H_2O$: C, 33.11; H, 2.80; N, 6.49. Found: C, 33.36; H, 2.13; N, 5.90.

3.4.4 Characterization Methods

Electrochemical characterization.

Electrical measurements were performed with custom linear 2-electrode devices. In a typical setup, the sample was loaded into a PTFE die of 2 mm diameter. Steel pins were used as the electrodes on each side of the pellet. DC measurements were performed using a Keithley model 2450 source meter. AC measurements at frequencies between 500 kHz and 5 Hz were performed using a BioLogic VSP. Real and imaginary components of the impedances shown in Nyquist plots are given as resistivity values by multiplying the resistance by A/t, where A is the area and t is the thickness of the pellet.

Humidity dependent measurements were performed at room temperature in home-built humidity chambers using saturated solutions of LiCl, NaCl, $Mg(NO_3)_2$, and K_2SO_4 at 11%, 53%, 75%, and 97% relative humidity. Samples in pellet form were equilibrated for 1 h at each

humidity before measurements. External pressure was applied using hand-tight c-clamps during all measurements.

Blocking measurements were performed in custom Swagelock cells with 10mm diameter stainless steel rod electrodes. The MOFs were pelletized at 1 ton pressure for 30 seconds, sandwiched between Nafion™ NR212 (Ion Power) membranes and fixed between the steel rods. The cell chamber was then filled with Millipore water. EIS measurements were carried out by a SP-200 potentiostat at frequencies between 2 MHz and 10 Hz. The ionic resistance related to the semicircle visible in the blocking measurements was extracted using a simplified equivalent circuit:

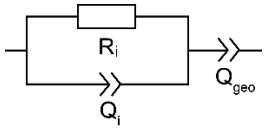

Figure 3-20. Equivalent circuit for fitting EIS to Nafion blocked measurements.

Cryogenic high resolution transmission electron microscopy (Cryo-HRTEM)

Cryo-HRTEM images were obtained at the Automated Cryogenic Electron Microscopy Facility at MIT.nano on a Talos Arctica G2 microscope operated at an accelerating voltage of 200 kV with a Falcon3EC direct electron detector. Samples were prepared by sonicating MOFs powders in isopropanol for 5 to 10 seconds. Specimens were prepared by drop-casting sonicated samples onto copper grids with holey carbon. All image acquisitions were done using EPU at an exposure time of 2 to 3 s. Analysis of the raw HRTEM data was done using Gatan Microscopy Suite software (GMS 3).

Elemental analyses (EA)

EA was performed by Robertson Microlit Laboratories, Ledgewood, New Jersey.

Infrared spectroscopy (IR)

IR spectra were recorded in a nitrogen-filled glovebox on a Bruker Alpha FTIR spectrometer equipped with an attenuated total reflectance accessory.

Nuclear magnetic resonance spectroscopy (NMR)

NMR spectra were collected in a Bruker Avance Neo spectrometer operating at 400.17 MHz with a 5 mm BBFO SmartProbe and internally referenced to the residual solvent signal.

High resolution mass spectrometry (HR-MS)

Mass spectra were collected using the JEOL AccuTOF 4G LC-plus equipped with an ionSense DART (Direct Analysis in Real Time) source. The spectra were collected using solid samples in positive ion mode, with the heater at 400 °C.

N_2 sorption isotherms

N_2 isotherms were measured by a volumetric method using a Micromeritics 3Flex sorption analyzer using liquid nitrogen baths (77 K). Samples were heated to 70 °C under a vacuum of 0.3 mtorr for 16 h prior to the analysis. Ultrahigh purity grade (99.999% purity) N_2, oil-free valves and gas regulators were used for all the free space correction and measurement.

Powder X-ray diffraction (PXRD)

PXRD patterns were recorded with a Bruker D8 Advance diffractometer equipped with a Göbel mirror, rotating sample stage, LynxEye detector and Cu Kα (λ = 1.5406 Å) X-ray source in a θ = 2θ Bragg–Brentano geometry. An anti-scattering slit (1 mm) and an exchangeable detector slit (8 mm) were used. The tube voltage and current were 40 kV and 40 mA, respectively. Knife-edge attachments were used to remove scattering at low angles. Samples for PXRD were prepared by placing powders on a zero-background silicon (510) crystal plate. Pawley refinement was performed on experimental data using pseudo-Voigt functions in TOPAS.

Table 3-4. Statistics of Pawley refinements for Cu_3TABC_2 and Zn_3TABC_2.

	R_{wp}	R_p	GoF	Cell parameters
Cu_3TABC_2	2.00	1.56	1.22	*a*=*b*=21.03 Å, *c*=3.24 Å
Zn_3TABC_2	5.07	3.84	1.05	*a*=*b*=21.11 Å, *c*=3.16 Å

Scanning electron microscopy (SEM)

SEM was conducted at MIT.Nano on a Zeiss Merlin high-resolution scanning electron microscope with InLens detector at an operating voltage of 3 kV.

Thermogravimetric analysis (TGA)

TGA was performed on a TA Instruments Q500 Thermogravimetric Analyzer at a heating rate of 2.0 °C/min under air flow of 5 mL/min on a platinum pan.

UV-Vis diffuse reflectance spectra (DRUV-Vis)

DRUV-Vis spectra were obtained using a Cary 5000i spectrophotometer, fitted with the UV/Vis DiffusIR accessory (Pike Technologies), at a scan speed of 200 nm/min under ambient conditions. Prior to sample measurements, a baseline using KBr was collected. Samples were diluted to 1 wt% in KBr. After data collection, the Kubelka-Munk function was applied to the raw data to eliminate scattering.

Water vapor adsorption isotherms

Water vapor adsorption isotherms and were measured using a gravimetric method with a Hiden Analytical XEMIS microbalance equipped with a vapor dose option. A typical sample of MOF weighing approximately 5 mg was loaded into the microbalance basket and subjected to external furnace activation at 70°C. The water analyses were carried out at room temperature using a programmable water bath with a recirculating chiller, and oil-free vacuum pumps were utilized to avoid any sample or feed gas contamination.

X-ray photoelectron spectroscopy (XPS)

XPS measurements were performed at MIT.nano using a Physical Electronics PHI Versaprobe II X-ray photoelectron spectrometer equipped with a monochromatic Al anode X-ray source. The main chamber pressure was in the 10^{-10} Torr range.

3.4.5 Supplementary Characterization

NMR Spectra

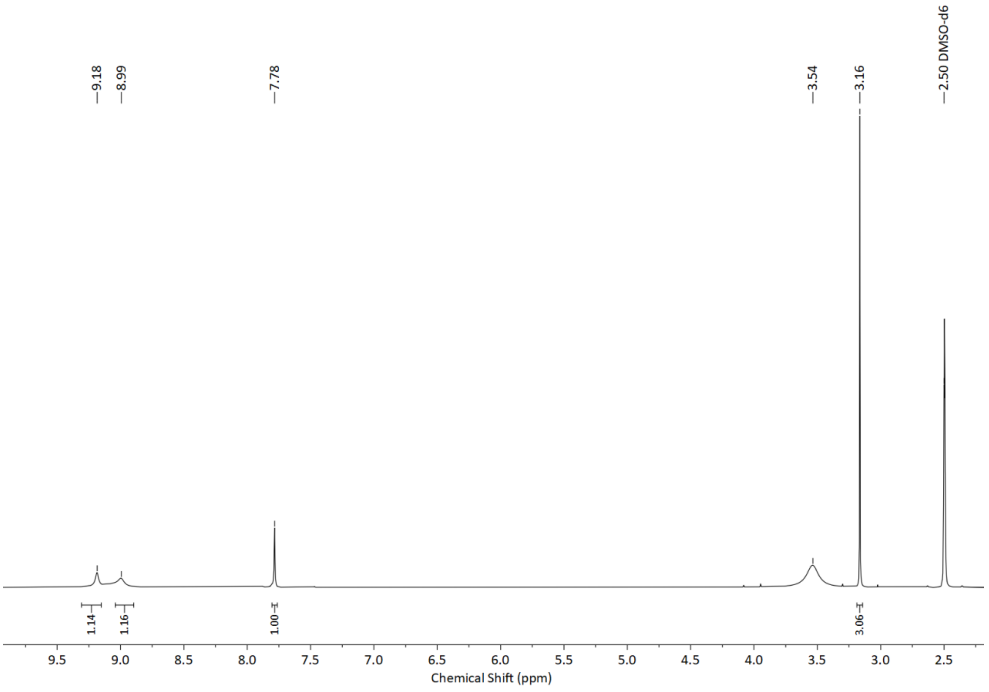

Figure 3-21. ^{1}H NMR spectrum of TABC-OMe (DMSO-d6, 400 MHz).

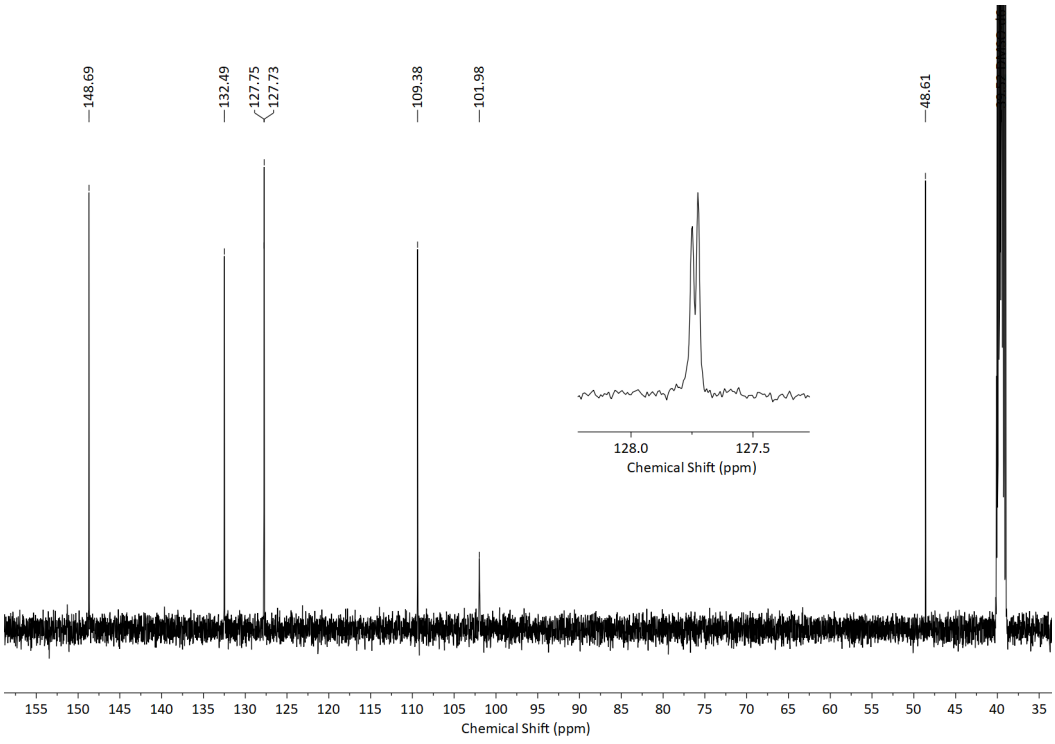

Figure 3-22. ^{13}C NMR spectrum of TABC-OMe (DMSO-d6). The inset is a magnification of the two peaks at 127.73 and 127.75 ppm.

Mass Spectrum

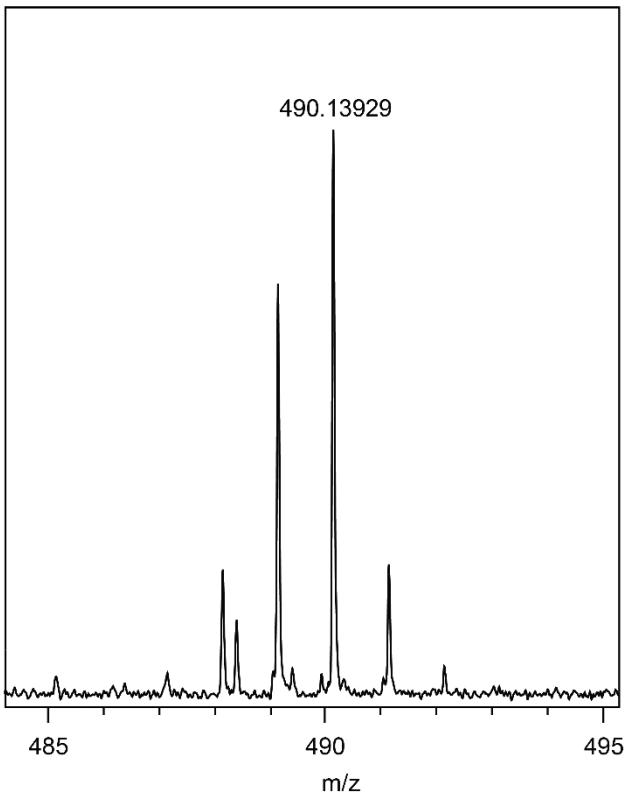

Figure 3-23. High resolution mass spectrum of TABC-OMe.

3.5 References

(1) Wang, Y.; Wustoni, S.; Surgailis, J.; Zhong, Y.; Koklu, A.; Inal, S. Designing Organic Mixed Conductors for Electrochemical Transistor Applications. *Nat. Rev. Mater.* **2024**, *9* (4), 249–265.

(2) Fabbri, E.; Pergolesi, D.; Traversa, E. Materials Challenges toward Proton-Conducting Oxide Fuel Cells: A Critical Review. *Chem. Soc. Rev.* **2010**, *39* (11), 4355–4369.

(3) Merkle, R.; Hoedl, M. F.; Raimondi, G.; Zohourian, R.; Maier, J. Oxides with Mixed Protonic and Electronic Conductivity. *Annu. Rev. Mater. Res.* **2021**, *51*, 461–493.

(4) Choi, J. Y.; Stodolka, M.; Kim, N.; Pham, H. T. B.; Check, B.; Park, J. 2D Conjugated Metal-Organic Framework as a Proton-Electron Dual Conductor. *Chem* **2023**, *9* (1), 143–153.

(5) Ribeiro, C.; Tan, B.; Figueira, F.; Mendes, R. F.; Calbo, J.; Valente, G.; Escamilla, P.; Paz, F. A. A.; Rocha, J.; Dincă, M.; Souto, M. Mixed Ionic and Electronic Conductivity in a Tetrathiafulvalene-Phosphonate Metal-Organic Framework. *J. Am. Chem. Soc.* **2024**, *147*, 48.

(6) Lu, C.; Choi, J. Y.; Check, B.; Fang, X.; Spotts, S.; Nuñ Ez, D.; Park, J. Thiatruxene-Based Conductive MOF: Harnessing Sulfur Chemistry for Enhanced Proton Transport. *J. Am. Chem. Soc.* **2024**, *146* (38), 26313–26319.

(7) Sadakiyo, M.; Yamada, T.; Kitagawa, H. Rational Designs for Highly Proton-Conductive Metal-Organic Frameworks. *J. Am. Chem. Soc.* **2009**, *131* (29), 9906–9907.

(8) Li, A. L.; Gao, Q.; Xu, J.; Bu, X. H. Proton-Conductive Metal-Organic Frameworks: Recent Advances and Perspectives. *Coord. Chem. Rev.* **2017**, *344*, 54–82.

(9) Xie, L. S.; Skorupskii, G.; Dincă, M. Electrically Conductive Metal-Organic Frameworks. *Chem. Rev.* **2020**, *120* (16), 8536–8580.

(10) Kharod, R. A.; Andrews, J. L.; Dinca, M. Teaching Metal-Organic Frameworks to Conduct: Ion and Electron Transport in Metal-Organic Frameworks. *Annu. Rev. Mater. Res.* **2022**, *52*, 103–128.

(11) Dou, J. H.; Arguilla, M. Q.; Luo, Y.; Li, J.; Zhang, W.; Sun, L.; Mancuso, J. L.; Yang, L.; Chen, T.; Parent, L. R.; Skorupskii, G.; Libretto, N. J.; Sun, C.; Yang, M. C.; Dip, P. V.; Brignole, E. J.; Miller, J. T.; Kong, J.; Hendon, C. H.; Sun, J.; Dincă, M. Atomically Precise Single-Crystal Structures of Electrically Conducting 2D Metal–Organic Frameworks. *Nat. Mater.* **2020**, *20* (2), 222–228.

(12) Apostol, P.; Gali, S. M.; Su, A.; Tie, D.; Zhang, Y.; Pal, S.; Lin, X.; Bakuru, V. R.; Rambabu, D.; Beljonne, D.; Dincă, M.; Vlad, A. Controlling Charge Transport in 2D Conductive MOFs–The Role of Nitrogen-Rich Ligands and Chemical Functionality. *J. Am. Chem. Soc.* **2023**, *145*, 9.

(13) Yin, J. C.; Lian, X.; Li, Z. G.; Cheng, M.; Liu, M.; Xu, J.; Li, W.; Xu, Y.; Li, N.; Bu, X. H. Triazacoronene-Based 2D Conductive Metal–Organic Framework for High-Capacity Lithium Storage. *Adv. Func. Mater.* **2024**, *34* (41), 2403656.

(14) Li, G.; Xiong, W. W.; Gu, P. Y.; Cao, J.; Zhu, J.; Ganguly, R.; Li, Y.; Grimsdale, A. C.; Zhang, Q. 1,5,9-Triaza-2,6,10-Triphenylboracoronene: BN-Embedded Analogue of Coronene. *Org. Lett.* **2015**, *17* (3), 560–563.

(15) Campbell, M. G.; Sheberla, D.; Liu, S. F.; Swager, T. M.; Dincə, M. Cu3(Hexaiminotriphenylene)$_2$: An Electrically Conductive 2D Metal–Organic Framework for Chemiresistive Sensing. *Angew. Chem. Intl. Ed.* **2015**, *54* (14), 4349–4352.

(16) Sheberla, D.; Sun, L.; Blood-Forsythe, M. A.; Er, S.; Wade, C. R.; Brozek, C. K.; Aspuru-Guzik, A.; Dincă, M. High Electrical Conductivity in Ni_3(2,3,6,7,10,11-Hexaiminotriphenylene)$_2$, a Semiconducting Metal-Organic Graphene Analogue. *J. Am. Chem. Soc.* **2014**, *136* (25), 8859–8862.

(17) Campbell, P. G.; Marwitz, A. J. V.; Liu, S. Y. Recent Advances in Azaborine Chemistry. *Angew. Chem. Intl. Ed.* **2012**, *51* (25), 6074–6092.

(18) Zhang, K. J.; Chen, T.; Oppenheim, J. J.; Yang, L.; Palatinus, L.; Müller, P.; Van Voorhis, T.; Dincă, M. High-Resolution Structure of Zn_3(HOTP)$_2$ (HOTP = Hexaoxidotriphenylene), a Three-Dimensional Conductive MOF. *Chem. Sci.* **2025**, *16*, 12416-12420.

(19) Wang, J., Chen, T., Jeon, M., Oppenheim, J.J., Tan, B., Kim, J., and Dincă, M. Superior Charge Transport in Ni-Diamine Conductive MOFs. *J. Am. Chem. Soc.* **2024** *146*, 20500–20507.

(20) Xie, L. S.; Sun, L.; Wan, R.; Park, S. S.; Degayner, J. A.; Hendon, C. H.; Dincă, M. Tunable Mixed-Valence Doping toward Record Electrical Conductivity in a Three-Dimensional Metal-Organic Framework. *J. Am. Chem. Soc.* **2018**, *140* (24), 7411–7414.

(21) Murase, R.; Leong, C. F.; D'Alessandro, D. M. Mixed Valency as a Strategy for Achieving Charge Delocalization in Semiconducting and Conducting Framework Materials. *Inorg. Chem.* **2017**, *56* (23), 14373–14382.

(22) Skorupskii, G.; Trump, B. A.; Kasel, T. W.; Brown, C. M.; Hendon, C. H.; Dincă, M. Efficient and Tunable One-Dimensional Charge Transport in Layered Lanthanide Metal–Organic Frameworks. *Nat. Chem.* **2019**, *12* (2), 131–136.

(23) Huggins, R. A. Simple Method to Determine Electronic and Ionic Components of the Conductivity in Mixed Conductors a Review. *Ionics* **2002**, *8* (3–4), 300–313.

(24) Jamnik, J.; Maier, J. Treatment of the Impedance of Mixed Conductors Equivalent Circuit Model and Explicit Approximate Solutions. *J. Electrochem. Soc.* **1999**, *146* (11), 4183–4188.

(25) Bayer, T.; Bishop, S. R.; Perry, N. H.; Sasaki, K.; Lyth, S. M. Tunable Mixed Ionic/Electronic Conductivity and Permittivity of Graphene Oxide Paper for Electrochemical Energy Conversion. *ACS Appl. Mater. Interfaces* **2016**, *8* (18), 11466–11475.

(26) Deslouis, C.; El Moustafid, T.; Musiani, M. M.; Tribollet, B. Mixed Ionic-Electronic Conduction of a Conducting Polymer Film. AC Impedance Study of Polypyrrole. *Electrochim. Acta* **1996**, *41* (7–8), 1343–1349.

(27) Safronova, E. Y.; Voropaeva, D. Y.; Lysova, A. A.; Korchagin, O. V.; Bogdanovskaya, V. A.; Yaroslavtsev, A. B. On the Properties of Nafion Membranes Recast from Dispersion in N-Methyl-2-Pyrrolidone. *Polymers* **2022**, *14* (23), 5275.

(28) Sun, Y. X.; Wang, X. G.; Shen, G. D.; Yang, T; Yang, Y. H.; Li, J.; Yang, M. Y.; Sun, H. M.; Wei, J.F. A 6π Azaelectrocyclization Strategy towards the 1, 5, 9-Triazacoronenes. *Adv. Synth. Catal.* **2020**, *362* (8), 1651-1656.

Chapter Specific Acknowledgement

I would like to thank Dr. Julius J. Oppenheim for performing the molecular DFT calculations and collecting the water sorption isotherm data. Cryo-HRTEM data was collected with the assistance of Dr. Jenn Podgorski and Dr. Sarah Sterling at the Automated Cryogenic Electron Microscopy Facility at MIT.nano on a Talos Arctica microscope, which was a gift from the Arnold and Mabel Beckman Foundation. SEM, and XPS data were also collected at the MIT.nano shared characterization facilities. The experimental work was financially supported by the Department of Energy (DE-SC0023288).

Chapter 4

Electrochemical Capacitance Traces with Interlayer Spacing in Two-dimensional Conductive Metal–Organic Frameworks

4.1 Abstract

Electrically conductive metal–organic frameworks (MOFs) are promising candidates for electrochemical capacitors (EC) for fast energy storage due to their high specific surface areas and potential for redox activity. To maximize energy density, traditional inorganic pseudocapacitors have utilized faradaic processes in addition to double-layer capacitance. Although conductive MOFs are usually comprised of redox active ligands which allow faradaic reactions upon electro-chemical polarization, systematic studies providing deeper understanding of the charge storage processes and structure-function relationships have been scarce. Here, we investigate the charge storage mechanisms of a series of triazatruxene-based 2D layered conductive MOFs with variable alkyl functional groups, $Ni_3(HIR_3\text{-}TAT)_2$ (TAT = triazatruxene; R=H, Et, *n*-Bu, *n*-Pent). Functionalization of the triazatruxene core allows for systematic variation of structural parameters while maintaining in-plane conjugation between ligands and metals. Specifically, R groups modulate interlayer spacing, which in turn shifts the charge storage mechanism from double-layer capacitance towards pseudocapacitance, leading to an increase in molar specific capacitance from $Ni_3(HIH_3\text{-}TAT)_2$ to $Ni_3(HIBu_3\text{-}TAT)_2$. Partial exfoliation of $Ni_3(HIBu_3\text{-}TAT)_2$ renders redox active ligand moieties more accessible and thus increases the dominance of faradaic processes. Our strategy of controlling charge storage mechanism through tuning the accessibility of redox-active sites may motivate further design and engineering of electrode materials for EC.

4.2 Introduction

Electrochemical capacitors (EC) bridge the gap between traditional parallel plate capacitors and batteries in terms of energy and power density.[1] Pure double-layer capacitors store energy via the formation of electrochemical double layers (EDL) consisting of physisorbed electrolyte ions. In ideal EDL capacitors, the specific surface area of the active electrode material is directly proportional to the amount of charge stored.[2] However, this charge storage capacitance can be supplemented by rapid Faradaic processes in materials such as $RuO_2 \cdot xH_2O$ and Nb_2O_5, which are said to operate as pseudocapacitors.[3] Non-porous coordination polymers have also been demonstrated to deliver high capacitance due to faradaic cation intercalation.[4,5] Electrically conductive 2D metal–organic frameworks (c-MOFs) are porous hybrid organic–inorganic materials that have emerged as viable materials for supercapacitors based on their high specific surface areas and efficient charge transport.[6-8] In many conductive MOFs, redox active ligands engage in charge transfer processes, leading to improved energy densities, while porosity increases ion access to the redox sites.[9,10] Importantly, the role of confinement of electrolyte ions in the pores of layered materials has received a lot of attention, revealing that matching of ion and pore size can lead to ion desolvation and greater charge density.[11-13] Yet, exploring specific aspects of charge storage in EC has been difficult because changing composition leads to multiple structural and/or physical changes that are challenging to deconvolute.

Due to their high tunability, c-MOFs serve as an excellent platform to rationally vary structural properties to probe charge storage with a wholistic view of both electronic and mass transport mechanisms. Recently, ligand tuning by alkylation of the triazatruxene (TAT) ligands before assembly to 2D TAT MOFs has been demonstrated.[14-16] It has been shown that the specific surface area of this family of MOFs can be tuned by changing the length of alkyl chains occupying the free pore space. Additionally, the stacking distance of the 2D sheets is likewise dependent on the alkyl substituents disturbing the interlayer π-stacking interactions. This enables the investigation of the effects of interlayer spacing and pore size on the capacitive mechanisms. Herein, we show that with c-MOFs, there is a direct relationship between interlayer spacing and capacitance and that, surprisingly, increasing the interlayer spacing causes a shift in the mechanism of charge storage itself, from physical capacitance to a large contribution of faradaic pseudocapacitive processes.

4.3 Results and Discussion

Synthesis and Structural Characterization

Solvothermal reaction between nickel acetate and variously *N*-functionalized hexaaminotriazatruxene (HATAT) ligands in aqueous sodium acetate/*N*,*N*-dimethylformamide/*N*,*N*-dimethylacetamide yields four isostructural HATAT-based hexagonal 2D layered c-MOFs with the general formula $Ni_3(HIR_3\text{-}TAT)_2$ (R=-H, -Et, -*n*-Bu, -*n*-Pent; abbreviated as H-MOF, Et-MOF, Bu-MOF, and Pent-MOF, respectively) (**Figure 4-1** and **4-2**).[15,16]

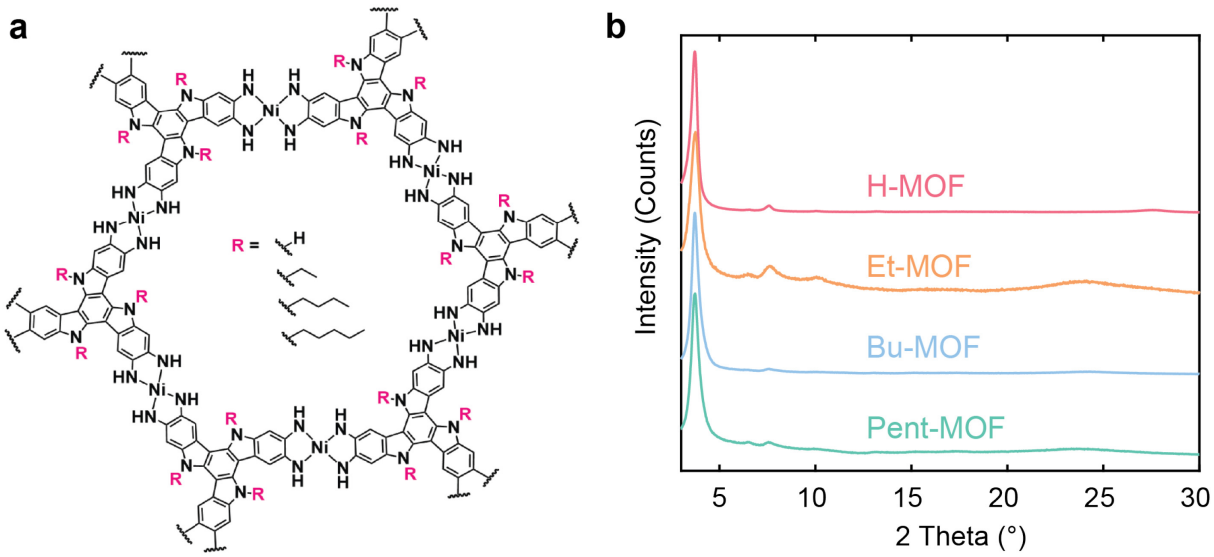

Figure 4-1 a) Schematic structure of TAT MOFs with various side chains. b) PXRD patterns of H-MOF, Et-MOF, Bu-MOF, and Pent-MOF.

We found that with these TAT-based MOFs, longer alkyl chains lead to more rapid precipitation, yielding materials with lower crystallinity under otherwise identical synthetic conditions. Increasing the pH of the reaction mixture through the addition of increasing amounts of sodium acetate improves the crystallinity of Pent-MOF (**Figure 4-3**).

Infrared spectra of the frameworks show increasing relative intensities of alkyl C−H stretching bands when going from H-MOF to Et-MOF, Bu-MOF, and Pent-MOF (**Figure 4-4**). Powder X-ray diffraction analysis demonstrated that all four MOFs display comparable in-plane structural order, as verified by the similar full-widths-at-half-maximum values, ~0.5°, of the (100) reflections at 2θ=3.76° (**Figure 4-5** and **Table 4-1**).

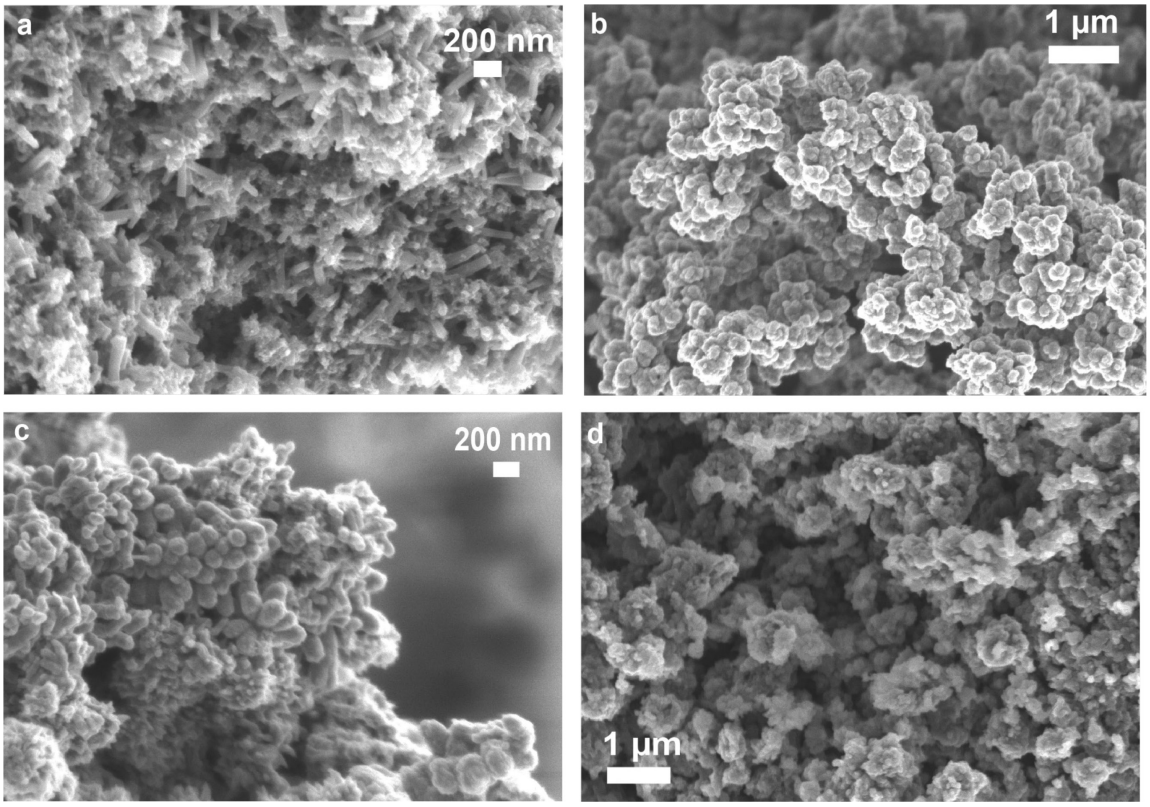

Figure 4-2. SEM images of a) H-MOF, b) Et-MOF, c) Bu-MOF and d) Pent-MOF.

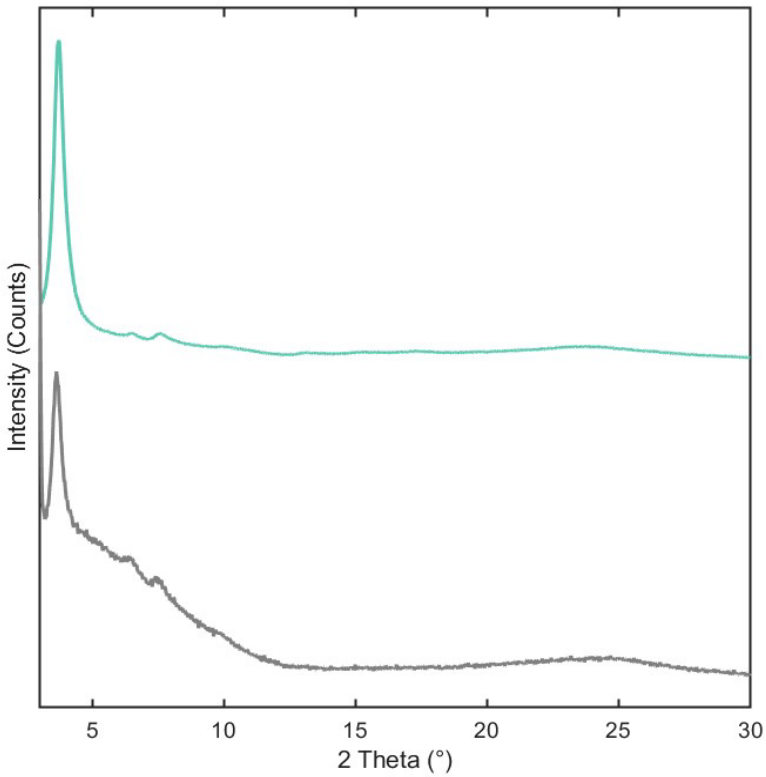

Figure 4-3. PXRD pattern of Pent-MOF (top) compared to the material formed under less basic reaction condition (bottom).

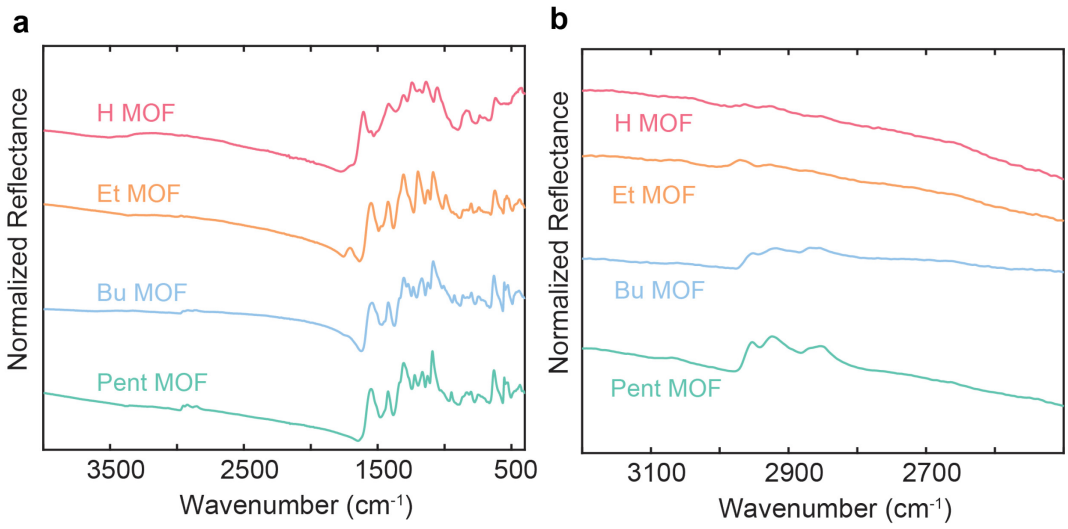

Figure 4-4. a) Full ATR-IR spectra of H-MOF, Et-MOF, Bu-MOF, and Pent-MOF and b) zoomed in region of alkyl C-H stretches.

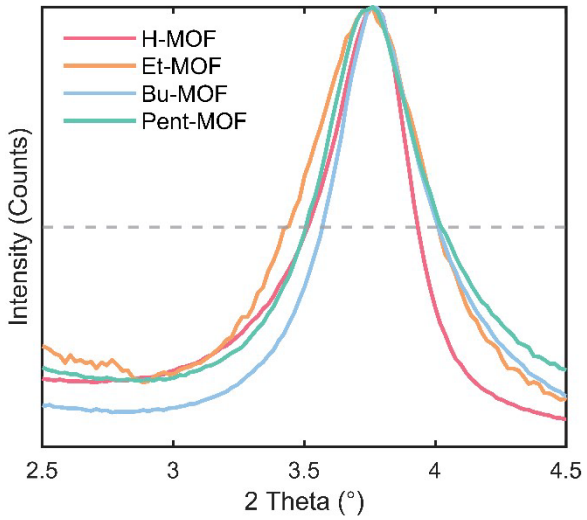

Figure 4-5. PXRD of (100) reflection of H-MOF, Et-MOF, Bu-MOF, and Pent-MOF. Full width at half maximum of the four MOF are approximately 0.5°, indicating comparable crystallinity.

Table 4-1. Full widths at half maximum of (100) reflections of H-MOF, Et-MOF, Bu-MOF, and Pent-MOF.

	Full widths at half maximum of (100) reflections (°)
H-MOF	0.40
Et-MOF	0.57
Bu-MOF	0.43
Pent-MOF	0.51

The stacking distance of the 2D sheets increases with increasing alkyl chain length from 3.29 Å for H-MOF to 3.63 Å, 3.69 Å and 3.72 Å for Et-MOF, Bu-MOF and Pent-MOF, respectively, as calculated from the (001) reflections between 2θ=23° and 28° (**Figure 4-6a**). The attenuated π–π stacking interaction induced by increasing the alkyl chain length leads to lower electronic coupling in the *c*-direction and reduced band dispersion, ultimately decreasing electrical conductivity from 1.9 mS/cm for H-MOF to 1.1 mS/cm, 0.50 mS/cm, and 0.13 mS/cm for Et-MOF, Bu-MOF and Pent-MOF, respectively (**Figure 4-6b**). N_2 sorption isotherms at 77 K gave apparent BET surface areas that decrease with chain length due to the alkyl chains residing in the pores: 735 m^2/g, 664 m^2/g, 522 m^2/g, and 421 m^2/g for H-MOF through Pent-MOF (**Figure 4-6c**). The total pore volume similarly decreases with increasing alkyl chain length (**Table 4-2**).

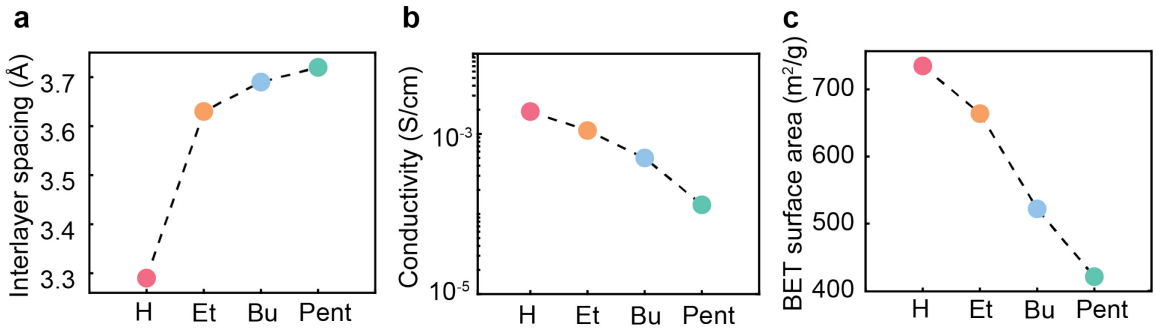

Figure 4-6. a) Progression of interlayer spacings across the series of MOFs, determined from (001) reflections. b) Electronic conductivities and c) BET surface areas of MOFs.

The foregoing analytical data confirm that side chain engineering of the organic linker modulates the interlayer distance, specific surface area, and accessible pore volumes of this series of TAT-based 2D conductive MOFs. As such, this family of frameworks serves as an ideal platform to correlate structurally induced effects with charge storage behavior. Electronic effects, dominated by in-plane conjugation and minimally influenced only by the degree of interlayer band dispersion, are effectively decoupled from structural changes.[13]

Electrochemical Characterization

Electrochemical characterization was performed in a three-electrode configuration. A mixture of c-MOF and conductive carbon with a mass ratio of 9 : 1 was pressed directly onto nickel foam as the working electrode, whereas an activated carbon pellet electrode with at least ten times higher mass than the MOF was used as the counter electrode. A LiTFSI (TFSI=trifluoromethanesulfonylimide) 1 m solution in acetonitrile was identified as a suitable electrolyte due to the large accessible voltage window of acetonitrile and stability of the c-

MOFs in this solvent (Figure S6). Cyclic voltammetry (CV) shows quasi-rectangular traces for all four materials in cathodic sweeps from 0.2 V to 0.0 V referenced against a silver wire pseudo-reference electrode (**Figure 4-7**). The molar specific capacitances (given per mol of TAT ligand) were determined from CV scans at scan rates between 3 mV/s and 100 mV/s. At low scan rates up to 20 mV/s, the molar specific capacitance increases with increasing interlayer distance from H-MOF to Et-MOF to Bu-MOF by up to a factor of 1.7 but decreases from Bu-MOF to Pent-MOF (**Figure 4-8**). Because specific capacitance and specific surface area follow inverse trends across the series of c-MOFs, it can be inferred that a second capacitive component, likely faradaic, contributes to the overall capacitance and it increases with alkyl chain length and interlayer distance.

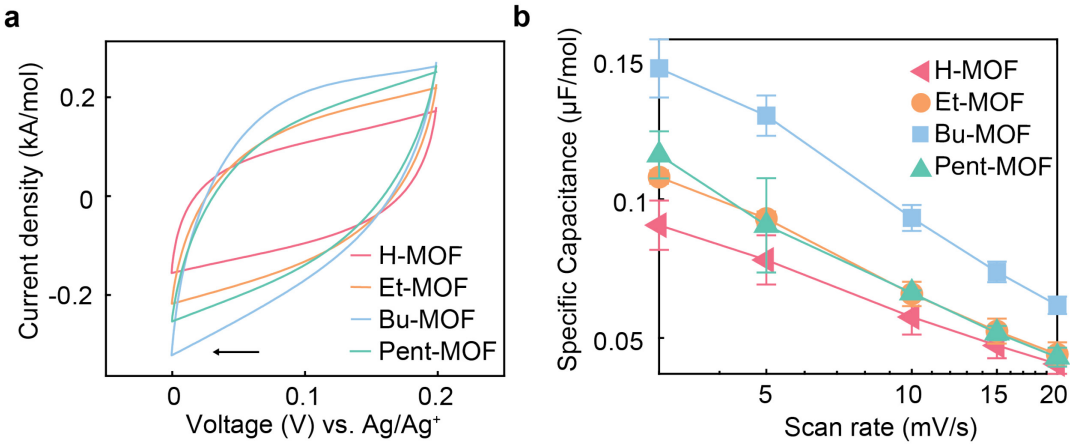

Figure 4-7. a) CV traces of c-MOFs in three electrode cells from 0.2 V to 0.0 V vs. Ag-wire pseudo-reference. The second cycle is shown. Molar current densities are normalized vs. moles of TAT ligand. b) Molar specific capacitances (normalized vs. moles of TAT ligand) determined from CV scans at scan rates from 3 to 20 mV/s.

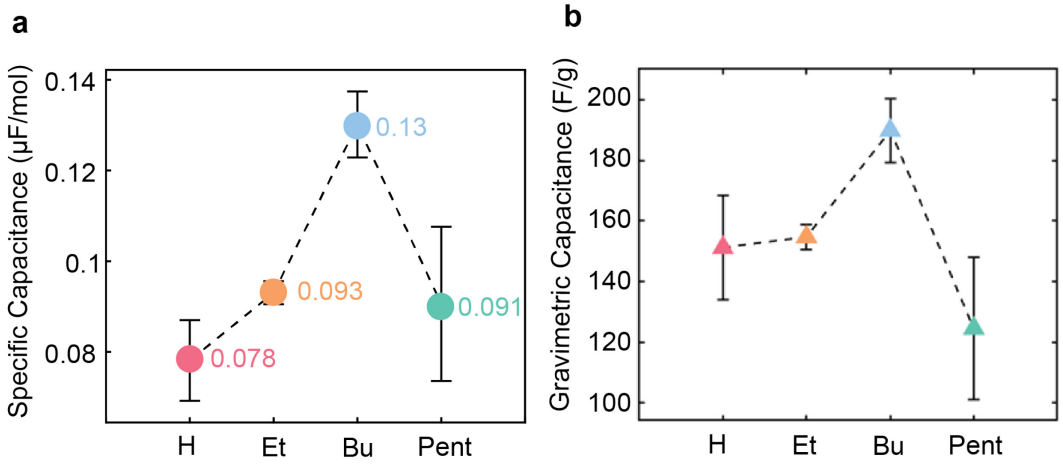

Figure 4-8. Comparison of a) molar specific capacitances and b) gravimetric specific capacitance at a scan rate of 5 mV/s.

The decrease in specific capacitance from Pent-MOF to Bu-MOF can experimentally be assigned to a continuously increasing ion transport resistance with increasing alkyl chain length; when R=*n*-Pent, ion transport cannot compensate for the rapidly charging capacitor of Pent-MOF. A first sign of this is the width of the CV trace for Pent-MOF, which shows the narrowest cycle, more typical for resistors (**Figure 4-7a**). Analysis of the scan rate dependence of the CV currents using the power law $i=av^b$ provides insight into diffusion resistances. The current i is hereby expressed as a constant factor, a, multiplied by the scan rate v to the power of a factor b, which can assume values between 0.5 and 1. In the lower limit of b=0.5, the current is proportional to the square root of the scan rate, which indicates an ideal semi-infinite diffusion regime, as described by the Randles-Ševčík equation.[17] For surface-adsorbed species, where no mass transfer limitations are at play, b=1.[17] Here, the b-values fitted for scan rates from 3 to 20 mV/s show a decreasing trend from 0.69 for H-MOF to 0.51 for Pent-MOF, pointing to increasing mass transfer limitations as the alkyl group becomes longer (**Figure 4-9, Table 4-3**).

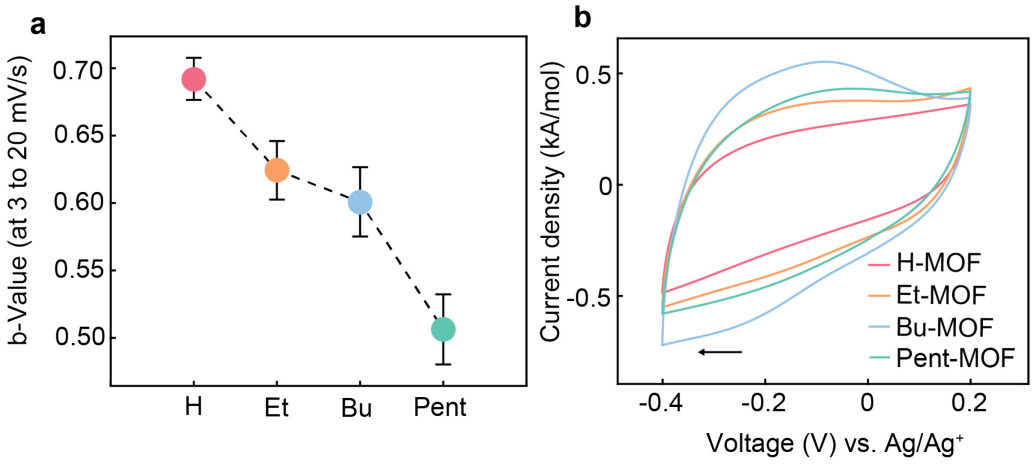

Figure 4-9. b) b-Values according to $i=av^b$, fitted to CV data collected at scan rates between 3 and 20 mV/s. b) CV traces of sweeps from 0.2 to −0.4 V at a scan rate of 5 mV/s.

Electrochemical impedance spectroscopy (EIS) performed at frequencies between 10 mHz and 500 kHz provided additional insight in the dynamic behavior of the electrode materials under various degrees of electrochemical polarization. Nyquist plots of the four materials reveal low equivalent series resistances of 1–2 Ω and overlapping semicircles at high frequencies, leading to a diffusion dominated regime, and capacitive tail that deviates from the vertical, typical for non-ideal porous supercapacitors (**Figure 4-10**). The diameters of the semicircles can be understood as the combination of interfacial and charge-transfer resistances. The onset of the quasi-linear tails moves to higher resistances with increasing chain length.[18] CV analysis

reveals increasingly faradaic behavior from H-MOF to Pent-MOF. By extending the voltage window of the cathodic sweep to −0.4 V, a broad faradaic feature emerges for the alkylated frameworks around −0.1 V, whereas H-MOF shows a smooth current response without signs of localized charge transfer induced current peaks (**Figure 4-9b**). Although scans from 0.2 to 0.0 V do not exhibit distinct faradaic peaks for any materials, the broad onset of the charge transfer peak at −0.1 V is likely to contribute to the capacitance in the smaller voltage window.

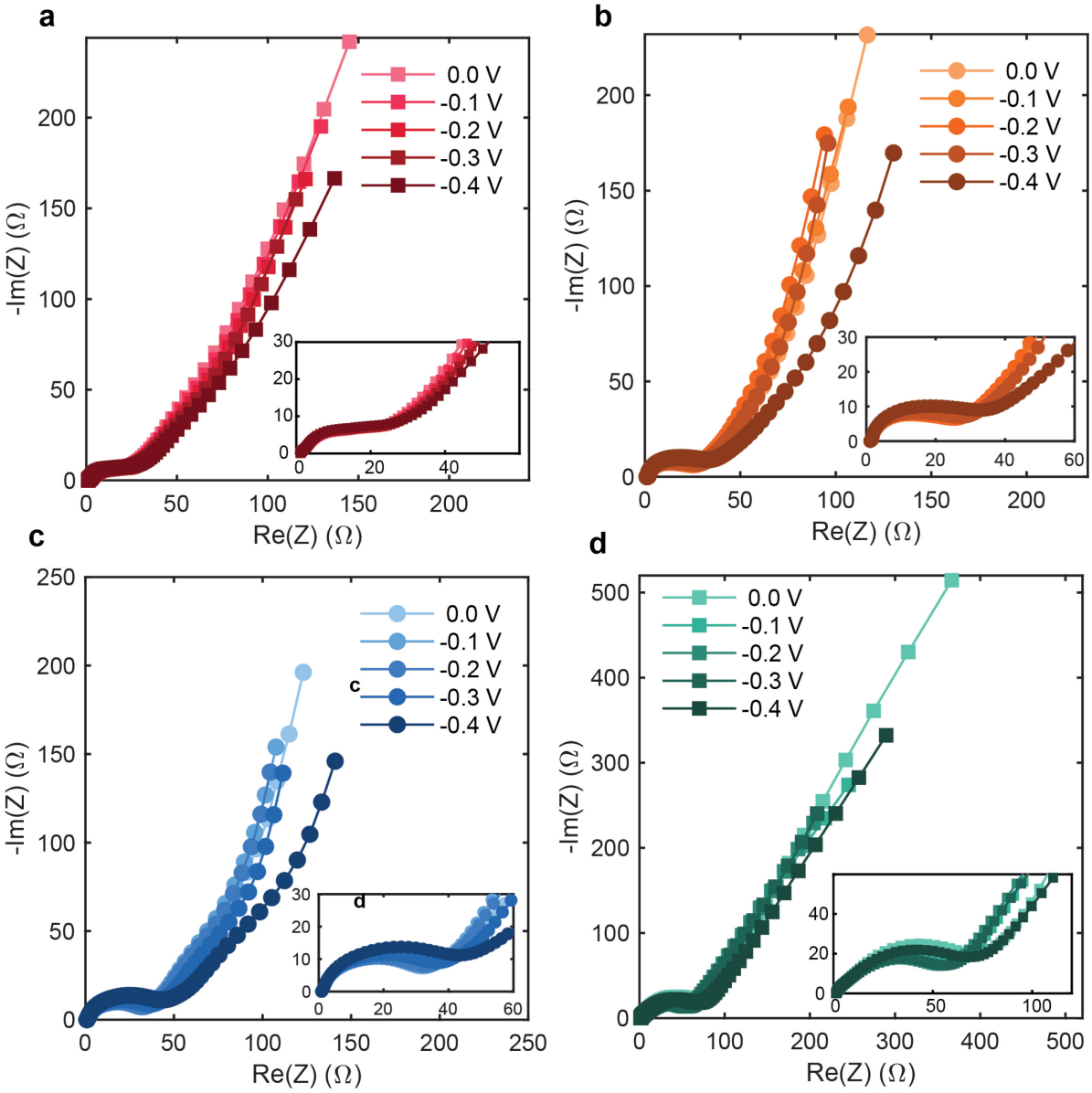

Figure 4-10. Nyquist plots for a) H-MOF, b) Et-MOF, c) Bu-MOF, and d) Pent-MOF for frequencies between 500 kHz and 10 mHz. Insets show high frequency semicircles.

Similar to DC techniques, AC analysis shows a clear trend of increasing resistance from H-MOF to Pent-MOF. This progression is, however, overshadowed by faradaic processes that become more prominent with interlayer spacing, dominating the charge transfer mechanism

for the most part. EIS at different electrochemical polarizations shows contributions of voltage dependent charge transfer resistances. Although the semicircle diameters in the Nyquist plot remain at almost the same real impedance for H-MOF, an increasingly stronger voltage dependence is observed for the alkylated MOFs (**Figure 4-10**). Bode-style projections (**Figure 4-11**) show that the voltage dependence of the real capacitance at low frequencies increases with increasing interlayer spacing, as seen in the more pronounced dome-shapes. This indicates an increasing contribution of charge transfer (i.e. faradaic) processes to the real capacitance.[19]

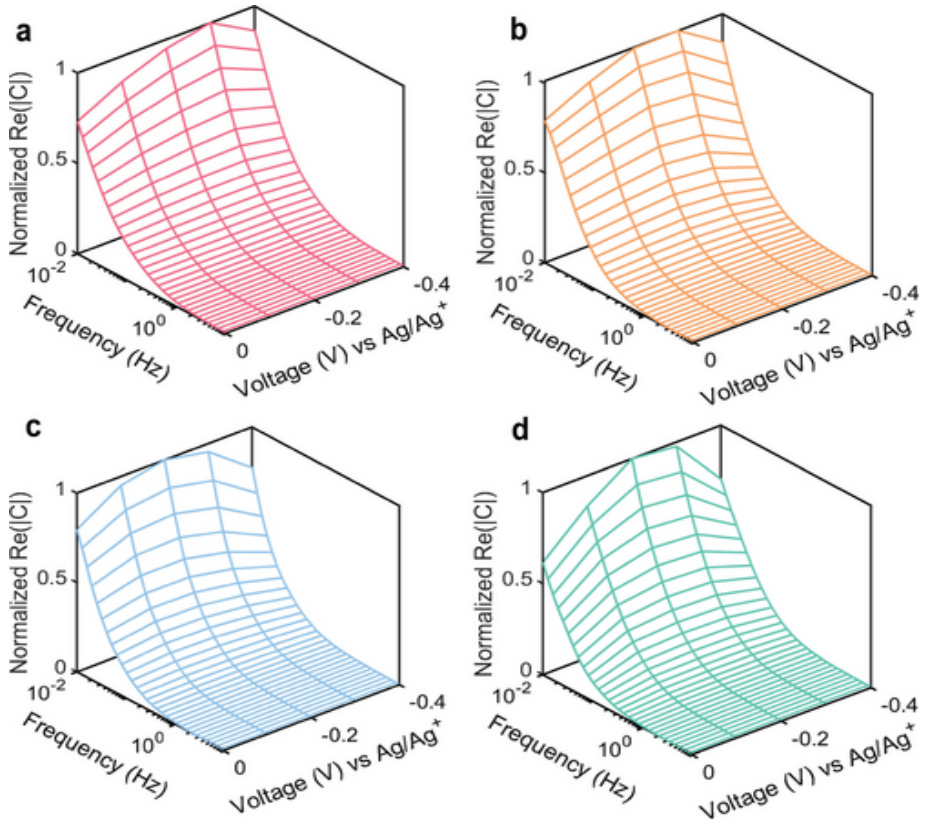

Figure 4-11. 3D-Bode representations of EIS of (a) H-MOF, (b) Et-MOF, (c) Bu-MOF and (d) Pent-MOF, showing the frequency and voltage dependence of the normalized real capacitance.

The increasing specific capacitances may be assigned to better access to the π-orbitals of the redox active ligands with increasing interlayer spacing. An alternative explanation for the increasing capacitance in this MOF series is, however, a potential confinement effect, whereby Li^+ ions become increasingly desolvated as they insert into the alkylated MOFs. Analysis of the relative faradaic contributions to the overall capacitance of exfoliated MOFs allows us to distinguish between these two possibilities: Cleavage of 2D layers would lead to increased accessibility of the π-planes and can be viewed as an "infinite" increase of interlayer spacing with concomitant maximization of the electrochemically active surface area. At the same time,

exfoliation would not change the pore diameter or chemical environment. Confinement is discouraged as ions would be able to access increased surface without shedding their solvation sphere.

Electrochemical Characterization of Exfoliated Materials

To test the effect of exfoliation, Bu-MOF and Pent-MOF were subjected to sonochemical treatment in ethanol. After 5 h of sonication, a subtle color change of the supernatant solution from grey-blue to a clear blue solution was observed. Centrifugation was performed to remove larger particles, and a blue colloidal solution of exfoliated MOF was obtained. Remarkably, this solution is stable under ambient conditions for at least several weeks without aggregation. The progress of exfoliation was followed via ultraviolet-visible (UV/Vis) spectroscopy. The UV/Vis spectra of the exfoliated Bu-MOF and Pent-MOF in ethanol matched their diffuse reflectance spectra as solids (**Figure 4-12**). Colloidal suspensions of insufficiently sonicated MOF show shifted absorbances, likely due to strong contributions of scattering on larger particles.

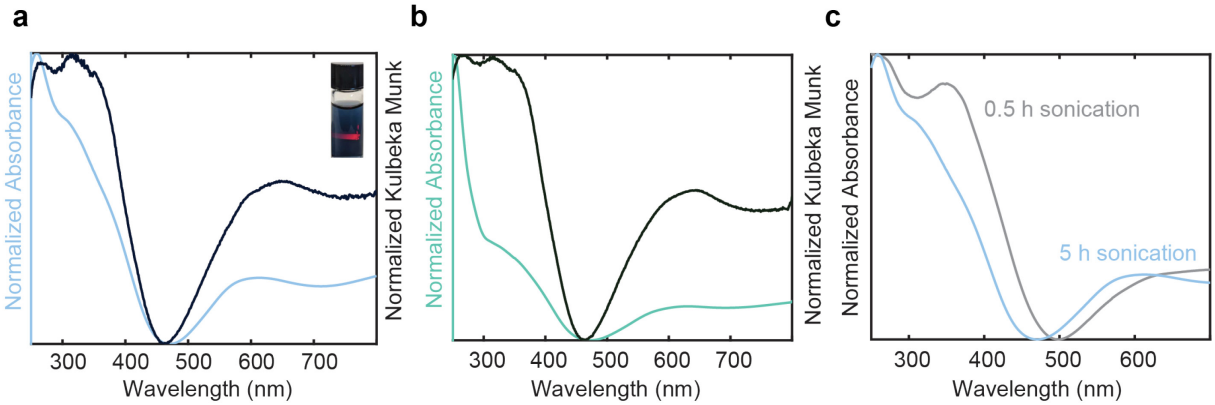

Figure 4-12. UV-Vis spectra of a) exfoliated Bu-MOF in ethanol solution (light) and diffuse reflectance (dark) of bulk Bu-MOF, b) exfoliated Pent-MOF in ethanol solution (light) and diffuse reflectance (dark) of bulk Pent-MOF, and c) UV-Vis spectra of Bu-MOF after 0.5 h and 5 h of sonication in ethanol. The inset in a) shows a solution of exfoliated Bu-MOF in ethanol.

Retention of crystal lattice of Bu-MOF was confirmed by transmission electron microscopy (TEM), clearly showing the lattice fringes of hexagonal particles (**Figure 4-13**). Raman spectroscopy shows bands typical for 2D materials and reveals a sharpening of bands upon exfoliation, consistent with a decrease in inhomogeneity of environments (**Figure 4-14**).[22]

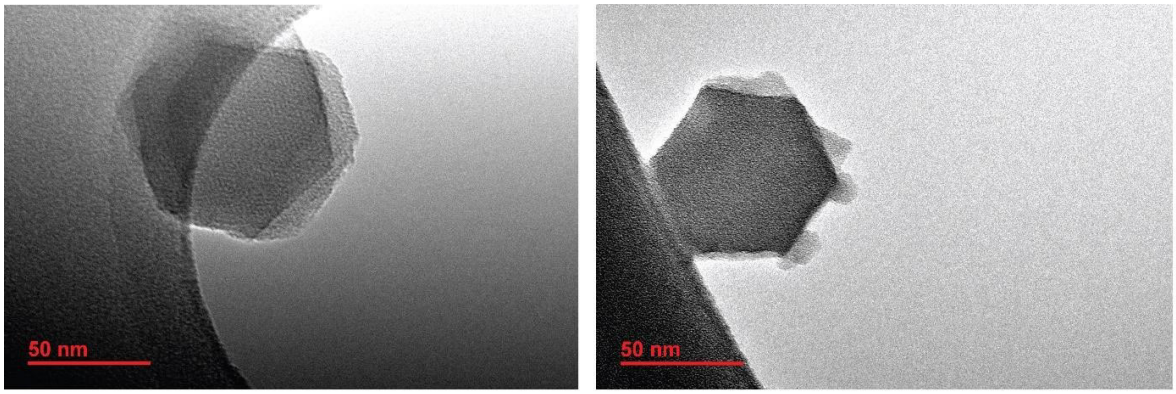

Figure 4-13. TEM images of exfoliated Bu-MOF.

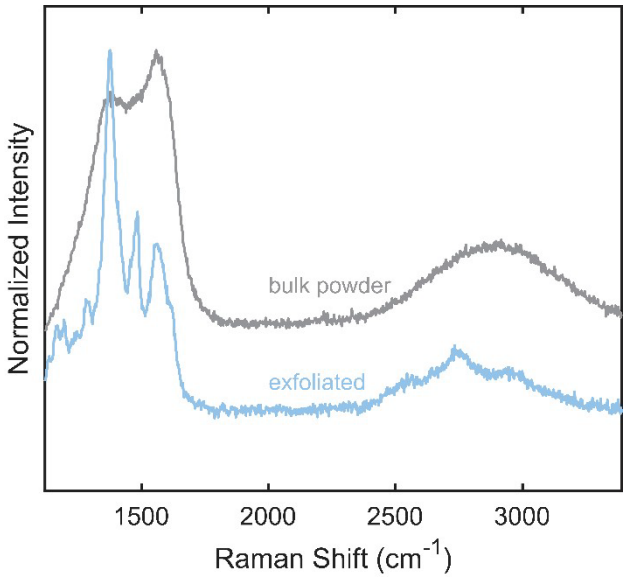

Figure 4-14. Raman spectra of bulk Bu-MOF and drop-casted exfoliated Bu-MOF on silicon substrate.

Bode projection of the impedance spectra of the exfoliated Bu-MOF with the same electrode composition as the bulk material shows higher voltage dependence of the real capacitance across a wider frequency range (**Figure 4-15**). This clearly demonstrates the increase in faradaic contributions upon exfoliation.[19, 23] The data for the exfoliated Pent-MOF mimics that of Bu-MOF (**Figure 4-15b**). As confinement decreases while faradaic contributions increase for the exfoliated MOFs, we may rule out confinement as the major contributor to the observed increase in capacitance and faradic processes across the series of MOFs. Instead, we assign the increasing faradaic nature of charge storage to better access to the π-orbitals of the redox active ligands, caused by increasing interlayer spacing. The interactions of ions with the MOF interlayer may be viewed as the equivalent to the intercalation pseudocapacitive mechanism in

non-porous structures in which lithium ions interact with active sites that reside between 2D layers.[5]

Through rational ligand modification of porous 2D conductive MOFs, we were able to promote faradaic processes and enhance the specific capacitance by a factor of 1.7 by increasing interlayer spacing. Electrochemical analysis allowed for deconvolution of opposite trends for resistive contributions and charge transfer-based contributions across the series of MOFs. Bulk exfoliation yielded stable colloidal solutions and further promoted faradaic processes by providing better access to redox active ligand planes. Increasing access to ligand-based active sites via interlayer distance is thus a viable strategy to introduce faradaic pseudocapacitive processes for porous 2D MOFs and bridges our understanding of porous double layer capacitors and layered intercalation-based pseudocapacitors. Our findings inspire the possibility of reaching higher energy densities compared to non-porous layered intercalation pseudocapacitors by utilizing active sites across the entire bulk. These findings might guide future material design and engineering towards electrode materials with enhanced energy and power density.

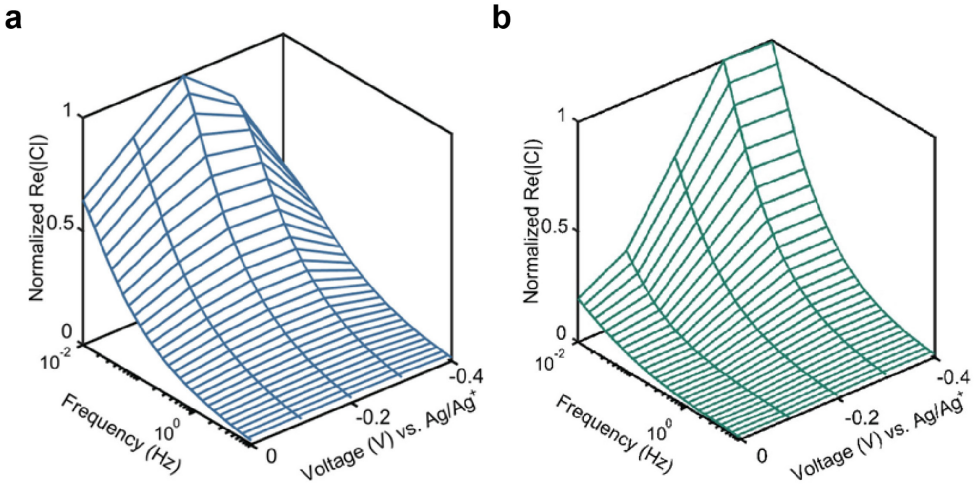

Figure 4-15. 3D-Bode representations of EIS of a) exfoliated Bu-MO and b) exfoliated Pent-MOF, showing the frequency and voltage dependence of the normalized real capacitance.

4.4 Materials and Supplementary Information

4.4.1 Materials

$Ni(OAc)_2 \cdot 6H_2O$, indole, alkyl bromides and LiTFSI were purchased from Sigma-Aldrich and were used without further purification. Dry THF and toluene were purchased from VWR and collected from an alumina column solvent purification system. ACN and EtOH were used as received. Activated carbon was prepared as a thin film by repeated kneading and rolling of a slurry of activated carbon, acetylene black and a PTFE solution mixture in 8:1:1 ratio, respectively, with ethanol. The prepared films were dried at 120 °C overnight prior to use in electrochemical capacitors. Standard Schlenk techniques were used for ligand synthesis.

4.4.2 Characterization Methods

Electrical conductivity

The electrical conductivity was measured using a linear four-point probe setup on pressed pellets at room temperature under ambient atmosphere. A Keithley 2450 source-meter was used as a current source and a Keithley 2182A unit was used as a voltmeter. The measured conductivity of the four MOFs was found to degrade up to one order of magnitude over several months. This is possibly caused by exposure to atmospheric humidity during the measurements or storage, resulting in lower values compared to previous reports.[16]

Infrared spectroscopy (IR)

IR measurements were performed on a Bruker Tensor 37 (MIR source and KBr beam splitter) with a mercury cadmium telluride (MCT, cooled with liquid nitrogen) detector and a germanium attenuated total reflectance (ATR) sample holder.

Powder X-ray diffraction (PXRD)

PXRD patterns were recorded with a Bruker D8 Advance diffractometer equipped with a Göbel mirror, rotating sample stage, LynxEye detector and Cu Kα (λ = 1.5406 Å) X-ray source in a $\theta = 2\theta$ Bragg–Brentano geometry. An anti-scattering slit (1 mm) and an exchangeable detector slit (8 mm) were used. The tube voltage and current were 40 kV and 40 mA, respectively. Knife-edge attachments were used to remove scattering at low angles.

Samples for PXRD were prepared by placing electrodes or powders on a zero-background silicon (510) crystal plate. PXRD patterns were normalized against the modelled position of the 100 reflections.[16]

Scanning electron microscopy (SEM)

SEM images were recorded using a Zeiss MERLIN SEM at 3.00 kV using an InLens detector at the MIT Materials Research Laboratory.

N_2 sorption isotherms

N_2 isotherms were measured by a volumetric method using a Micromeritics ASAP 2020 Plus gas sorption analyzer using liquid nitrogen baths (77 K). Samples were heated to 90 °C under a vacuum of 0.3 mtorr for 16 h prior to the analysis. Ultrahigh purity grade (99.999% purity) N_2, oil-free valves and gas regulators were used for all the free space correction and measurements.

Transmission electron microscopy (TEM)

TEM images were obtained using the FEI Tecnai (G2 Spirit TWIN) transmission electron microscope at the MIT Materials Research Laboratory. Sonicated samples in ethanol were drop-casted onto lacey carbon copper grids.

UV-vis-NIR diffuse reflectance spectra (DRUV–vis–NIR)

DRUV-Vis-NIR spectra were obtained using a Cary 5000i spectrophotometer, fitted with the UV-Vis DiffusIR accessory (Pike Technologies), at a scan speed of 200 nm/min under ambient conditions. Prior to sample measurements, a baseline using KBr was collected. Samples were diluted to 1 wt% in KBr. After data collection, the Kubelka-Munk function was applied to the raw data to eliminate scattering.

Solution phase UV-Vis-NIR spectroscopy

UV-Vis-NIR spectra were obtained using a Cary 5000i spectrophotometer with background subtraction. Ethanol solutions were measured in quartz cells purchased from spectrocell.

Raman spectroscopy

Raman spectra were measured using a Renishaw Invia Reflex Raman Confocal Microscope at the MIT Materials Research Laboratory under the excitation laser of 532 nm with the laser

not exceeding 1% of the full power. Unexfoliated MOF was measured as pressed powder while exfoliated MOF was drop-casted onto silicon substrate.

Electrochemical Characterization

Home-made T-shaped Swagelok cells fitted with stainless steel collectors were used for tests in three-electrode configurations. Bulk material was pressed directly onto Ni-foam using 3.0 ton force/cm^2 with a mass loading of 0.5 - 1.5 mgMOF/cm^2 as the working electrode. Overcapacitive activated carbon films were used as counter electrodes while a silver wire served as a pseudo-reference. Glass fiber separators were used as well as 1 M LiTFSI in ACN as the electrolyte.

All electrochemical measurements were carried out using a Biologic VSP-300 potentiostat. Impedance measurements were performed using a multi-sinusoidal signal with an amplitude of 10 mV over a large frequency range of 10 mHz – 500 kHz. The MOFs were stable under the employed cycling conditions, although Et-MOF showed a higher propensity for decomposition upon prolonged cycling and storage. Freshly synthesized Et-MOF was thus used for electrochemical characterization whereas the other materials were stored in a desiccator. The molar specific capacitance is given for mols of TAT ligand and was calculated from the CV curves using equation:

$$c = \frac{\int IdVM}{mv\Delta V} \quad (1)$$

where m = mass of the active material, ΔV = potential window, v = scan rate and M = molar mass of the formula unit containing one TAT molecule ($Ni_{1.5}(HIR_3\text{-}TAT)$). Values are given as the average of three measurements using different cells each time. b-Values were fitted from CV data according to $i = av^b$. Molar current densities and capacitances can be converted to gravimetric versions *via* $i_g = i_{molar}/M$ *and* $c_g = c_{molar}/M$, where M is the molecular weight of a $Ni_{1.5}$TAT unit. The molecular weights used for this conversion were 517.04 g/mol, 601.70 g/mol, 685.86 g/mol and 727.94 g/mol for H-MOF, Et-MOF, Bu-MOF, and Pent-MOF, respectively.

4.4.3 Molecular Synthesis

Synthesis of HIR3-TAT Ligands

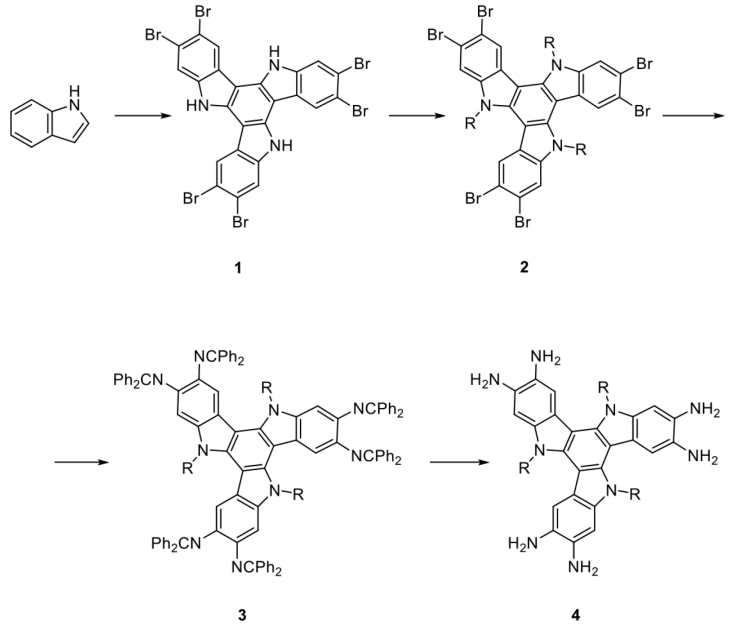

Figure 4-16. Synthetic scheme for the synthesis of HIR_3-TAT from indole.

The synthesis of hexabromotriazatruxene **1** and hexaiminotriazatruxene **4-H** and was carried out using previously described procedures.[15,24]

Alkylated hexabromotriazatruxenes 2

Alkylation of hexabromotriazatruxene was performed according to modified literature procedures.[2] A mixture of hexabromotriazatruxene **1** and KOH (10 equiv.) were heated to reflux in dry THF (100 mL) for 30 min under nitrogen atmosphere. The alkyl bromide (4.6 equiv. of 1-bromoethane, 1-bromobutane or 1-bromopentane) was added and the mixture and refluxed for 14 h before cooling to room temperature. The light red mixture was diluted with DCM and washed with 10% HCl. The organic phase was dried over Na_2SO_4, and solvents removed under vacuum to afford a brown solid as the crude product. The solids were washed with hexane then MeOH to afford off-white solids. Recrystallization in ethyl acetate/chloroform yields the alkylated hexabromotrizatruxene **2** as white needles. ^{1}H NMR (C_6D_6, 400 MHz): **2-Et**: δ (ppm) = 1.02 (t, 3H), 4.06 (q, 2H), 7.62 (s, 1H, H_{ar}), 8.43 (s, 1H, H_{ar}). **2-Bu**: δ (ppm) = 0.96 (t, 3H), 1.40 (m, 2H), 1.97 (m, 2H), 4.63 (t, 2H), 7.81 (s, 1H, H_{ar}), 8.37 (s, 1H, H_{ar}). **1-Pent**: δ (ppm) = 0.89 (t, 3H), 1.40 (m, 4H), 2.01 (m, 2H), 4.67 (t, 2H), 7.82 (s, 1H, H_{ar}), 8.36 (s, 1H, H_{ar}).

Hexaamino-N-alkyl-triazatruxenes (3,4)

To a flame dried Schlenk flask were added $Pd_2(dba)_3$ (0.21 mmol, 0.22 equiv.), *rac*-BINAP (0.43 mmol, 0.44 equiv.) and 50 ml dry toluene. The mixture was degassed by three freeze–pump–thaw cycles and refluxed for 30 min. The solution was then cooled to room temperature and alkylated hexabromotriazatruxene (0.97 mmol, 1.0 equiv.), sodium *tert*-butoxide (8.5 mmol, 8.8 equiv.) and benzophenone imine (8.5 mmol, 8.8 equiv.) were added and degassed three more times. The mixture was refluxed for 48 h to afford a dark red-orange solution which was dried under vacuum. The crude product was extracted using DCM and further purified via silica column chromatography (Hex/EA = 5/1). The bright red product **3** was directly used for the next step by dissolving in nitrogen purged THF. 10 ml of nitrogen-purged concentrated HCl were added to the solution and stirred at room temperature for 1 h until a beige precipitate formed. The solids were isolated via centrifugation, washed with water and hexane. The product **4** was dried under high vacuum and stored under nitrogen atmosphere. ^{1}H NMR (DMSO-d_6, 400 MHz): **4-Et**: δ (ppm) = 1.40 (t, 3H), 4.79 (q, 2H), 7.28 (s, 1H, H_{ar}), 8.14 (s, 1H, H_{ar}). **4-Bu**: δ (ppm) = 0.59 (t, 3H), 0.86 (m, 2H), 1.63 (m, 2H), 4.79 (t, 2H), 7.30 (s, 1H, H_{ar}), 8.18 (s, 1H, H_{ar}). **4-Pent**: δ (ppm) = 0.52 (t, 3H), 0.80 (m, 2H), 0.97 (m, 2H), 1.61 (m, 2H), 4.78 (t, 2H), 7.27 (s, 1H, H_{ar}), 8.15 (s, 1H, H_{ar}).

4.4.4 MOF Synthesis

Ni_3(HI-TAT)$_2$, Ni_3(HIEt$_3$-TAT)$_2$, Ni_3(HIBu$_3$-TAT)$_2$ (H-MOF, Et-MOF, Bu-MOF)

H-MOF was synthesized according to a published procedure.[15] **Et-MOF** and **Bu-MOF** were synthesized under identical conditions: 5.05 mg $Ni(OAc)_2{\cdot}6H_2O$ in 3 mL DMF and 3 mL DMA were preheated to 65 °C in a 20 mL vial. 2 mL of aqueous 2 M NaOAc solution and 10 mg of the hexaamino-TAT ligand in 1.5 mL water were added and heated over night with stirring to yield a black powder that was washed with water and MeOH. Elemental analysis: $Ni_3(HIEt_3TAT)_2{\cdot}4.1H_2O{\cdot}7.9$MeOH: Calculated: C: 53.34%; H: 6.18%; N: 16.47%. Found: C: 53.35%; H: 5.00%; N: 15.97%. $Ni_3(HIBu_3\text{-}TAT)_2{\cdot}3.2H_2O{\cdot}4.4$MeOH: Calculated: C: 58.38%; H: 6.66%; N: 16.03%. Found: C: 58.41%; H: 5.89%; N: 15.71%.

Ni_3(HIPent$_3$-TAT)$_2$ (Pent-MOF)

5.05 mg $Ni(OAc)_2 \cdot 6H_2O$ in 3 mL DMF and 3 mL DMA were preheated to 65 °C in a 20 mL vial.10 mg of the hexaamino-TAT ligand in 3.5 mL of aqueous 2 M NaOAc solution were added and heated over night with stirring to yield a black powder that was washed with water and MeOH. Elemental analysis: Ni_3(HIPent$_3$-TAT)$_2 \cdot 3.4H_2O \cdot 5.2$MeOH: Calculated: C: 59.25%; H: 7.16%; N: 14.94%. Found: C: 59.28%; H: 6.39%; N: 14.62%.

4.4.5 Supplementary Characterization

SEM of Cycled Electrodes

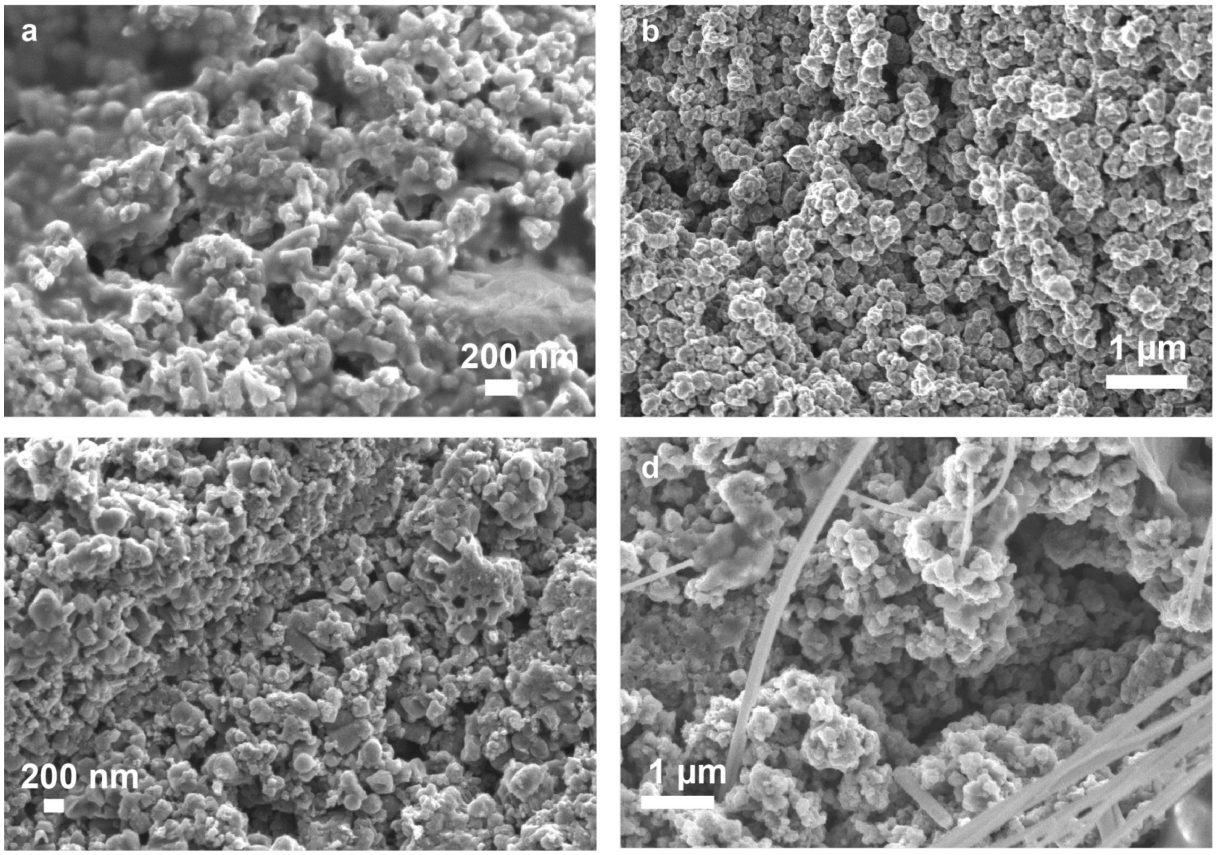

Figure 4-17. SEM Images of cycled electrodes of a) H-MOF, b) Et-MOF, c) Bu-MOF, and d) Pent-MOF. Electrodes were rinsed with water and ACN after disassembly of cells and dried under vacuum.

N_2 Sorption Isotherms and Total Pore Volume

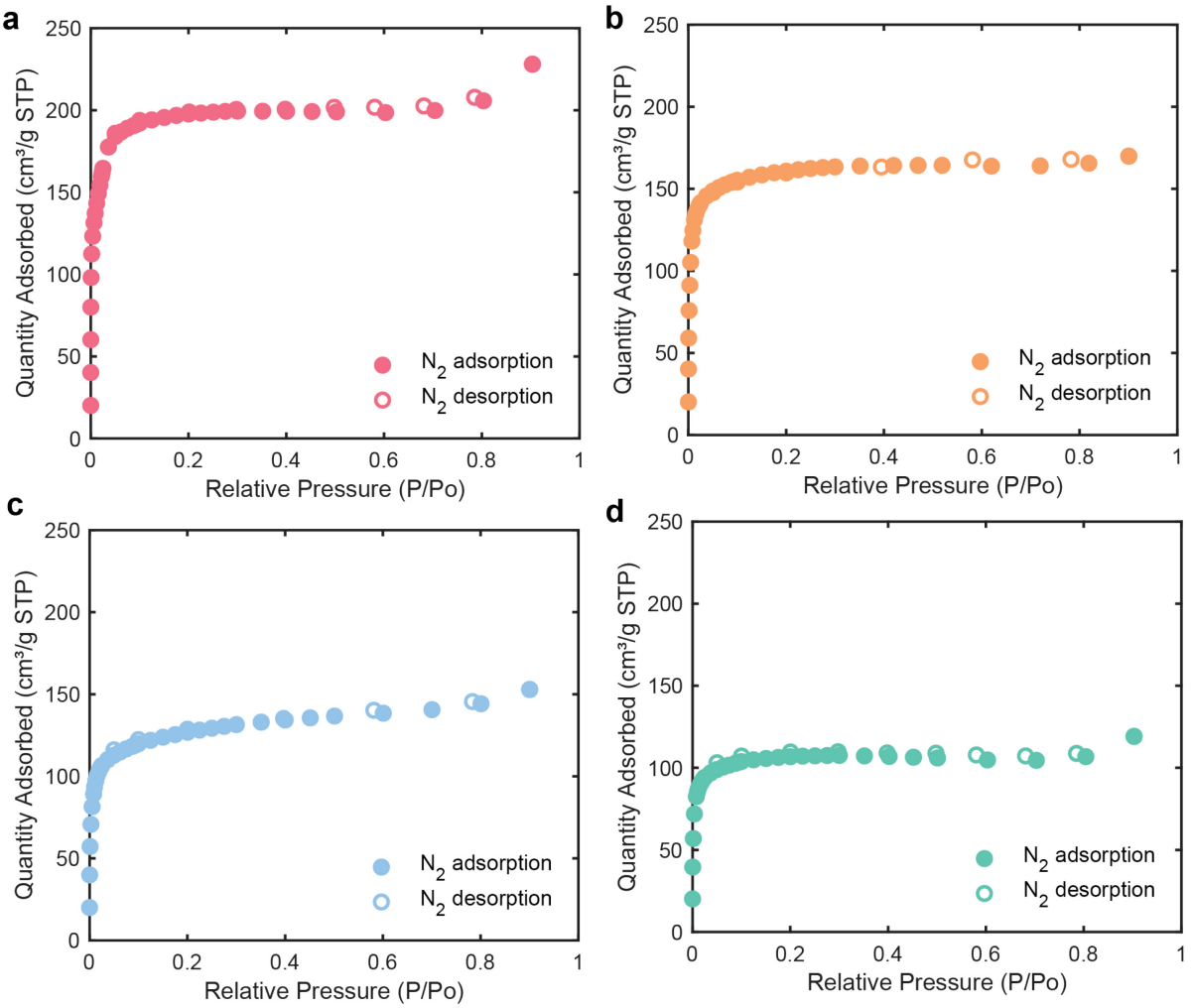

Figure 4-18. N_2 adsorption and desorption isotherms at 77 K for a) H-MOF, b) Et-MOF, c) Bu-MOF, and d) Pent-MOF.

Table 4-2. Single point N_2 desorption total pore volumes.

	Single point pore volume (cm^3/g)
H-MOF	0.353
Et-MOF	0.263
Bu-MOF	0.236
Pent-MOF	0.184

Cyclic Voltammetry

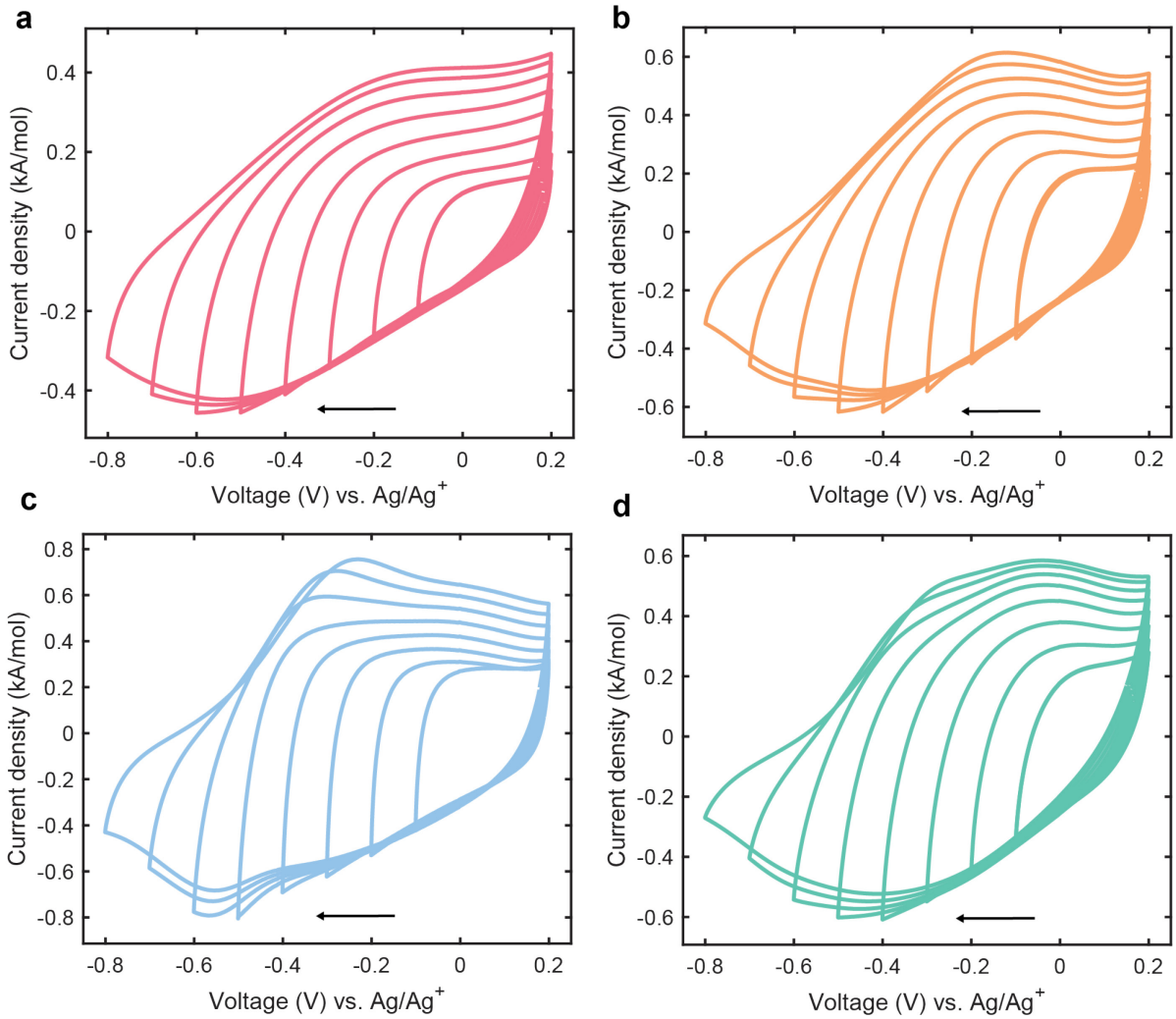

Figure 4-19. CV traces of a) H-MOF, b) Et-MOF, c) Bu-MOF, and d) Pent-MOF in three-electrode cells. The second of five cycles in each voltage window is depicted.

b-Value Analysis

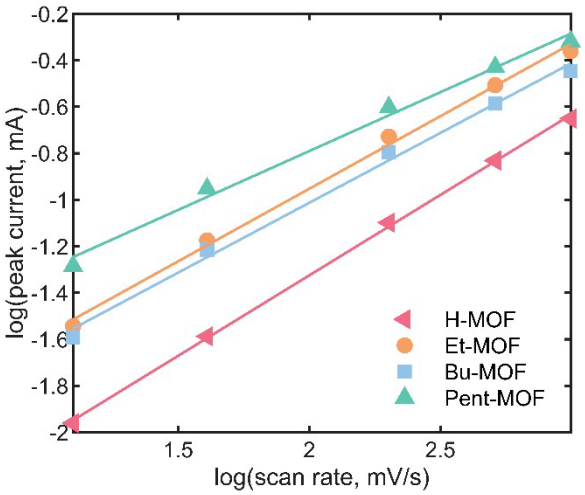

Figure 4-20. Relationship of log(scan rate) vs log(peak current) between 3 and 20 mV/s and their linear fit.

Table 4-3. Slope and intercepts of linear fit of log(scan rate) vs log(peak current) between 3 and 20 mV/s.

	Slope (As/V)	**Intercept (mA)**
H-MOF	0.692	2.07
Et-MOF	0.624	2.11
Bu-MOF	0.601	1.93
Pent-MOF	0.506	1.70

4.5 References

(1) Simon, P.; Gogotsi, Y. Materials for Electrochemical Capacitors. *Nat. Mater.* **2008**, *7*, 845–853.

(2) Kötz, R.; Carlen, M. Principles and Applications of Electrochemical Capacitors. *Electrochim. Acta* **2000**, *45* (15–16), 2483–2498.

(3) Choi, C.; Ashby, D. S.; Butts, D. M.; DeBlock, R. H.; Wei, Q.; Lau, J.; Dunn, B. Achieving High Energy Density and High Power Density with Pseudocapacitive Materials. *Nat. Rev. Mater.* **2020**, *5* (1), 5–19.

(4) Banda, H.; Dou, J. H.; Chen, T.; Zhang, Y.; Dincă, M. Dual-Ion Intercalation and High Volumetric Capacitance in a Two-Dimensional Non-Porous Coordination Polymer. *Angew. Chem. Intl. Ed.* **2021**, *60* (52), 27119–27125.

(5) Banda, H.; Dou, J. H.; Chen, T.; Libretto, N. J.; Chaudhary, M.; Bernard, G. M.; Miller, J. T.; Michaelis, V. K.; Dincă, M. High-Capacitance Pseudocapacitors from Li^+ Ion Intercalation in Nonporous, Electrically Conductive 2D Coordination Polymers. *J. Am. Chem. Soc.* **2021**, *143* (5), 2285–2292.

(6) Sheberla, D.; Bachman, J. C.; Elias, J. S.; Sun, C. J.; Shao-Horn, Y.; Dincă, M. Conductive MOF Electrodes for Stable Supercapacitors with High Areal Capacitance. *Nat. Mater.* **2017**, *16* (2), 220–224.

(7) Zhang, P.; Wang, M.; Liu, Y.; Fu, Y.; Gao, M.; Wang, G.; Wang, F.; Wang, Z.; Chen, G.; Yang, S.; Liu, Y.; Dong, R.; Yu, M.; Lu, X.; Feng, X. Largely Pseudocapacitive Two-Dimensional Conjugated Metal-Organic Framework Anodes with Lowest Unoccupied Molecular Orbital Localized in Nickel-Bis(Dithiolene) Linkages. *J. Am. Chem. Soc.* **2022**, *145* (11), 6247–6256.

(8) Yu, M.; Dong, R.; Feng, X. Two-Dimensional Carbon-Rich Conjugated Frameworks for Electrochemical Energy Applications. *J. Am. Chem. Soc.* **2020**, *142* (30), 12903–12915.

(9) Nathan Hong, C.; Crom, A.; Feldblyum, J. I.; RLukatskaya, M. Metal-Organic Frameworks for Fast Electrochemical Energy Storage: Mechanisms and Opportunities. *Chem* **2023**.

(10) Zhang, Y.; Riduan, S. N.; Wang, J. Redox Active Metal– and Covalent Organic Frameworks for Energy Storage: Balancing Porosity and Electrical Conductivity. *Chem. Eur. J.* **2021**, *23* (65), 16419-16431.

(11) Fleischmann, S.; Zhang, Y.; Wang, X.; Cummings, P. T.; Wu, J.; Simon, P.; Gogotsi, Y.; Presser, V.; Augustyn, V. Continuous Transition from Double-Layer to Faradaic Charge Storage in Confined Electrolytes. *Nat. Energy* **2022**, *7* (3), 222-228.

(12) Shin, S.-J.; Gittins, J. W.; Golomb, M. J.; Forse, A. C.; Walsh, A. Microscopic Origin of Electrochemical Capacitance in Metal–Organic Frameworks. *J. Am. Chem. Soc.* **2023**, *145*(26), 14529-14538.

(13) Bi, S.; Banda, H.; Chen, M.; Niu, L.; Chen, M.; Wu, T.; Wang, J.; Wang, R.; Feng, J.; Chen, T.; Dincă, M.; Kornyshev, A. A.; Feng, G. Molecular Understanding of Charge Storage and Charging Dynamics in Supercapacitors with MOF Electrodes and Ionic Liquid Electrolytes. *Nat. Mater.* **2020**, *19* (5), 552–558.

(14) Lu, Y.; Hu, Z.; Petkov, P.; Fu, S.; Qi, H.; Huang, C.; Liu, Y.; Huang, X.; Wang, M.; Zhang, P.; Kaiser, U.; Bonn, M.; Wang, H. I.; Samorì, P.; Coronado, E.; Dong, R.; Feng, X. Tunable Charge Transport and Spin Dynamics in Two-Dimensional Conjugated Metal-Organic Frameworks. *J. Am. Chem. Soc.* **2024**, *146*(4), 2574-2582.

(15) Apostol, P.; Gali, S. M.; Su, A.; Tie, D.; Zhang, Y.; Pal, S.; Lin, X.; Bakuru, V. R.; Rambabu, D.; Beljonne, D.; Dincă, M.; Vlad, A. Controlling Charge Transport in 2D Conductive MOFs–The Role of Nitrogen-Rich Ligands and Chemical Functionality. *J. Am. Chem. Soc.* **2023**, *145*, 24669–24677.

(16) Lu, Y.; Zhang, Y.; Yang, C.-Y.; Revuelta, S.; Qi, H.; Huang, C.; Jin, W.; Li, Z.; Vega-Mayoral, V.; Liu, Y.; Huang, X.; Pohl, D.; Položij, M.; Zhou, S.; Cánovas, E.; Heine, T.; Fabiano, S.; Feng, X.; Dong, R. Precise Tuning of Interlayer Electronic Coupling in Layered Conductive Metal-Organic Frameworks. *Nat. Comm.* **2022**, *13* (1), 7240.

(17) Bard, A. J.; Faulkner, L. R. *Electrochemical Methods: Fundamental and Applications*, 2nd ed.; John Wiley & Sons: Hoboken, NJ, 2001.

(18) Mathis, T. S.; Kurra, N.; Wang, X.; Pinto, D.; Simon, P.; Gogotsi, Y. Energy Storage Data Reporting in Perspective–Guidelines for Interpreting the Performance of Electrochemical Energy Storage Systems. *Adv. Energy Mater.* **2019***, 9 (39),* 1902007.

(19) Ko, J. S.; Lai, C. H.; Long, J. W.; Rolison, D. R.; Dunn, B.; Nelson Weker, J. Differentiating Double-Layer, Psuedocapacitance, and Battery-like Mechanisms by Analyzing Impedance Measurements in Three Dimensions. *ACS Appl. Mater. Interfaces* **2020**, *12* (12), 14071–14078.

(20) Ferrari, A. C.; Meyer, J. C.; Scardaci, V.; Casiraghi, C.; Lazzeri, M.; Mauri, F.; Piscanec, S.; Jiang, D.; Novoselov, K. S.; Roth, S.; Geim, A. K. Raman Spectrum of Graphene and Graphene Layers. *Phys. Rev. Lett.* **2006**, *97* (18), 187401.

(21) Wang, S.; Wang, Q.; Shao, P.; Han, Y.; Gao, X.; Ma, L.; Yuan, S.; Ma, X.; Zhou, J.; Feng, X.; Wang, B. Exfoliation of Covalent Organic Frameworks into Few-Layer Redox-Active Nanosheets as Cathode Materials for Lithium-Ion Batteries. *J. Am. Chem. Soc* **2017**, *139* (12), 4258–4261.

Chapter Specific Acknowledgement

This chapter is adapted with permission from Su, A. Y.; Apostol, P; Wang, J; Vlad, A; Dincă, M. Electrochemical Capacitance Traces with Interlayer Spacing in Two-dimensional Conductive Metal–Organic Frameworks. Angew. Chem. Int. Ed. 2024, 63, e202402526. Copyright © 2024 The Authors. The experimental work was financially supported by the Department of Energy (DE-SC0023288). The synthesis of $Ni_3(HITAT)_2$ was conducted by Dr. Petru Apostol who was financially supported under the European Union's Horizon 2020 research and innovation program (grant agreement no. 770870,MOOiRE). Dr. Jiande Wang has provided highly valued discussion and suggestions that have significantly helped to shape this work. Part of this work (SEM, TEM, Raman) made use of the MRL (now MIT.Nano) shared characterization facilities at MIT.